



# VCU

Virginia Commonwealth University  
VCU Scholars Compass

---

Theses and Dissertations

Graduate School


---

2021

## Live Cell Biomass Tracking for Basic, Translational, and Clinical Research

Graeme Murray

Follow this and additional works at: <https://scholarscompass.vcu.edu/etd>

 Part of the [Diagnosis Commons](#), [Nanomedicine Commons](#), [Optics Commons](#), and the [Other Analytical, Diagnostic and Therapeutic Techniques and Equipment Commons](#)

© Graeme Murray

---

Downloaded from

<https://scholarscompass.vcu.edu/etd/7129>

This Dissertation is brought to you for free and open access by the Graduate School at VCU Scholars Compass. It has been accepted for inclusion in Theses and Dissertations by an authorized administrator of VCU Scholars Compass. For more information, please contact [libcompass@vcu.edu](mailto:libcompass@vcu.edu).

© Graeme F. Murray 2021

---

All Rights Reserved

# Live Cell Biomass Tracking for Basic, Translational, and Clinical Research

A dissertation submitted in partial fulfillment of the requirements for the degree of Doctor of Philosophy at  
Virginia Commonwealth University

by

Graeme Fritchen Murray

B.A. University of Chicago, 2014

Director: Dr. Jason C. Reed

Associate Professor, Dept. of Physics

Virginia Commonwealth University

Richmond, VA

January 26<sup>th</sup>, 2020

### Acknowledgements:

I'd like to thank my Mom, Dad, brother Alex, and spouse Zoe for the support they have provided me and the sacrifices they have made so I could complete this work.

I'd like to thank Dr. Jason Reed for guiding my studies and listening when I came barging into his office and began speaking without any context multiple times per week. As well I'd like to thank members of his lab: Kevin Leslie, Daniel Guest, Sean Koebley, and Andrey Mikheykin without whom this work could not have been completed.

I'd like to thank all members of my committee, Dr. Loren Picco, Dr. Chuck Harrell, Dr. Amir Toor, and Dr. Ross Mikkelsen who provided insight and guidance throughout my work.

I'd like to thank Dr. Michael Donnenberg and Dr. Massimo Bertino for creating an MD/PhD Nanoscience program, and members of the MD/PhD program especially Sandra Sorrell and Georgia Straton.

I'd like to thank all the members of the Harrell, Gewirtz, and Teitell labs with whom I have collaborated with to create this work, in particular but not limited to: Tia Turner, Mohammed Alzubi, David Boyd, Valerie Carpenter, Tareq, Saleh, Liliya Tyutyunyk-Massey, Dian Huang, and Bowen Wang.

Finally, I'd like to thank my friends Ben Xia-Reinert, Rohan Puri, Mike Rogers, John Zacccone, and Will Massey.

## Publications resulting from this work:

**Murray, G. F.**; Guest, D.; Mikheykin, A.; Toor, A.; Reed, J., Single cell biomass tracking allows identification and isolation of rare targeted therapy-resistant DLBCL cells within a mixed population. *Analyst* **2021**.

Saleh, T.; Carpenter, V. J.; Tyutyunyk-Massey, L.; **Murray, G.**; Levenson, J. D.; Souers, A. J.; Alotaibi, M. R.; Faber, A. C.; Reed, J.; Harada, H.; Gewirtz, D. A., Clearance of therapy-induced senescent tumor cells by the senolytic ABT-263 via interference with BCL-XL -BAX interaction. *Mol Oncol* **2020**.

Huang, D.; Roy, I. J.; **Murray, G. F.**; Reed, J.; Zangle, T. A.; Teitell, M. A., Identifying fates of cancer cells exposed to mitotic inhibitors by quantitative phase imaging. *Analyst* **2019**

**Murray, G. F.**; Turner, T. H.; Guest, D.; Leslie, K. A.; Alzubi, M. A.; Radhakrishnan, S. K.; Harrell, J. C.; Reed, J., QPI Allows in vitro Drug Screening of Triple Negative Breast Cancer PDX Tumors and Fine Needle Biopsies. *Frontiers in Physics* **2019**

Saleh, T.\*; Tyutyunyk-Massey, L.\*; **Murray, G. F.\***; Alotaibi, M. R.; Kawale, A. S.; Elsayed, Z.; Henderson, S. C.; Yakovlev, V.; Elmore, L. W.; Toor, A.; Harada, H.; Reed, J.; Landry, J. W.; Gewirtz, D. A., Tumor cell escape from therapy-induced senescence. *Biochem Pharmacol* **2018**.

**Murray, G. F.**; Turner, T. H.; Leslie, K. A.; Alzubi, M. A.; Guest, D.; Sohal, S. S.; Teitell, M. A.; Harrell, J. C.; Reed, J., Live Cell Mass Accumulation Measurement Non-Invasively Predicts Carboplatin Sensitivity in Triple-Negative Breast Cancer Patient-Derived Xenografts. *ACS Omega* **2018**

\*authors contributed equally to this work

# Table of Contents

<b>1</b>	<b>Chapter 1: Biomass</b>	<b>1</b>
1.1	Importance of the regulation of cell mass	1
1.2	Measuring cell mass	1
<b>2</b>	<b>Chapter 2: Previous work on High Speed Live Cell Interferometry (HSLCI)</b>	<b>5</b>
2.1	Overview of original HSLCI system	5
2.2	HSLCI study in melanoma	8
<b>3</b>	<b>Chapter 3: HSLCI predicting <i>in vivo</i> carboplatin sensitivity</b>	<b>11</b>
3.1	Ex vivo methods for predicting patient drug sensitivity	11
3.2	Effects of carboplatin on PDX models	12
3.3	Identification of carboplatin resistant single cells in carboplatin sensitive UCD52	14
3.4	Development and screening of UCD52-CR	15
3.5	Assay details	16
3.6	Conclusions	17
3.7	Methods	17
<b>4</b>	<b>Chapter 4: Technological Improvements</b>	<b>18</b>
4.1	Image collection upgrades	18
4.2	Image processing upgrades	19
<b>5</b>	<b>Chapter 5: Application of upgrades: fine needle biopsy and drug testing on PDX models</b>	<b>20</b>
5.1	Screening from a fine needle biopsy	20
5.2	Screening more potentially HSLCI challenging drugs in a shorter time	22
5.3	Methods	27
<b>6</b>	<b>Chapter 6: Isolation of Cells</b>	<b>28</b>
6.1	Addition of micropipette system	28
6.2	Targeted therapy and the need to study drug tolerance	29
6.3	SU-DHL-10 & SU-DHL-6 differential sensitivity to idelalisib	30
6.4	SU-DHL-10/SU-DHL-6 1:100 idelalisib resistant cell isolation	31
6.5	Methods	33
<b>7</b>	<b>Chapter 7: Senescence</b>	<b>34</b>
7.1	Introduction	35
7.2	Changes in cell size	35
7.3	Changes in cell growth and escape from senescence	38
7.4	Treatment with ABT-263	43
7.5	Methods	44
<b>8</b>	<b>Conclusions and Future Directions</b>	<b>45</b>
8.1	HSLCI as a clinical screening tool	45

8.2	<i>HSLCI as a translational research tool</i> .....	46
8.3	<i>HSLCI as basic research tool</i> .....	47
8.4	<i>Conclusion</i> .....	47
<b>9</b>	<b>Appendix</b> .....	<b>53</b>
9.1	<i>Supplementary Figures</i> .....	54

## List of Figures

Figure 1: Michelson Interferometry .....	3
Figure 2: Quadriwave Lateral Shearing Interferometry (QWLSI).....	4
Figure 3: Overview of original HSLCI setup.....	5
Figure 4: Ray diagram of focusing module .....	6
Figure 5: Image Collection .....	7
Figure 6: Identifying drug resistant and sensitive cells in a mixed population.....	9
Figure 7: MEK inhibitor screen on vemurafenib resistant melanoma .....	10
Figure 8: Effects of carboplatin on three PDX models as measured in vitro by HSLCI.....	12
Figure 9: Effects of carboplatin on three PDX models as measured in vivo.....	13
Figure 10: Examples of resistant and sensitive UCD52 cells to 100 $\mu$ M carboplatin .....	14
Figure 11: Development of UCD52-CR .....	15
Figure 12: Screening UCD52 and UCD52-CR.....	16
Figure 13: Objective remains within depth of field >95% of the time while scanning. ....	18
Figure 14: Processing data in real-time .....	20
Figure 15: Fine needle biopsy (FNB) sample preparation compared to bulk prep. ....	21
Figure 16: UCD52 screen of proteasome inhibitors.....	22
Figure 17: HCI09 screen of proteasome inhibitors .....	23
Figure 18 An example UCD52 cell resistant to 1 $\mu$ M bortezomib.....	24
Figure 19: HCI09 screen of CDK 4/6 inhibitors.....	25
Figure 20: UCD52 screen of CDK 4/6 inhibitor Abemaciclib, 24 vs 48 hr comparison.....	26
Figure 21: Additions to HSLCI system for cell isolation .....	29
Figure 22: Use of micropipette system .....	29
Figure 23: SU-DHL-6 & SU-DHL-10 differential sensitivity to idelalisib.....	31
Figure 24: Isolation and re-culture of idelalisib resistant cells .....	33
Figure 25: Mass and area distribution of etoposide-treated and etoposide-treated and enriched high- C <sub>12</sub> FDG and low- C <sub>12</sub> FDG H460 cells. ....	36
Figure 26: HSLCI observation of 1 $\mu$ M etoposide treated H460 cells and cell clusters.....	38
Figure 27: Biomass growth rates of etoposide treated and C <sub>12</sub> FDG sorted H460 cells from 0 to up to 9 days after treatment .....	40
Figure 28: HSLCI analysis of low-dose etoposide treatment shows variable patterns of growth arrest including a senescence phenotype.....	41
Figure 29: HSLCI analysis of H460 sorted, senescent cells shows that proliferative recovery originates in $\beta$ -gal positive cells.....	42
Figure 30: Cells that escape ABT-263 effects are smaller .....	43
Figure 31: HSLCI as a clinical screening tool .....	45
Figure 32: H1975 osimertinib-tolerant cell isolation.....	46

## List of Supplementary Figures

Supplementary Figure 1: Cell collection .....	54
Supplementary Figure 2: Idelalisib resistant isolation replicates .....	55
Supplementary Figure 3: PCR identification of drug resistant cells.....	56
Supplementary Figure 4: Replicates of drug sensitive cell isolations.....	56
Supplementary Figure 5: Cell clusters with smaller single cells grow faster after etoposide treatment .....	57
Supplementary Figure 6: TOK-001 HCI09 <i>in vitro-in vivo</i> correlation.....	58



## Abstract

### LIVE CELL BIOMASS TRACKING FOR BASIC, TRANSLATIONAL, AND CLINICAL RESEARCH

By Graeme F. Murray

A dissertation submitted in partial fulfillment of the requirements for the degree of Doctor of Philosophy at Virginia Commonwealth University

Virginia Commonwealth University, 2021

Major Director: Dr. Jason Reed, Associate Professor, Department of Physics

Single cell mass is tightly regulated throughout generations and the cell cycle, making it an important marker of cell health. Abnormal changes in cell size can be the first indication of dysfunction in response to environmental stimuli such as cytotoxic drugs. Described here is the further development of high-speed live cell interferometry (HSLCI) to concurrently measure the changes in single cell mass of thousands of cells over time. Critically, the high-throughput nature of HSLCI provides realistic pictures of tumor heterogeneity. This throughput enabled HSLCI to correctly predict *in vivo* carboplatin sensitivity of three triple negative breast cancer patient derived xenografts, while also characterizing the spectrum of drug response from apoptosis to senescence to drug resistance. HSLCI quantified previous qualitative observations of increases in cell size and losses in cell density in senescent cells, and importantly observed proliferative recovery in cells demonstrating these senescent characteristics. Furthermore, the addition of a micropipette system has enabled the isolation of rare (~1%) drug resistant cells for further study with molecular biology methods. Together, this work highlights HSLCI's versatility and potential for clinical, translational, and basic research.

# 1 Chapter 1: Biomass

This chapter provides an overview of single cell mass, how it is measured, how it is regulated, and the important role that cell mass plays in cell biology.

## 1.1 *Importance of the regulation of cell mass*

In mammalian cells, single cell size (volume) and dry mass (proteins, DNA, and RNA) are tightly regulated throughout generations with the average mother and daughter cells being roughly the same size and different cell types ranging between 5- 100  $\mu\text{m}$  in diameter [1, 2]. Maintaining this size and regulating growth are crucial for human survival. Immune cells must respond to infection but also not proliferate excessively to result in auto-immune disease. Dying cells must be replaced without causing carcinogenic overstimulation. The cell replacing the dying must serve the same function and remain the same size. If the daughter cell is too small, it might not have enough surface area to absorb nutrients, while if it is too big the cytoplasm may become too dilute to function properly [3].

In order to adaptively regulate size and mass on shorter timescales, cells take cues from the cytoskeleton through mechanosensitive ion channels and protein signals through kinase dependent ion channels to adapt size to environmental changes[2]. On longer time scales, size and growth are regulated by pathways such as mTor, MyC, and Hippo which can adapt protein and lipid synthesis in response to nutrition [4-6]. Yet even with this understanding, we can still only hypothesize on molecular mechanisms that couple division rate with cell size, the key to maintaining cell size generation after generation [1, 2].

While our knowledge of the regulation of cell size and growth is limited but expanding, we have extensive research on the dysregulation of cell size due to the study of the diseases that manifest from it. Cardiac muscle cells enlarge leading to cardiomyopathy, developmental brain disorders occur due to neuron shape or size dysregulation, and cancers grow due to mutations in regulatory pathways [1]. Through the lens of tightly regulated cell growth, the biomass response of single cells to environmental stimuli such as cytotoxic drugs can reveal the heterogeneity of a population. It is this heterogeneity in response to stimuli, specifically cancer drugs, that is the bane of oncology clinics everywhere. Initially promising drug responses often result in relapses after a small subpopulation of cells that were resistant to the initial treatment regrow the tumor [7-10]. Identifying and studying these subpopulations before clinical treatment could not only inform research into drug resistance but also when done on a large enough scale inform therapy for individual patients. The first step is developing a system that can scan tens of thousands of cells to identify small subpopulations with the picogram sensitivity necessary for identifying drug resistant cells after only 10-12 hours of monitoring.

## 1.2 *Measuring cell mass*

In the past 70 years, cellular mass has been measured through a variety of methods including first through biochemical stains and interference microscopy, and more recently mass spectrometry, microresonators, and electron microscopy [11-24]. All methods have only seen limited use in research and clinical settings due to issues of throughput, precision, or complexity [24, 25]. Recent advances in microfabrication and computing have unlocked the potential of using cell mass as a bio-marker at scale [3, 24, 25]. Methods benefitting from these advances fall into two categories, resonance sensors and optical modalities, each with their advantages and disadvantages:

### *Resonance sensors*

Resonance sensors use an array of cantilevers in fluid communication with one another along with delay channels which enable repeated measurement of the mass of suspended cells over time [26]. The suspended cell's or particle's mass is determined by the change in resonance frequency of the cantilever. The resonance frequency is changed by the difference in the particle's mass compared to the displaced fluid [20, 22]. To measure the resonance frequency, the cantilever is vibrated by either small embedded

piezoresistors or an external laser doppler vibrometer. This method enables 100 attogram precision in ideal conditions, but cells are measured one at time as they pass through the fluid channel in the cantilever, limiting measurement to 50-60 cells per hour [27, 28]. Drug resistant cells subpopulations which have been shown to lead to resistant cancer recurrence in patients can be present at only 0.2% of the population of the original tumor [7]. These methods do not yet have the throughput necessary to identify rare drug resistant cells or screen multiple drugs at once but are best suited to measuring a-tens of cells with extreme precision.

### Optical modalities

Quantitative optical measurement of living cells began in the 1950s utilizing Michelson interferometry (**Figure 1**), which can be traced back to 1887 when Michelson and Morley invented interferometry, disproving the existence of a luminiferous ether, winning America's first Nobel prize [12, 29]. Since both the 19<sup>th</sup> century and the 1950s, there have been leaps forward in both digital imaging and computing power.

Today interferometry is commonly used in industry to identify nanoscale aberrations or defects in surface morphology. The most famous example of this use was when interferometers were used to identify the defects in the primary lens of the Hubble telescope when it was first launched [30]. More recently interferometry was used for the first detection of gravity waves using interferometers with enough precision to measure the difference of a thousandth of a proton over 4 kilometers [31].

All these applications are based on the same principles. A light beam is split down two identical paths except for the presence or absence ("reference beam") of an object interest. These beams are then superimposed on each other forming an interference pattern. The interference pattern is caused by the difference in optical path length (OPL) caused by the presence of the object interest, in our case the living cell. Optical path length is equal to the integral of the index of refraction ( $n$ ) across the path from 0 to  $z$  that the light travels in the  $z$  direction.

$$OPL = \int_0^z n(x, y) dz$$

The index of refraction describes how fast light travels through a material, where  $c$  is the speed of light in a vacuum and  $v$  is the phase velocity of light in the material.

$$n = \frac{c}{v}$$

The optical path difference (OPD) can then be found by subtracting the OPL of the reference arm from the sample arm over the thickness of the sample,  $h$ :

$$OPD = \int_0^h n(x, y) - n_{medium} dz$$

From there integrating over the entire imaging surface ( $S$ ) in the  $x, y$  direction gives the total optical volume difference (OVD).

$$OVD = \iint_S OPD dx dy = \iint_S \int_0^h n(x, y) - n_{medium} dz dx dy$$

Living cells, specifically their proteins, DNA, and RNA, have a difference in index of refraction which is relatively constant and different than the media surrounding it [14]. This constant enables the OVD to be converted to the amount of material (dry mass) of the cell present. This OVD is directly proportional to the mass of the cell by number  $\alpha$  which is typically expressed as  $\frac{1}{\alpha} = 5.56 \frac{pg}{\mu m^3}$

$$\iint_S OPD dx dy = am$$

$$m = \frac{1}{\alpha} OVD$$

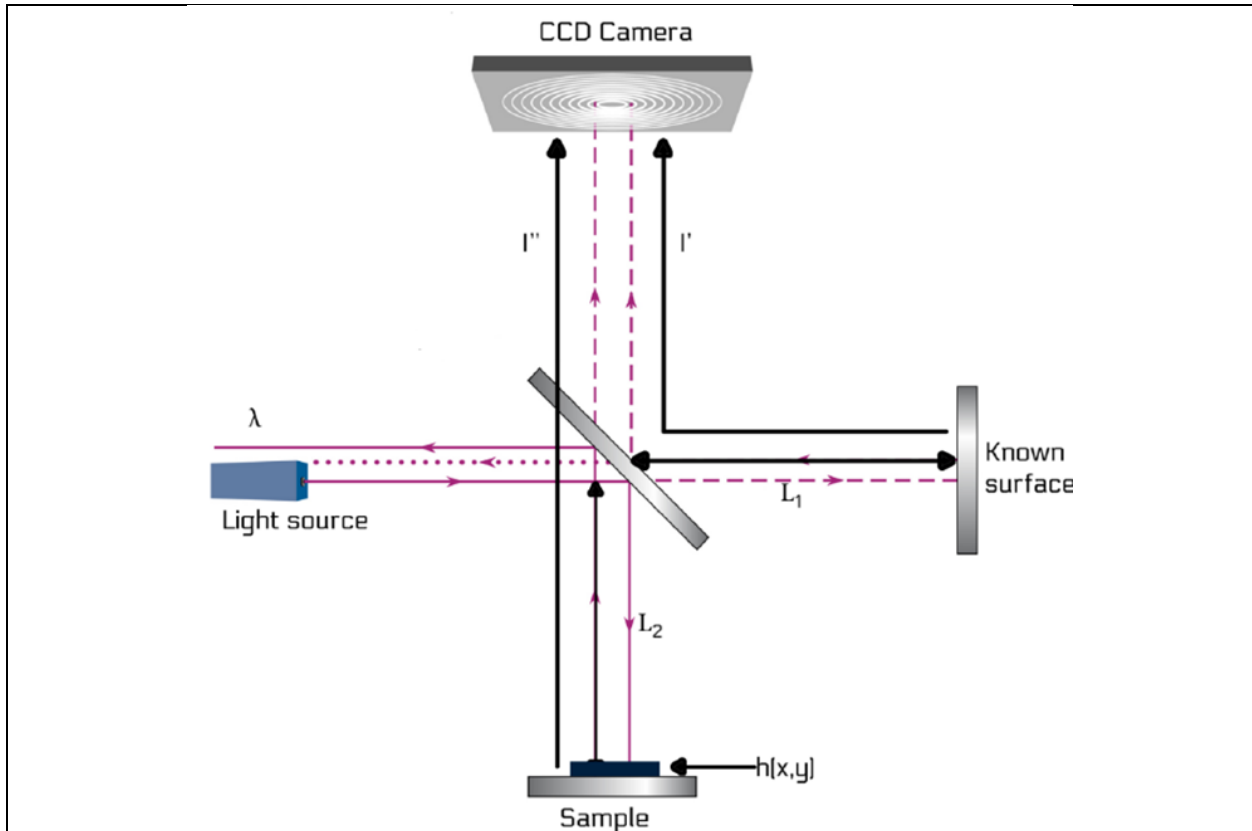


**Figure 1: Michelson Interferometry**

Coherent light is emitted and then split to go down two identical arms. The light travels down the sample path (L2) and reference path (L1) which are identical except for the sample. The light is then recombined forming an interference pattern that is captured by a CCD camera. From the interference pattern, the difference in optical path length (L1 and L2) can be calculated enabling the calculation of the mass of the sample present. Adapted from: [32]

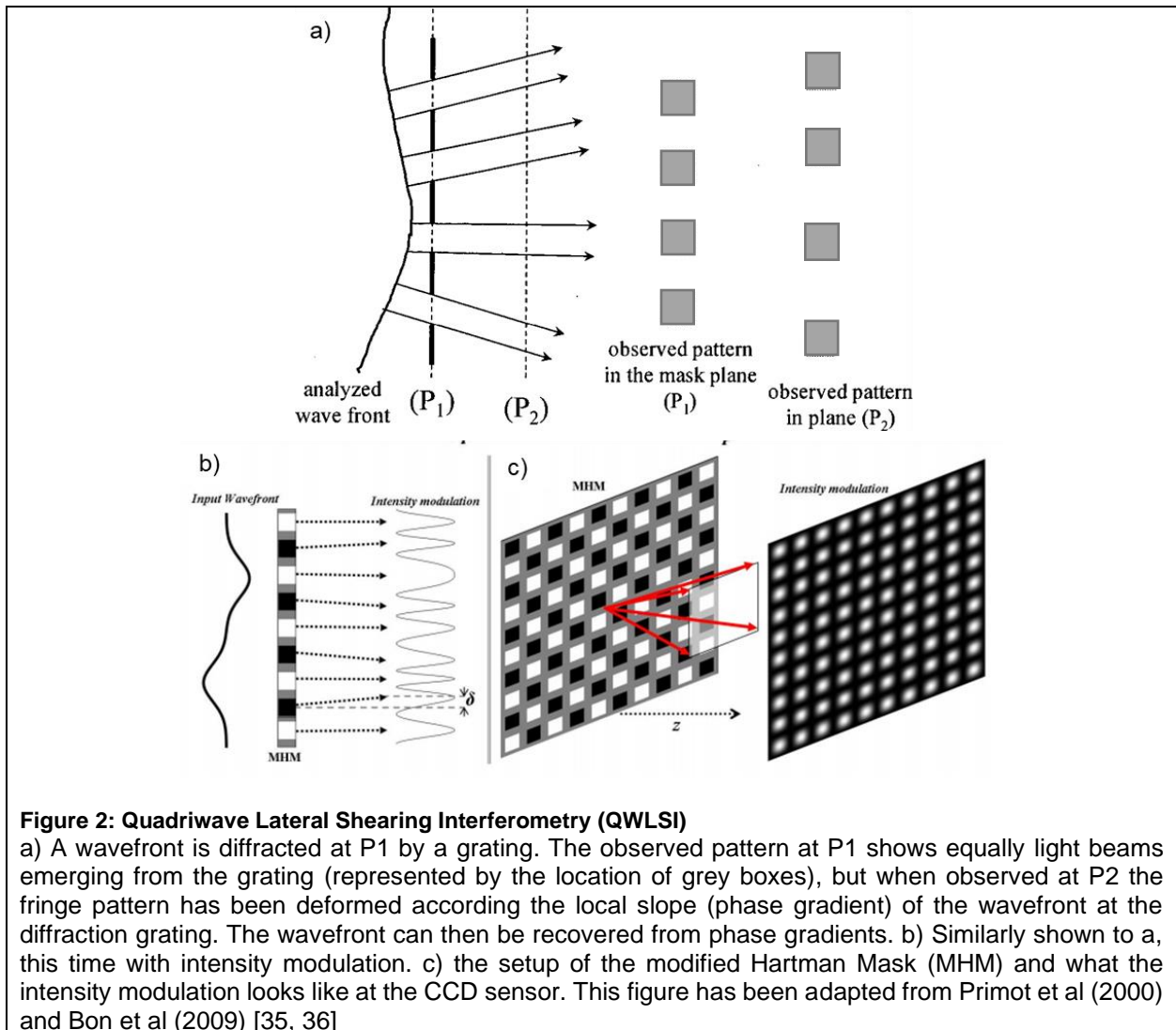
Since 1887, variations on interferometry have developed into a field of its own. Some methods such as Optical Coherence Tomography (OCT) which relies on low-coherence interferometry have become commonly used in ophthalmology clinics to provide detailed images from within the retina [33, 34]. Scanning of the mirror in the reference arm allows for the development of a reflectivity profile of the sample as only light reflected at the same depth of the mirror will interfere to form a pattern. This enables visualizations of structures with micrometer resolution [33, 34].

While there are countless variations of interferometry such as OCT, this work will focus on those that can be used to measure cell mass. A Michelson interferometer can be used to measure cell mass over time and has been done by our group [18]. But this type of setup necessitates a second reference arm which adds bulk to any system. To build a system that could take phase images in parallel to fluorescence images and not require a second reference in arm in tight space, our group explored quadriwave lateral shearing interferometry (QWLSI).

In QWLSI, non-laser coherent light is passed through the living cells and then sheared by diffraction grating (millimeters in front of the camera) into multiple (four) replica wavefronts. These wavefronts are then

recombined to form an interference pattern at the CCD camera sensor. The phase data is then calculated from aberrations in the Fourier harmonics of the intensity peaks caused by local phase gradients as light passes through the diffraction grating. An example in one dimension is shown in **Figure 2a**. Looking at the analyzed wavefront at the mask ( $P_1$ ) and after the mask ( $P_2$ ) shows that the light beams emerging from the diffraction grating at  $P_1$  are deflected with respect to the phase gradients, the local slopes of the wavefront. The dependence of the fringe pattern on the local phase gradients at the point of diffraction enables the phase gradients to be recovered from the fringe deformation by means of Fourier deconvolution around the interferogram fringe frequency.

The phase and field intensity are then calculated by integration. This process is known as unwrapping. A similar situation is shown in **Figure 2b**, this time showcasing the intensity modulation depending on the slope of input wavefront. Finally, **Figure 2c** shows what the diffraction grating looks like in 2-dimensions. The grating also known as a modified Hartman Mask (MHM) is made up of a superposition of an amplitude grating of period  $p$  and a  $\pi$ -shift check board (phase grating of period  $2 \cdot p$ ). This grating is optimized to diffract more than 90% of the light energy into the four first orders carried by the four wave vectors allowing calculations to use just the first four orders [35, 36].



This setup removes the need for a reference arm but does require an additional step of integration when processing the data and comparison to a reference image taken without the sample (without cells, just media) in place.

## 2 Chapter 2: Previous work on High Speed Live Cell Interferometry (HSLCI)

This chapter provides an overview of the HSLCI system prior to the work described here utilizing QWLSI. Most work was performed by either Kevin Leslie, Daniel Guest, or Dian Huang.

### 2.1 Overview of original HSLCI system

#### Imaging setup

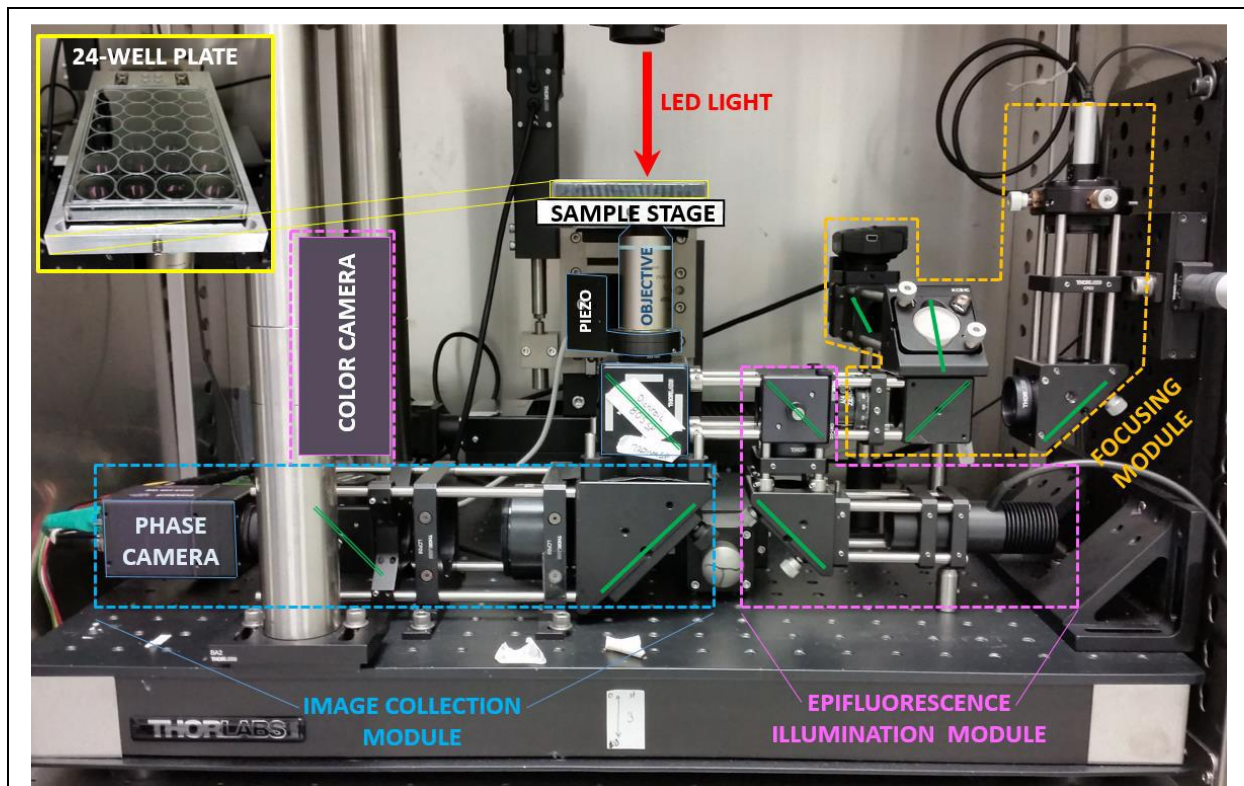


**Figure 3: Overview of original HSLCI setup**

Cell samples are placed in a 24 well plate and secured in a custom sample stage (solid yellow). The sample stage is connected to 3 linear translational motors that can move it in the x, y, & z directions. During operation the stage is translated from 0 to 100 mm in the y direction, and then moved to a new spot in the x direction and then scanned from 100 to 0 mm in the y direction. Focus is maintained by both the z-motor (coarse) and piezo actuator (fine) which is controlled by the focusing module. The focusing module maintains the distance between the objective and glass bottomed plate through adjustment of the reflection of an infrared laser by the piezo actuator as read by a quadrant photodiode. A 660 nm LED light above the sample stage is strobed (4 fps) to coincide with the exposure time of the phase camera. This light is directed to the phase camera through the image collection module. Finally, an epifluorescence illumination module shines light to excite any fluorophores present whose emissions are then directed toward the color camera. Depending on the fluorophores used filters need to be adjusted to allow the correct wavelengths to pass. Adapted from [37]

The HSLCI platform, **Figure 3**, consists of a custom-built inverted optical microscope coupled to an off-axis quadriwave lateral shearing interferometric camera (SID4BIO, Phasics, Inc.). Cells are imaged in single, standard-footprint (128 mm x 85 mm), glass-bottomed, multi-well plates secured in a custom sample stage.

The sample stage is connected to three linear translation motors which move in the x, y, and z directions. The sample sits right above the objective, which is either a 10x, 20x, or 40x Nikon Plan fluorite objective. As the sample stage is moved 100 mm at 2mm/s (acceleration of 1mm/s<sup>2</sup>) in the y-direction, a 660 nm LED light is strobed at 4 fps to coincide with QWLSI camera's exposure time.

The glass bottom of the plate is not perfectly smooth, so focus is maintained coarsely by the linear translation motor and more finely by a piezo actuator. The motor and actuator are controlled by the focusing module (**Figure 4**) consisting of infrared laser, quadrant photodiode (QPD) and proportional integral derivative (PID) controller. The infrared laser is reflected off the bottom of the plate at the air-glass interface due to a difference in the index of refraction. This reflection is then sent toward the quadrant photo diode and read by the diode as a voltage. At the beginning of each experiment the operator sets an optimal focus position which is stored as a voltage from the diode in the PID controller. As the plate moves, the distance between the objective and bottom of the glass plate changes. The reflection of the infrared laser changes as does the voltage read by the QPD. The PID sense the change in voltage on QPD and sends a new (separate) voltage to either expand or contract the piezo actuator that the objective sits on to bring the image back into focus. This operation is happening thousands of times a second to ensure the imaging plane remains within the depth of field of the objective.

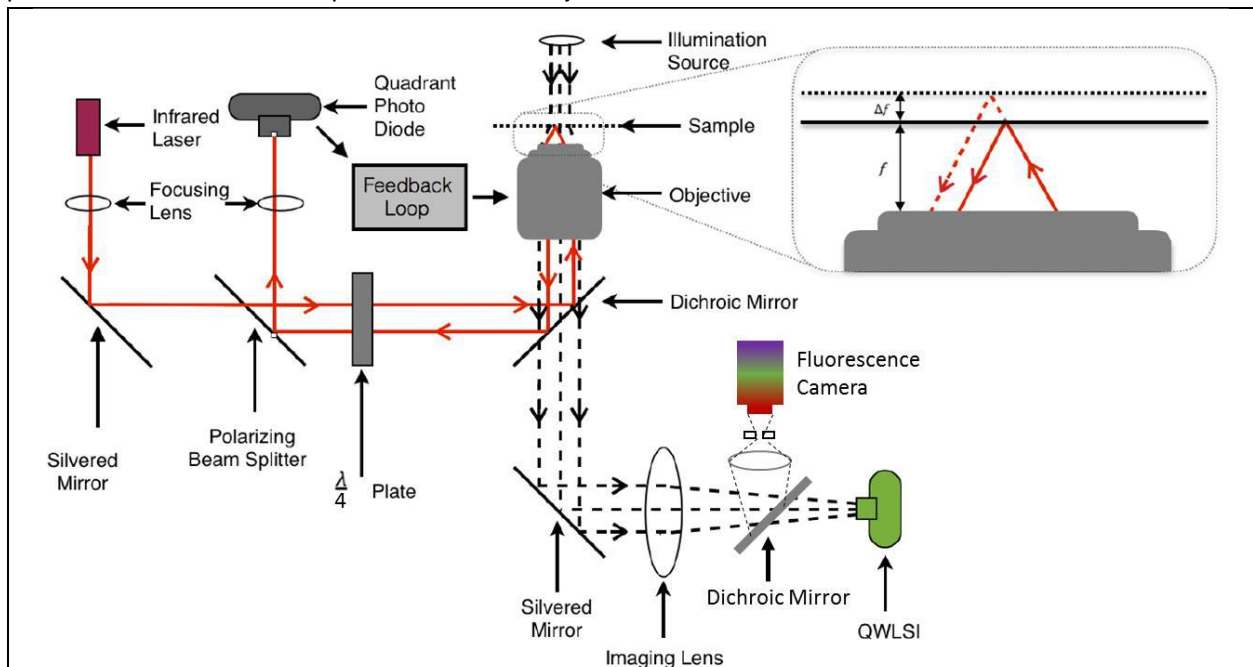


**Figure 4: Ray diagram of focusing module**

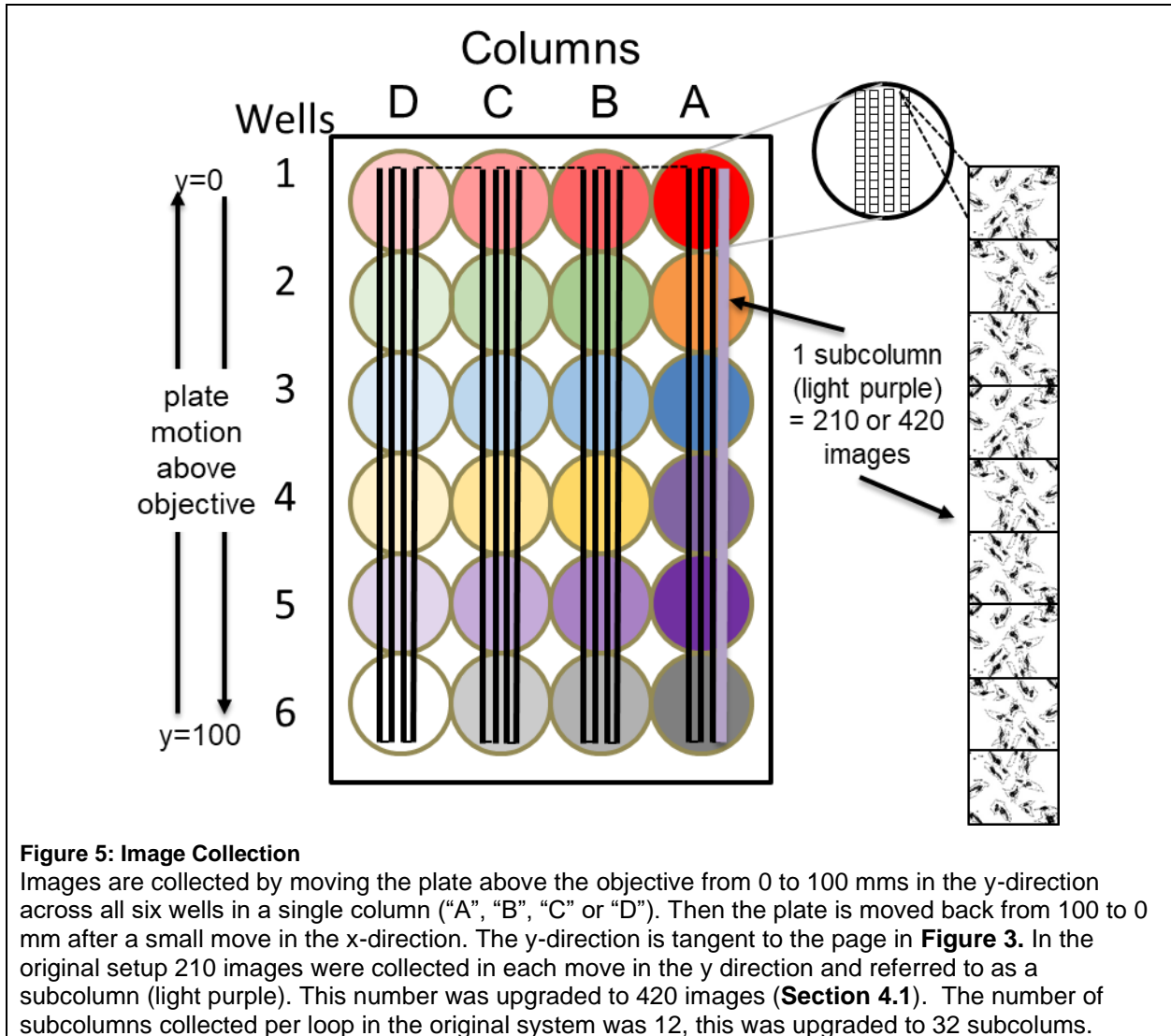
Samples are imaged in glass bottom plate with images collected by the off-axis QWLSI. Dynamic focus stabilization is maintained as the plate is scanned at 2mm/s over the objective. An infrared laser reflects at the air glass interface at the bottom plate. This reflection is then captured by the quadrant photodiode (QPD) and interpreted as a voltage. Distance  $f$  is the focus position set at the beginning of the experiment from the bottom of the plate to objective. As the plate moves in the y direction a change  $\Delta f$  is created due to fluctuations in glass created during manufacturing. This in turn changes the voltage read by the quadrant photo diode. This change in voltage is sent to the PID controller (Feedback Loop) which then adjusts a voltage sent to a piezo actuator underneath the objective to bring the distance back between the objective and plate back to  $f$ . Note, epifluorescence module not shown. Adapted from Guest, D. 2017 [38].

The HSLCI platform is installed inside a standard cell culture incubator (Steri-Cult CO<sub>2</sub> Incubator, ThermoFisher) to maintain conditions for optimal cell growth

*Processing*

210 interferograms at a time (0 to 100mm in y direction) are collected as Motion JPEG 2000 (".mj2") files. ".mj2" files are simply a sequence of JPEG 2000 files which can then be accessed one by one for processing. These 210 interferograms are referred to as "subcolumn" (**Figure 5**). Each column of wells ("A", "B", "C", or "D") consists of only two subcolumns.

Processing is completed by an automated custom MATLAB pipeline. First, images are unwrapped by the manufacturer's software (see **Section 1.2.** on QWLSI). These phase images have low frequency background noise inherent to lateral shearing interferometry. This and other noise is removed through a flattening process. First, a polynomial is fit to background curvature in the image line by line and then subtracted out. Next, the image is passed through a low pass filter to smooth the high frequency pixel-pixel noise inherent in any imaging due to each pixel generating its own independent noise.



Next cells are detected in these flattened images by spatial derivative edge detection kernels which look for sharp changes in OPL difference between neighboring pixels. The optical volume of each cell in an image is then recorded and can be converted to mass. Cells are then tracked from image to image and a linear fit is performed to measure each cell's hourly growth rate. Quality filters are then applied to only consider cells with hourly growth rates with standard error of the residuals <0.2%.



On a single Intel Core i7, unwrapping takes approximately 500 ms while processing (flattening and segmenting) takes around 500-1000 ms. Due to manufacturers restrictions, unwrapping cannot be done in parallel, processing can.

## 2.2 HSLCI study in melanoma

As a proof of concept that biomass tracking in response to drug treatment could identify drug resistant and drug sensitive cells, our group screened two melanoma cell lines: the vemurafenib-sensitive M249P and vemurafenib-resistant and GFP-labeled M239R4, and attempted to identify single cells as either M249P (sensitive) or M249R4 (resistant) based off biomass growth in response to vemurafenib.

M249P and M249R4 cells were plated separately and in a 1:1 mixture and then monitored with an older setup of Live Cell Interferometry (LCI). Cells were then dosed with 5 $\mu$ M vemurafenib for 24 hours and then monitored by LCI for 10 hours. As phase images were being taken every 10 minutes, every fifth loop (50 minutes) fluorescent images were taken to be used to identify cells as either the GFP positive M249R4 or the GFP-negative M249P (**Figure 6a-c**).

Biomass growth rates were then used as an identifier for cells as either drug resistant or drug sensitive and compared to cell identification based on fluorescence (**Figure 6d,e**). Receiver-Operator Curve (ROC) analysis confirmed that biomass growth is a robust predictor of drug sensitivity even when the two cell lines are combined in the same well (AUC 0.88). But as would be expected with any cell line, some M249R4 cells were dying or showed little to no growth, while more surprisingly some M249P cells showed continued growth despite vemurafenib exposure (**Figure 6d**). This biomass growth in nominally drug sensitive cells showcases the heterogeneity of response in this patient derived cell line. These two cell lines are isogenic, M249R4 was evolved from M249P through repeated exposure to vemurafenib. These outlier M249P cells, which continued growth in response to vemurafenib, may be the precursor cells that evolved into the M249R4 line.

With the efficacy of single cell biomass growth as an indicator of drug sensitivity established, our group decided to use this indicator to find promising drugs to treat the M249R4 line. This is the first attempt to establish the feasibility of simulating real-world clinical decision making using single cell biomass growth. As will be discussed more in **Section 3.1**, after a patient develops resistance to first-line therapy, physicians have to make decision on what drugs to try next. Typically, these decisions are based off prognostic factors, patient health, and genetics [39]. There is interest in personalizing and informing decision-making more precisely through the use of quick *ex-vivo* drug testing against a patient's tumor (**Section 3.1**).

In the case of melanoma, salvage therapy can continue to target BRAF or instead target MEK, another kinase. To simulate a physician deciding on which inhibitor for this M249R4 "patient", our group screened four MEK inhibitors (cobimetinib, selumetinib, trametinib, binimetinib) and one BRAF inhibitor (Dabrafenib) (**Figure 7**). The \* indicated the max serum concentration (C<sub>max</sub>) as measured in clinic trials [24]. Using this C<sub>max</sub> as a benchmark, unsurprisingly the BRAF inhibitor dabrafenib showed little effectiveness

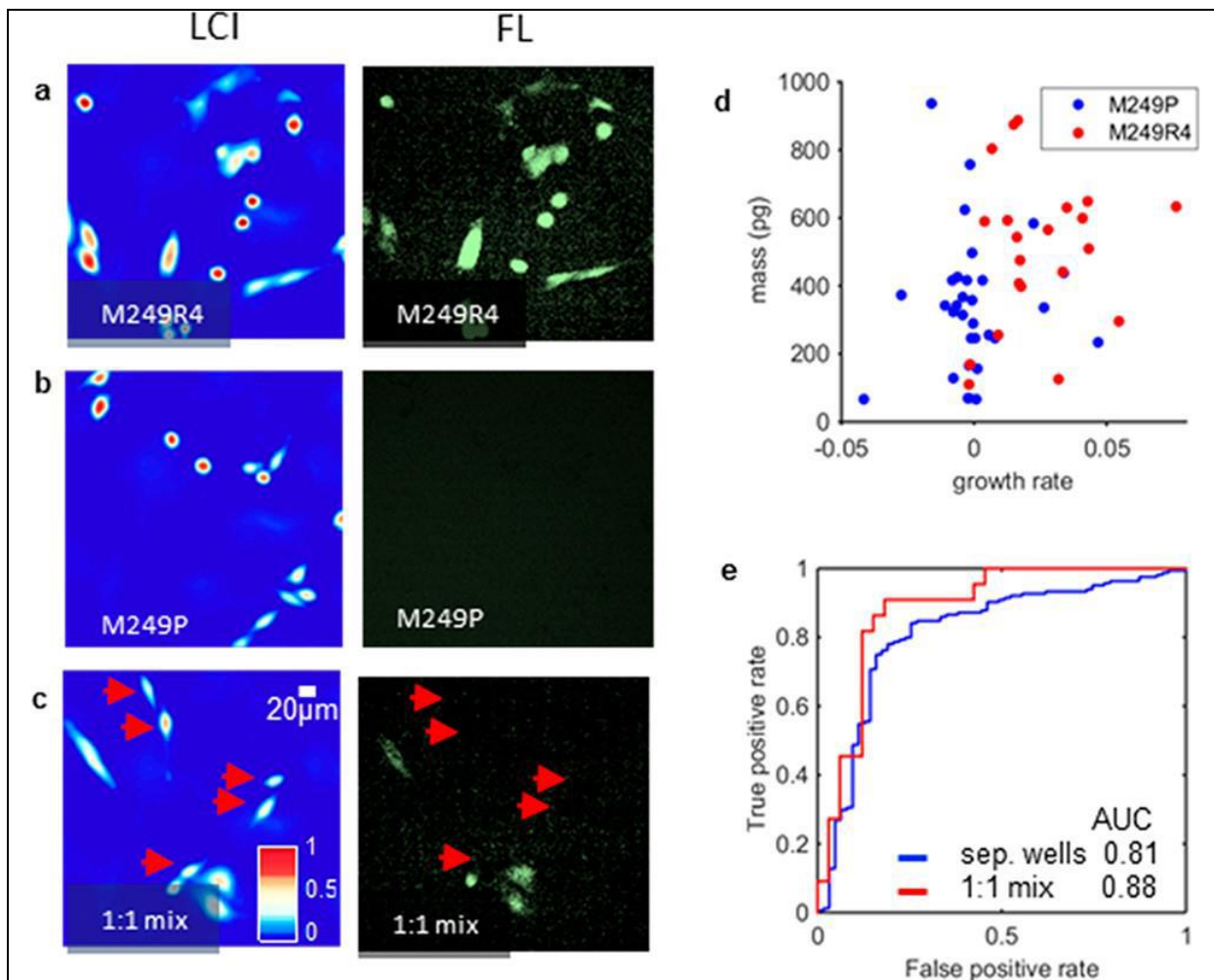


**Figure 6: Identifying drug resistant and sensitive cells in a mixed population**

a). Optical thickness as measured by LCI (left) and fluorescent images (FL, right) for M249R4-GFP positive cells. b) LCI and FL images of M249P cells. c) LCI and FL images of a 1:1 mixture of M249P (red arrows), and M249R4 (unlabeled) cells. d) Biomass vs growth rate of 1:1 mixture. M249P, vemurafenib sensitive, cells are in blue while M249R4, vemurafenib resistant cells are in red. Growth rates taken after 48 hours of exposure. e) ROC curving of classifying M249P vs M249R4 cells based on biomass growth rate versus true positive/negative of fluorescence. Adapted from Huang et al [24]

when compared to the control (DMSO). In contrast MEK inhibitors cobimetinib and trametinib reached their maximum effectiveness below their  $C_{max}$ . While binimetinib and selumetinib showed effectiveness, neither reached their maximum effect below  $C_{max}$ , with selumetinib performing slightly better.

In this simulated case, the physician could incorporate this new information into their decision making. Binimetinib would be an unlikely choice for salvage therapy while one would potentially choose between cobimetinib or trametinib based on experience, side effects, and patient preferences.

This work showcases the power of HSLCI in screening and identifying effective drugs by increased throughput to measure multiple agents in parallel. However, this remains just a simulation and results must be correlated to *in vivo* treatments.

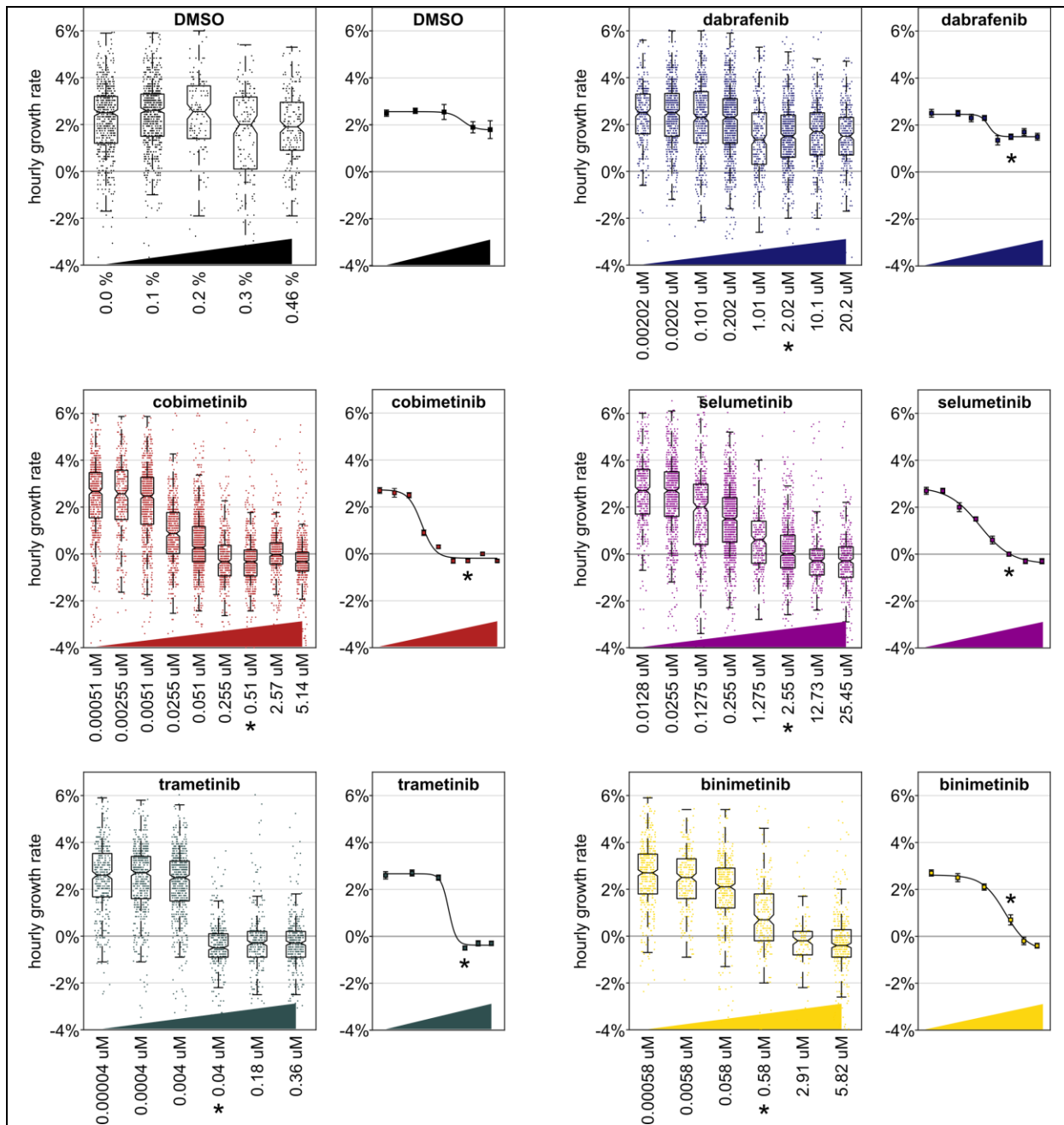


**Figure 7: MEK inhibitor screen on vemurafenib resistant melanoma**

M249R4 vemurafenib resistant cells were plated into 24 well plates and given log scale dosages of each inhibitor or the vehicle DMSO. After 24 hours of incubation, plates were imaged by HSLCI for 10 hours. Hourly growth rates for individual cells, indicated by scatter plots in box plots, were automatically calculated by linear fit to biomass versus time data. Data for each drug-dose combination was the sum of three independent experiments. Median population growth rates from all three repeats were plotted and fit with sigmoid curves. Error bars represent the 95% confidence interval in the median. The dosages marked by \* correspond to maximum serum concentrations measured in clinical trials at therapeutic dosages. Adapted from Huang et al. [24]

### 3 Chapter 3: HSLCI predicting *in vivo* carboplatin sensitivity

The next step in establishing potential uses for HSLCI requires a model system that enables correlations of HSLCI results to *in vivo* treatment. For this, our group used triple negative breast cancer (TNBC) patient derived xenografts (PDX) models which are discussed further below.

#### 3.1 *Ex vivo* methods for predicting patient drug sensitivity

Approximately one third of triple-negative breast cancer (TNBC) patients experience drug-resistant metastatic disease that is often fatal [40]. Current guidelines attempt to personalize cancer therapy based on a patient's general state of health, clinical tumor staging, hormone receptor status, and mutation profile [41]. But these guidelines are often inadequate at predicting therapeutic resistance before bulk tumor growth restarts and potentially metastasizes [41-43].

A recent study has demonstrated the necessary capabilities for such a test to successfully detect drug resistant clones before treatment [7]. Following 20 TNBC patients, Kim et al. performed single cell DNA and RNA sequencing pre-, mid-, and post-treatment. In 10 patients treatment was successful, while in 10 others the tumor persisted. After identifying the dominant clones post treatment in patient's resistant tumors, Kim et al performed deep sequencing on the corresponding pre-treatment tumors. In 10/10 cases they were able to identify the dominant drug resistant clones in the pre-treatment tumors as rare sub clones with prevalence ranging from 0.2-2%. This necessitates that any test must be able to detect cells in the 1/1000 range.

One potential assay for early detection of drug resistant clones is liquid biopsies. Liquid biopsies detect circulating biomarkers, exosomes, microRNAs, circulating tumor DNA, and tumor cells in blood. These blood samples can accurately reflect tumor heterogeneity and are easy to acquire. Yet, this approach still depends on sequencing and requires an understanding of the clinical significance of each detected mutation. This dependency leads to a high specificity (>95%) but poor sensitivity (66%) for predicting therapeutic resistance in patients [44]. If a known resistance-related mutation is detected, liquid biopsy methodologies reliably predict patient therapeutic sensitivity. However, in more than one third of cases, potential resistance-related mutations are not found, or the significance of detected mutations is unknown, resulting in the incorrect prediction of susceptibility to therapeutics.

Recent improvements in tumoroid culture allow for the *ex vivo* proliferation of primary patient samples. These advances make it feasible to screen patient samples for therapeutic sensitivity against a large panel of potential drugs. [45, 46]. However, this technology suffers from cost and procedural complexity drawbacks that limit its utility in clinical settings. Furthermore, as implemented, these assays rely on the bulk averaging of fluorescent viability signals acquired from an entire sample well (representing a heterogeneous cell population), making the detection of minute (1/1000) subpopulations inherently impractical.

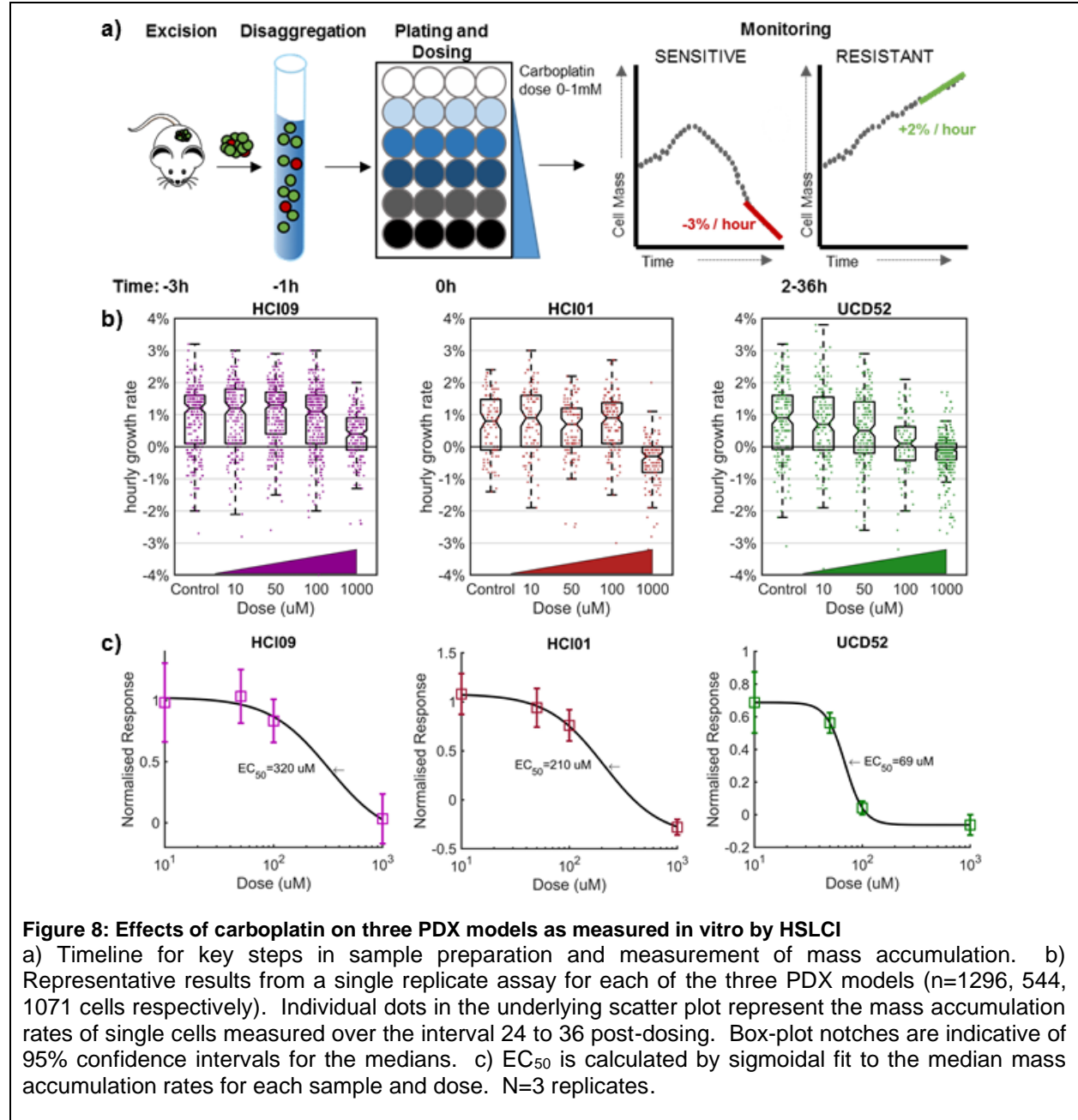
Alternatively, analyses of changes in cancer cell biomass have shown promise in rapidly assessing drug sensitivity and fulfilling these requirements [21, 47]. In cell line models of breast cancer[48] and melanoma[49], loss in cellular biomass has been shown to correlate with drug sensitivity, and was often detectable before classical apoptotic signals. A major limitation of this previous work is that it is not obviously extensible to real patient tumors owing to potential artefacts that would be generated by the removal of cells from their microenvironment and deleterious effects of excision and purification.

To test if the analysis of biomass change could function as *ex vivo* test, patient-derived xenograft (PDX) models, which are human TNBC tumors growing in immunodeficient mice, were excised, and enzymatically disaggregated into a single cell suspension. Rapid and accurate biomass accumulation-based prediction of *in vivo* sensitivity to the chemotherapeutic drug carboplatin was performed and *in vitro* biomass results were correlated with *in vivo* treatment results. Importantly, while not fully recapitulating a human tumor, owing to the absence of complete tumor: immune system interactions and other factors, PDX preclinical cancer models have been shown to maintain the gene expression heterogeneity and histology seen in

primary tumors [50]. As a result, PDX models are a much more relevant platform on which to evaluate the translational potential of biomass accumulation drug response assays than are cell lines and can serve as pre-clinical test for patient tumors.

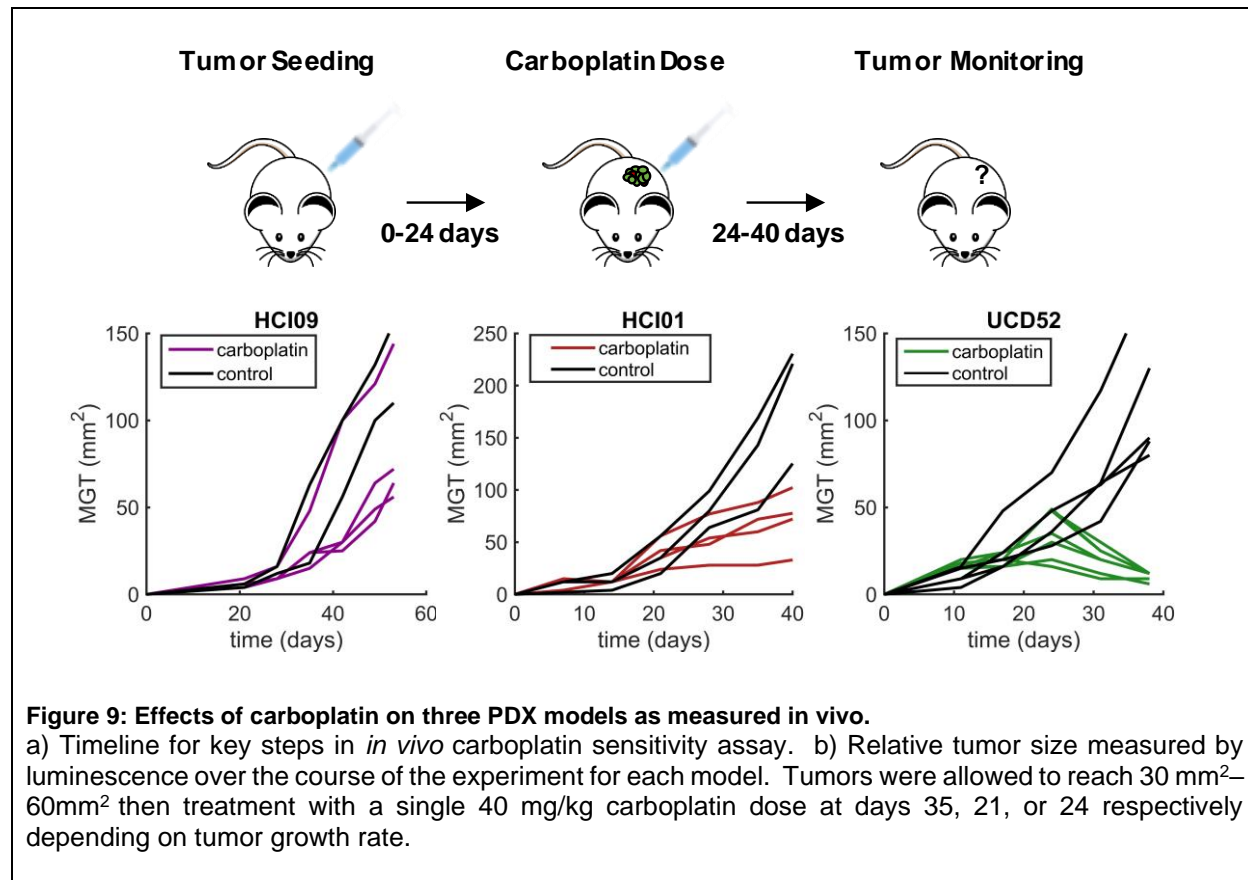
In these studies, we used our previously described (Section 2.1) optical cell biomass measurement system, the High Speed Live Cell Interferometer (HSLCI) [49]. Biomass accumulation kinetic responses were determined by continuously measuring single cells or small cell clusters every 10 minutes. Assay results are obtained in approximately 40 hours from sample excision, which is a sufficiently rapid turnaround time to inform subsequent therapy selection in patients. Further, quick turnaround limits the amount of time for potential genetic or epigenetic changes to occur due to *in vitro* culture.

### 3.2 Effects of carboplatin on PDX models



The *in vitro* response to carboplatin of three TNBC PDX models (HCI01, HCI09, and UCD52) were monitored following the timeline and protocol described in **Figure 8a**. Tumors were excised and enzymatically digested into single-cell suspensions. Following this, cells were placed in a 24-well glass bottom plate with media, dosed with carboplatin, and then monitored for 36 hours using the HSLCI system. As carboplatin is not cell cycle specific, we anticipated detecting responses within 36 hours post dosing. Each assay included parallel measurements across a log-scale range of carboplatin doses in the same plate. The 1X dose in this range (40-70  $\mu\text{M}$ ) corresponds to the equivalent maximum serum concentration measured in patients receiving FDA-approved therapeutic doses of carboplatin (**Figure S1a**)[51]. Example results from one replicate assay with data from 24-36 hours after dosing for each PDX model are shown in **Figure 8b**. The data from three independent replicates was compiled to calculate an  $\text{EC}_{50}$  and plot a dose response (**Figure 8c**). The *in vitro* assays predicted that the PDX model UCD52 ( $\text{EC}_{50}$  69  $\mu\text{M}$ ) would be substantially more sensitive than either HCI01 ( $\text{EC}_{50}$   $2.1 \times 10^2 \mu\text{M}$ ) or HCI09 ( $\text{EC}_{50}$   $3.2 \times 10^2 \mu\text{M}$ ) models to a single equivalent dose of carboplatin administered *in vivo*.

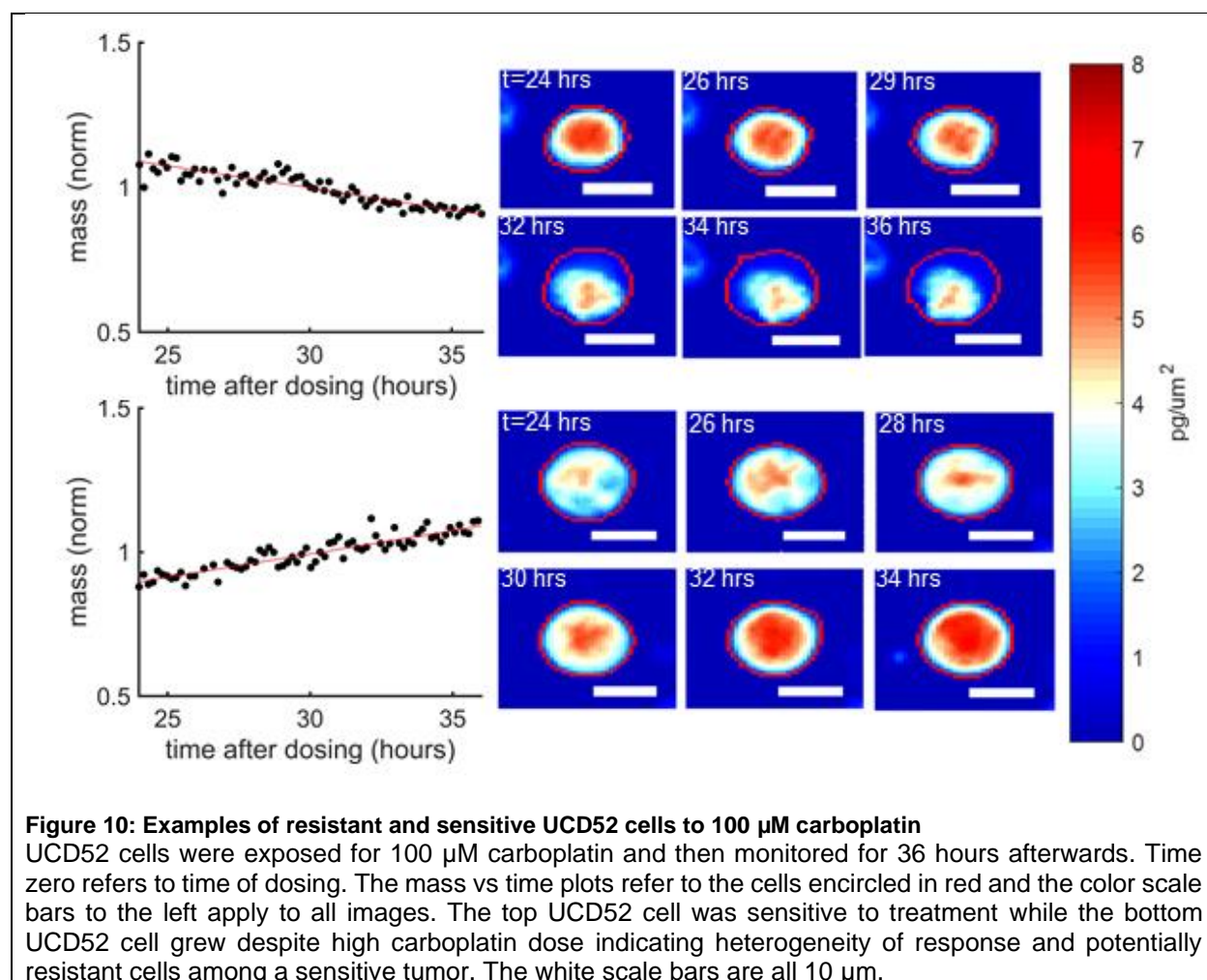
*In vivo* studies (**Figure 9a**) were performed by first seeding and then expanding mammary tumors in all three TNBC models. Single dose administration of vehicle or carboplatin at 40 mg/kg was performed on days 21, 24 or 35 depending on tumor growth. This dose approximates to around  $3.3 \pm 1.4 \text{ mg} \cdot \text{min}/\text{ml}$  in humans [51, 52]. Relative tumor size was determined daily in live animals by luminescence measurements, up to day 40. As predicted by the *in vitro* assay, the UCD52 model was the only PDX model to demonstrate a decrease in tumor size (**Figure 9b**). Tumors continued growing in both HCI01 and HCI09 models after treatment, with HCI09 growing more aggressively, a result concordant with the higher  $\text{EC}_{50}$  for HCI09 measured in the *in vitro* biomass accumulation assay.



### 3.3 Identification of carboplatin resistant single cells in carboplatin sensitive UCD52

As shown in **Figure 8b**, the biomass accumulation rates of cells within the measured populations of all three TNBC PDX models exhibited significant heterogeneity. Under the imaging conditions used, this heterogeneity in biomass accumulation rates represents biological variation and not measurement noise[47, 49]. Of particular interest were cells which demonstrated robust growth despite a substantial population-level dose-dependent loss of biomass. These cells could be analogous to subpopulations of drug resistant cells seen in patient TNBC tumors, which are subsequently selected for undesirable expansion or persistence by drug treatment, making them responsible for the recurrence of tumors often seen in TNBC. Therefore, identification and isolation of these 'non-responder' cells for further genomic and phenotypic characterization may aid in our mechanistic understanding of drug response heterogeneity in cancer.

**Figure 10** shows two representative examples of the biomass accumulation responses from individual cells from the most sensitive PDX model, UCD52, after treatment with 100  $\mu\text{M}$  carboplatin, which is higher than the maximum concentration experienced in humans. These cells showed biomass accumulation rates of -1.5% and 2.3% per hour between hours 24 – 36, post-treatment. Interestingly, during hours 24 – 36 post-treatment, in this representative experiment 47 cells, or 16% of surviving cells at 36 hrs exposed to 100  $\mu\text{M}$  carboplatin, gained biomass at a rate of 1% or more per hour. However, the valid percentage of 'non-responders' in the original population is likely far lower, as the number of living cells measured at later time points is significantly reduced, relative to pre-dosing levels, due to treatment.



### 3.4 Development and screening of UCD52-CR

To simulate the development of drug resistance frequently seen in patients, the *in vivo* sensitive model, the Harrell Lab treated UCD52 repeatedly with carboplatin until it no longer responded (Figure 11). A crucial hurdle for HSLCI is distinguishing UCD52 from UCD52-CR as the key to clinical screening is predicting *in vivo* sensitivity. When tested in three separate experiments, (UCD52 run again), UCD52 was distinguished from UCD52-CR with great certainty ( $p < 0.0001$ ). The  $EC_{50}$  of UCD52-CR increased to  $104 \mu\text{M}$  up from  $54.6 \mu\text{M}$  in UCD52.

The observation of resistant cells in UCD52 by HSLCI (Figure 8 & Figure 10) before the development of resistance *in vivo* demonstrates another avenue for clinical and translational applications. The first question to answer is: are these the cells that lead to the formation of UCD52-CR? If these resistant cells could be isolated it could not only teach us more about the development of drug resistance, but if developed enough inform potential therapies to prevent the development resistance in patients. Such work first requires the construction of isolation system (section 6.1) along with real-time data processing (section 4.2) and extensive testing.

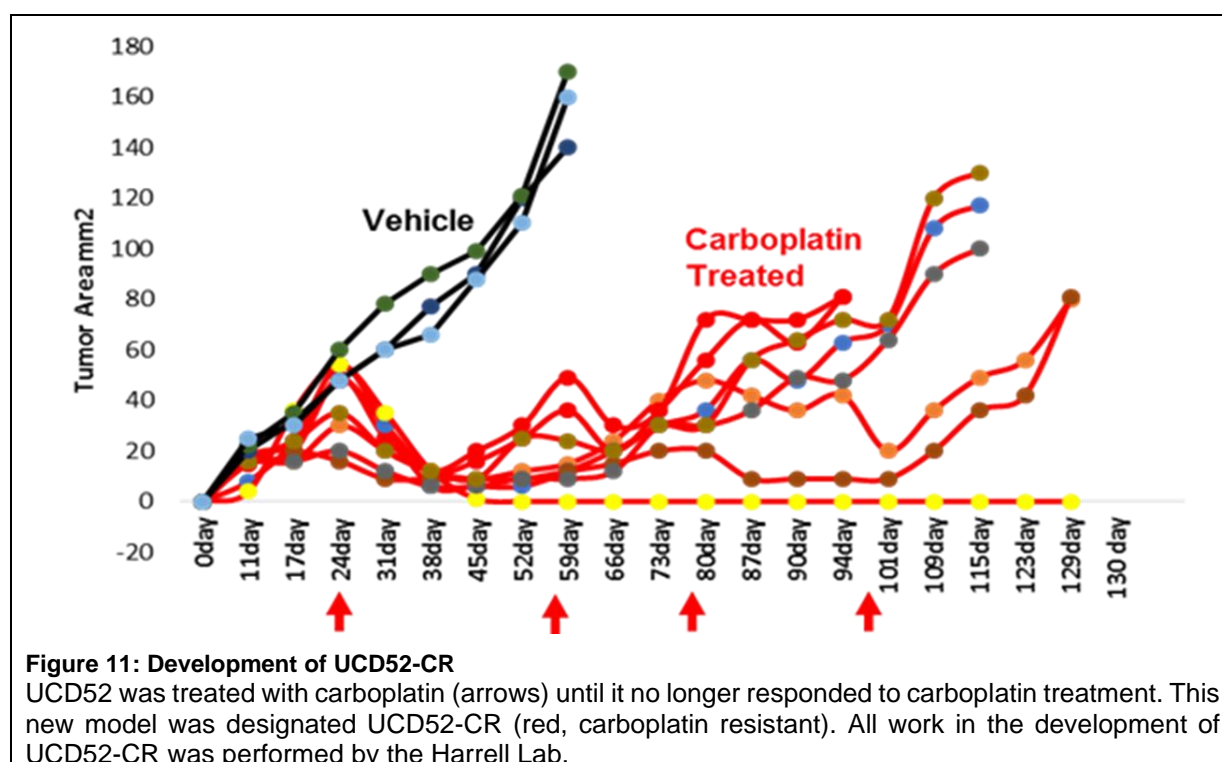
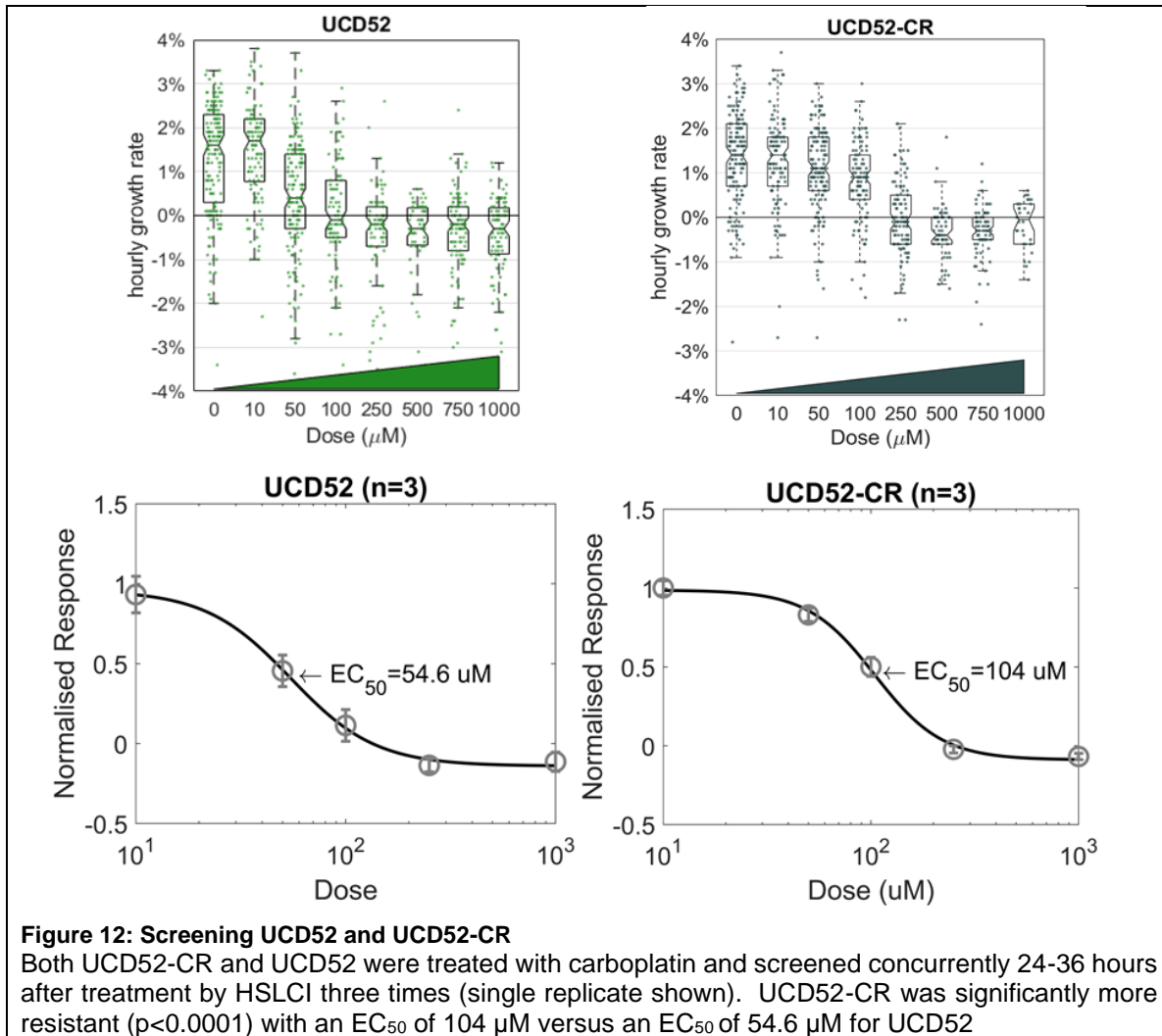


**Figure 11: Development of UCD52-CR**

UCD52 was treated with carboplatin (arrows) until it no longer responded to carboplatin treatment. This new model was designated UCD52-CR (red, carboplatin resistant). All work in the development of UCD52-CR was performed by the Harrell Lab.





### 3.5 Assay details

During tumor resection, disaggregation, and enzymatic digestion, only large pieces of debris are filtered out. Furthermore, beyond the surgical excision step, there is no active selection of breast cancer cells. As a result, the cells measured by the HSLCI are a combination of stromal and tumor cells. In previous fluorescence associated cell sorting experiments that specified epithelial and stromal cells, between 80-85% of cells were found to be cancer cells [53]. While a lack of biomarker-based tumor cell selection increases the ease of use and decreases the expense of each HSLCI run, the presence of non-tumor cells and pieces of cell debris whose biomasses remain static could obscure measurements.

These challenges are overcome using two strategies. First, as PDX tumor cells are non-adherent, they remained in 3D spherical shape and relatively dense with many PDX cells having subregions of biomass density over 8  $\text{pg}/\mu\text{m}^2$ . This 3D shape causes PDX cells to remain in a focal plane distinct from stromal cells, such as fibroblasts which attach to the bottom of the plate. This allows for the HSLCI to focus on the imaging plane directly above the bottom of plate on cells that are not attached. Second, fibroblasts have a typical area of around 3,600  $\mu\text{m}^2$ , whereas unattached cancer cells have an area of approximately 200-800  $\mu\text{m}^2$  [54]. This size disparity allows for the rapid resolution of cell type. Future analyses could leverage distinct phenotypic features of fibroblasts, such as lamellipodia, which decrease circularity and further distinguish stromal cells from tumor cells. Finally, debris are easily distinguished by their low biomass,

allowing *in silico* exclusion. Importantly, the same filtering methodology was applied across all three PDX models evaluated in these experiments. Definitive growth response signals were detected in all three PDX models.

### 3.6 Conclusions

These study results demonstrate HSLCI's ability to rapidly quantify the drug sensitivity of single, freshly explanted tumors cells, within 40 hours of excision. This time scale is feasible in the clinic as it is the same as widely used antibiotic susceptibility tests. This builds upon previous work with the HSLCI platform that quantified single-cell sensitivity of melanoma cell lines to vemurafenib[49] and overcomes the lack of *ex vivo* cell proliferation seen in most cancers, including these TNBC PDX models[53].

To succeed as a clinical assay for personalized therapeutic susceptibility, HSLCI must have faster turnaround times and demonstrate *in vivo* sensitivity correlations better than current *in vitro* methods, which have not seen wide-scale adoption. With a maximum turnaround time of 40 hours from tumor excision to useable results and a fully automated analysis pipeline, HSLCI reduces both cost and time compared to current gold standard methods. Furthermore, these initial results are promising as they demonstrate the correlation of *in vitro* drug sensitivity profiling with *in vivo* assessments of therapeutic efficacy in pre-clinical PDX breast cancer models.

Future research utilizing HSLCI will include increased throughput and the characterization of resistant subpopulations to assess whether the identified cells by HSLCI are the same cells that proliferate *in vivo*, leading to therapy resistance commonly seen in TNBC. Additionally, HSLCI will also be used to assess drug sensitivity in biopsies from TNBC and other human solid tumors.

### 3.7 Methods

**PDX Mouse Models:** Three triple negative PDX lines, HCI01, HCI09, and UCD52 were obtained from the Huntsman Cancer Institute (HCI) and University of Colorado Denver (UCD) by the Harrell Lab. Cells were resuspended in Matrigel (Corning) and injected into the fourth mammary fat pads of non-obese diabetic severe combined immunodeficient gamma (NSG) mice.

**Preparation of tumor suspension:** As described in Turner et al.[53] and DeRose et al.[50], PDX tumors were excised from the mammary fat pads of NSG mice once they had reached approximately 10mm x 10mm in size. Untreated tumors were digested with a solution of DMEM/F12, 5% fetal bovine serum (FBS), 300 U/ml Collagenase (Sigma), and 100 U/ml hyaluronidase (Sigma). Digested tissue was resuspended in NH<sub>4</sub>Cl, and trypsinized to generate single cell suspensions by the Harrell Lab.

**HSLCI operation:** Cells were plated on 24-well glass bottom plates at  $5 \times 10^4$  cells per well in M87 medium[50] and dosed with pharmaceutical grade carboplatin, obtained from VCU Dalton Oncology Clinic, ranging from 0 to 1 mM. Plates were incubated for 24 hours and then imaged by the HSLCI for 12 hours.

To account for the potential noise introduced by drifting cells and cell debris that could artificially impact measured growth rates of stable cells, data was quality filtered such that only biomass tracks (mass vs. time) exhibiting linear fit standard errors of less than 0.002 normalized mass units per hour and a total mass of greater than 300 pg but less than 3000 pg were included. These error bounds ensure our confidence in the hourly mass accumulation rates is +/- 0.2% and that only true physiologic cell growth is measured. The minimum mass filter ensures that our data only include individual cells or two-three cell clusters, and not cell debris.

**In vivo mouse studies:** The Harrell Lab generated mammary tumors by injecting 500,000 cells from HCI01, HCI09 or UCD52 single cell suspensions into the abdominal mammary gland in 50% Matrigel. After ~3 weeks, when tumors were in log-phase growth (30-60mm<sup>2</sup>), a single intraperitoneal injection of vehicle (normal saline) or carboplatin (40 mg/kg) was administered. Tumor sizes were recorded for an additional 3 weeks.

## 4 Chapter 4: Technological Improvements

The original HSLCI setup not only provided a step change improvement of throughput for single cell biomass measurement (**Section 2.1**), but also the basis for further throughput increases without complete system redesign [24]. The camera only collected images at 4 fps below a theoretical maximum of 32 fps, while the stage only moved at 2mm/s below a maximum of 20 mm/s.

The need for technological improvements was driven by two goals: first screening cells from just a fine needle biopsy (FNB), and second isolating resistant cells for further examination. The number of cells from a FNB would be many less than the digestion of a whole tumor. Instead of millions of cells, our group expected to have thousands to low tens of thousands. This requires imaging as much of the well as possible to capture the growth rates of the highest percentage of cells present as possible.

When isolating resistant cells, the cells of interest are rare. Their rarity necessitates not only increased imaging throughput, but also requires truly real-time processing with the increased imaging throughput.

These goals drove multiple upgrades which are elaborated below.

### 4.1 Image collection upgrades

The first and most simple upgrade was at 40x magnification which was used in the PDX studies. The distance between each image was greater than the length in the y-direction of a single image so that an extra image could be taken each time without overlap, taking 420 (8fps) instead of the 210 images (4fps) each time the stage is moved 100 mm in the y direction (**Figure 5**).

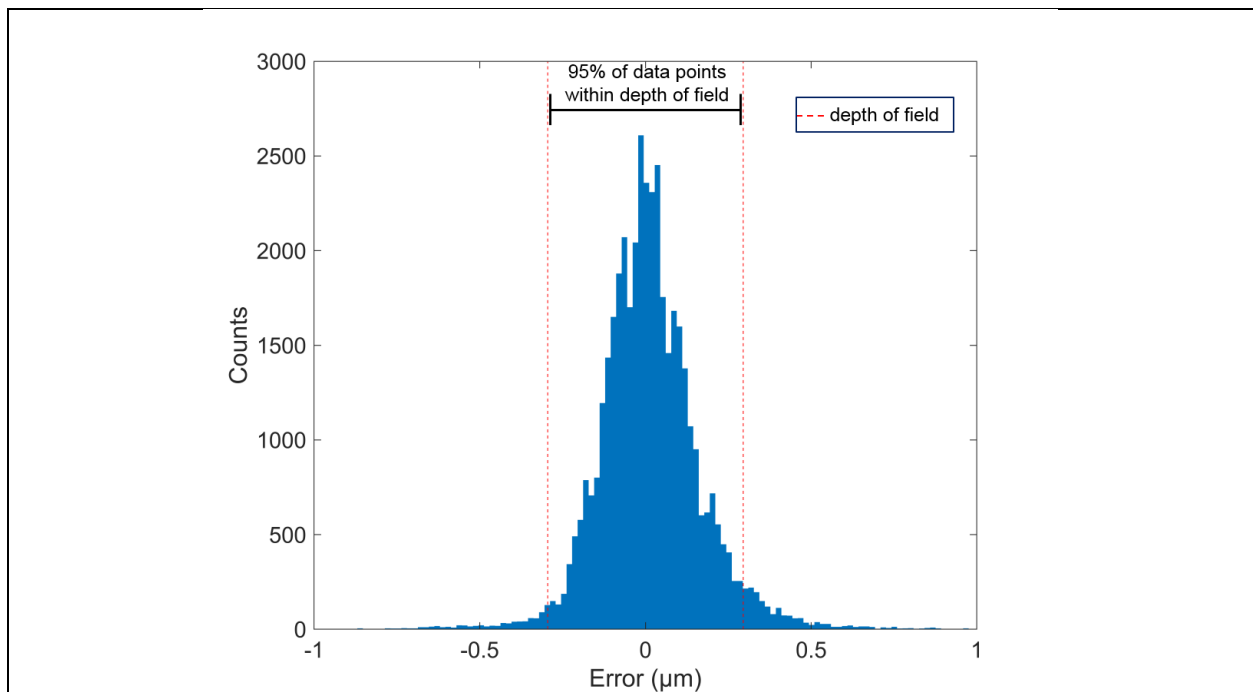


**Figure 13: Objective remains within depth of field >95% of the time while scanning.**

With new hardware upgrades, it was important to ensure the objective (Nikon 40x Plan Flour.) remained within its depth of field while scanning. PID recorded Output, Error, and time elapsed every five milliseconds for 20 loops. Data was then filtered to only include time points where the images were taken. 95% of data points collected remained with the depth field (0.59µm) of focus.

To move the stage faster while maintaining focus the bandwidth of the autofocus feedback loop was increased by upgrading the microcontroller to operate at >1 kHz. At the operating depth of field (0.5 µm; Nikon 40x air objective), testing demonstrated the PID loop kept the microscope within +/- 0.295 µm of the commanded focus position 95% of the time (**Figure 13**).

The system could now move at 8mm/s instead of 2 mm/s which permits maximization of the camera's framerate (32 fps). A new problem arose as the files (each subcolumn, **Figure 5**) were now 420 images instead of 210 images. Due to the increased size, each ".mj2" file took around ~40 seconds to save instead of ~5 seconds. The details of this are discussed in in **Appendix 9.1**. This extra saving time removed any gains from moving faster.

To improve this, saving was then changed so that images are saved as a binary file, the simplest and quickest format to save. Next instead of saving at the end of each loop, the previously collected subcolumn (420 images) is saved from memory while the next subcolumn (420 images) is being collected. With saving times now ~12.5 seconds, the same speed as collection, the system operated close to its theoretical maximum.

These improvements vastly expanded the data footprint. One experiment, the data collected in 12 hours, is now ~3.2 terabytes. Previously, less than 450 gigabytes were collected per experiment. This order of magnitude change required larger hard drives and unlimited back up storage. Additionally, using our previous setup for processing data, a single experiment could take a week or more to process.

This burden of processing and the need to process in real-time for cell isolation experiments drove improvements in image processing.

#### *4.2 Image processing upgrades*

As referenced in **Section 2.1**, analyzing raw interferograms consists of both an unwrapping step and a processing (flattening and segmenting) step. In the original setup these steps are done in sequence by column and loop. All images from column A loop  $n$  on a plate (6-8 subcolumns per column) are unwrapped one by one by the manufacturer's software on one CPU, then all those images are processed in parallel. This made the unwrapping step a major bottleneck.

Two improvements provided by the camera manufacturer made this step faster. First, they developed a new GPU based unwrapping software package which took 85ms per image instead of ~500ms. Second, this software could now take a simple array as an input image instead of as a tiff file, saving an additional ~17ms.

Next the software was redesigned so that processing of the previous set images could occur during the unwrapping of the current images and all this could happen in real-time as images are collected (**Figure 14**). The entire process is run by two computers. The "Control" computer which runs the HSLCI instrument—sending signals to start collecting images and move the stage, and the "Processing" computer which unwraps, flattens and segments the data. The "Control" computer runs the machine through script\_LoopTest where the number of loops and which columns are being imaged is established and then calls Script\_TrigMoveCellIsolation to collect each column of images.

When performing real-time processing at 40x, the bottleneck remains the processing. Eight subcolumns can be processed in <10 minutes. For comparison, 32 subcolumns can be imaged in 10 minutes. For experiments that don't require real-time processing, all 32 subcolumns can be imaged and then processed later.

For experiments that require real-time processing, a six-well plate is used (two columns: A and B). When resistant cells need to be isolated, the column "A", in which the treated cells of interest are, is processed in real-time. As this processing occurs, the control column ("B") can be imaged and analyzed later.

Processing the data while images are still being collected requires constant communication between the processing and control computers to prevent delays in either processing data or data collection. As images are being collected by the "Control" computer, in the background files that are already collected are shuttled to the "Processing" computer for processing.

Just as the “Control” computer updates the “Processing” computer on its data collection by moving files over, the “Processing” computer notifies the “Control” computer when a loop has finished processing. With that signal, the “Control” computer starts collecting another loop of images. This communication ensures that the “Control” computer does not get ahead of the “Processing” computer. The details of this communication are discussed further in **Appendix 9.1** and **Figure 14**.

These processing changes enabled a doubling (4->8 sub columns) of the amount of the data that could be processed within 10 minutes. Continued improvements will come from parallelizing the unwrapping through multiple GPUs, and more workers to parallelize the processing.

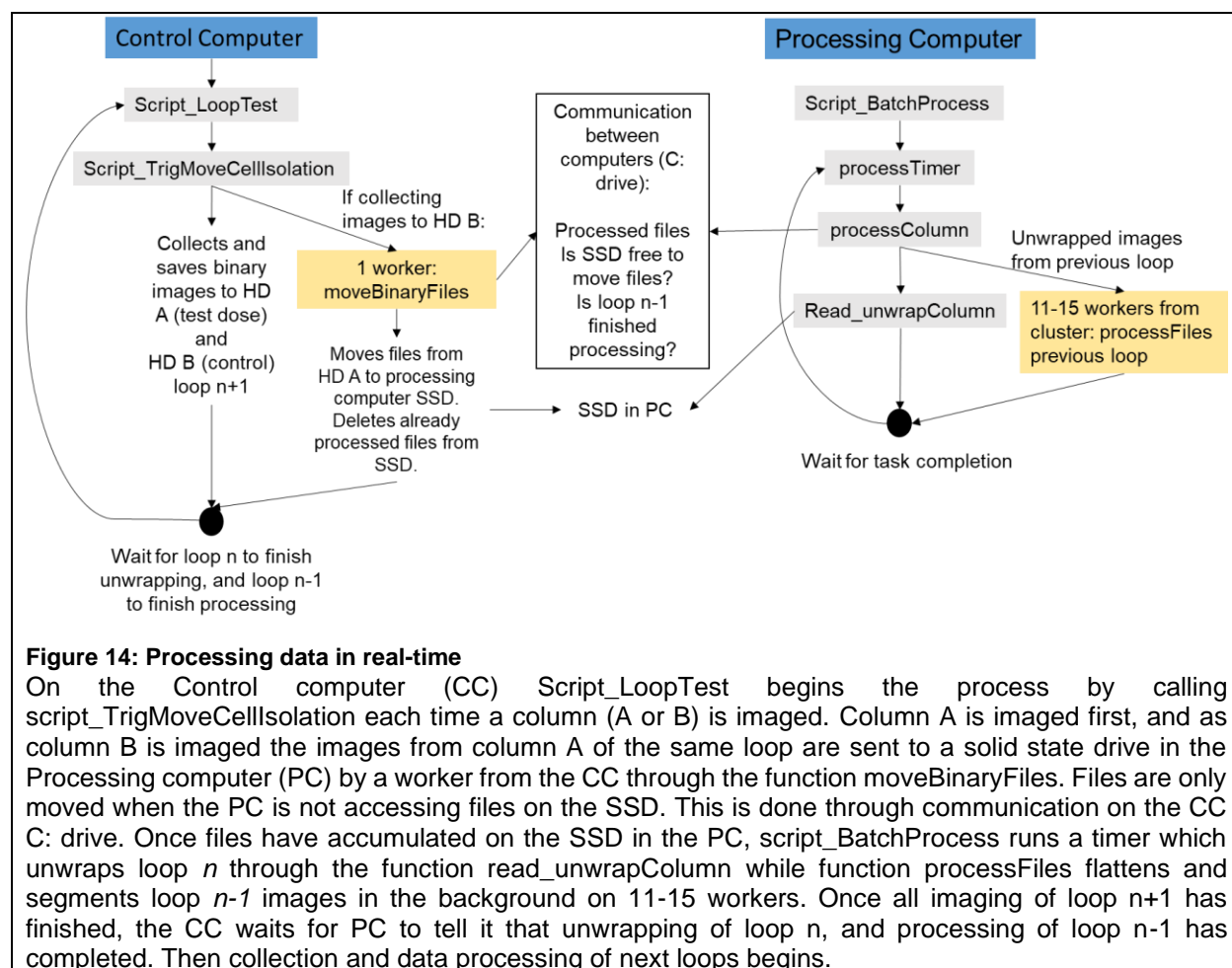


**Figure 14: Processing data in real-time**

On the Control computer (CC) `Script_LoopTest` begins the process by calling `script_TrigMoveCellIsolation` each time a column (A or B) is imaged. Column A is imaged first, and as column B is imaged the images from column A of the same loop are sent to a solid state drive in the Processing computer (PC) by a worker from the CC through the function `moveBinaryFiles`. Files are only moved when the PC is not accessing files on the SSD. This is done through communication on the CC C: drive. Once files have accumulated on the SSD in the PC, `script_BatchProcess` runs a timer which unwraps loop  $n$  through the function `read_unwrapColumn` while function `processFiles` flattens and segments loop  $n-1$  images in the background on 11-15 workers. Once all imaging of loop  $n+1$  has finished, the CC waits for PC to tell it that unwrapping of loop  $n$ , and processing of loop  $n-1$  has completed. Then collection and data processing of next loops begins.

## 5 Chapter 5: Application of upgrades: fine needle biopsy and drug testing on PDX models

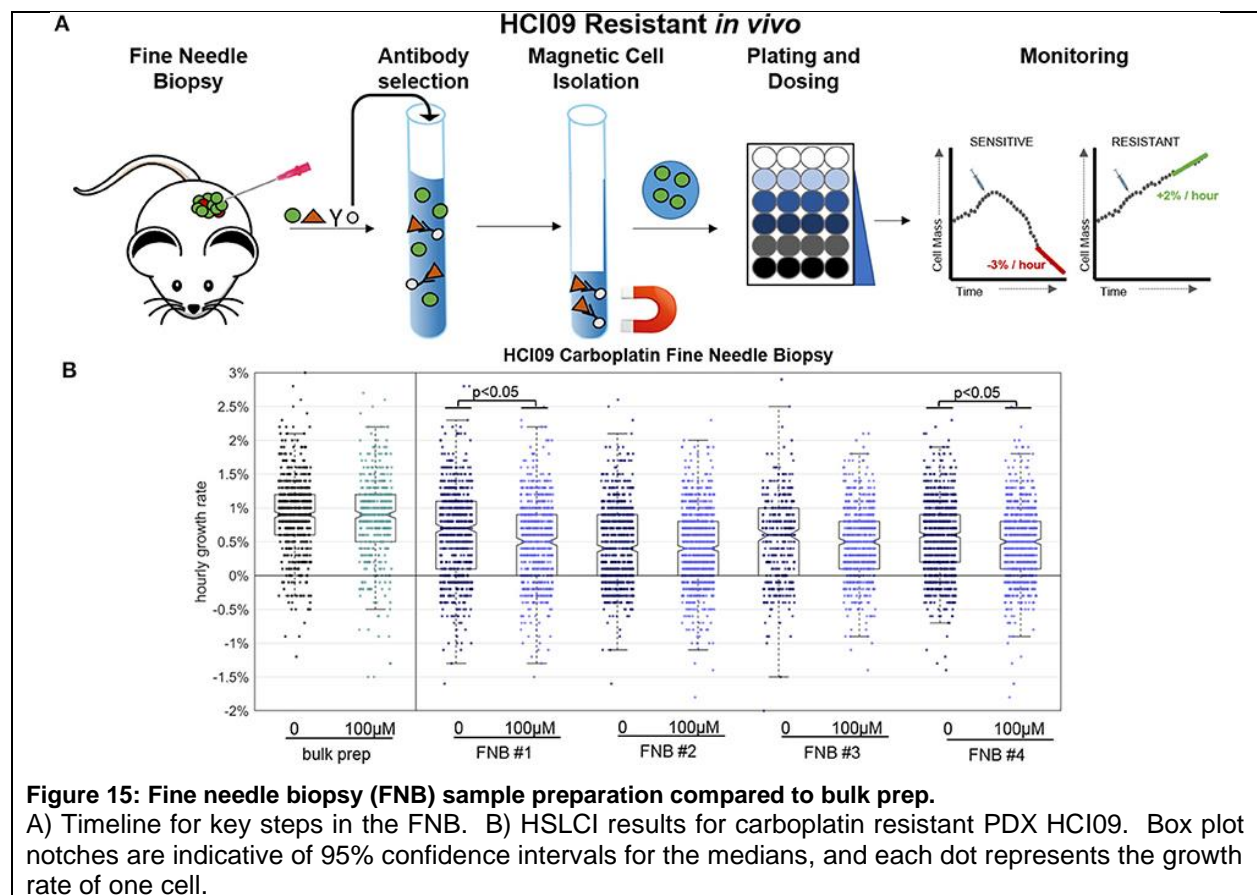
### 5.1 Screening from a fine needle biopsy

Utilizing this higher throughput setup, our group tested the feasibility of acquiring samples through Fine Needle Biopsy (FNB). Prior HSLCI PDX experiments employed bulk excision and enzymatic digestions of murine tumors, resulting in the acquisition of millions of cells [55]. This approach is not feasible in the clinic where procedures need to be minimally invasive for the patients and samples are often divided for multiple analyses, including sequencing and histology. Fine needle biopsy (FNB) is a frequently utilized procedure which provides minimally invasive access to patient tissue using small needles. Additionally, if HSLCI can be used with FNB then it can be used with a larger core sample which is more commonly taken as cores preserve the histology of the tumor. A key question to be resolved in use of FNB with HSLCI is whether or

not the process is so perturbative to the cells' physiologic state that it masks the effects of the drug under study.

To address this question, we developed a simple needle biopsy protocol and compared the results obtained with it to those obtained using a bulk tumor extraction. (**Figure 15**). We tested this protocol using PDX model HCl09, previously shown to be resistant to carboplatin at the therapeutically relevant dose of 100  $\mu\text{M}$  *in vivo* [55]. HCl09 tumors were biopsied with a 22-gauge needle, yielding between 10,000-40,000 viable cells. Debris and dead cells were removed using the Easy Sep  $\text{\textcircled{R}}$  Dead Cell removal kit, which selects for inner leaflet phospholipid Annexin V [56]. The remaining viable cells were then directly plated into standard-footprint 24-well plates, treated with high dose carboplatin (100  $\mu\text{M}$ ), and imaged 24-36 hours after drug administration. For comparison, a standard bulk enzymatic digestion was performed in parallel.

Four independent fine-needle biopsies were performed, labeled as FNB #1 etc. in **Figure 15**. Between 700-1500 cells were isolated and monitored from each biopsy. We found that the negative purification process was absolutely required due to the relatively large fraction of debris present in the FNB as compared to the bulk sample prep, which could be used without this step.



Compared to the bulk prep, both the treated and untreated FNB samples displayed slightly lower median hourly mass accumulation rates, down  $\sim 0.3\%$ , from  $\sim 0.9\%$  per hour in the bulk prep to  $\sim 0.6\%$  per hour in the FNB prep. FNB and bulk prep samples showed a comparable spread of single cell growth rates about the median. The four FNB replicates behaved similarly to one another, with minor differences between replicates in line with our previous PDX results [55]. Two of the four carboplatin treated cases showed a slight ( $\sim 0.2\%$ ) but statistically meaningful median reduction in mass accumulation rate, again within the previously observed range for PDX bulk prep replicates

The isolation process results in a slight reduction in median population mass accumulation rates relative to the bulk prep approach ( $< 0.3\%$  suppression), but this effect is small enough that it does not mask

carboplatin resistance in this particular PDX, nor does it appear to substantially alter the intra-sample growth rate heterogeneity. The mass accumulation suppression induced by FNB could become more meaningful in cases where the untreated samples have naturally low mass accumulation rates and is clearly an issue requiring further study. However, our initial experiments support the viability of FNB as a route to obtaining HSLCI-measurable samples from human patients.

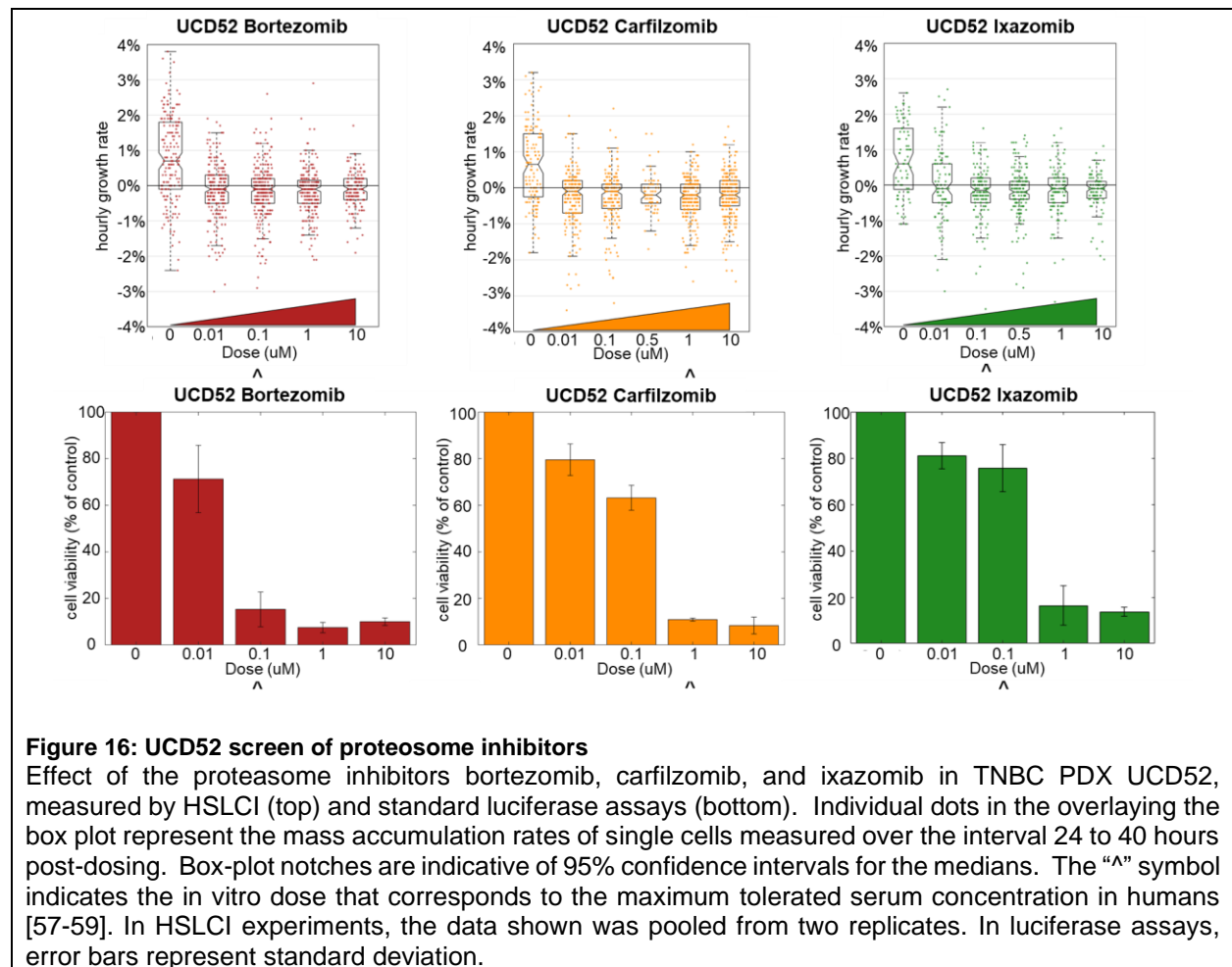
### 5.2 Screening more potentially HSLCI challenging drugs in a shorter time

Throughput upgrades also enable the screening of more drugs in faster time period than our previous studies with PDX models. To begin to define the limits of HSLCI, two classes of drugs that pose potential problems for HSLCI and are relevant in the development of new therapies for TNBC were chosen.

Proteasome inhibitors inhibit the degradation of proteins and directly interfere in mass regulation potentially resulting in an exaggerated effect. CDK 4/6 inhibitors present a challenge by their cell-cycle specific nature. An advantage of HSLCI over other *ex-vivo* methods is the fast turnaround time with screens performed at 24 hours instead of 72 hours since mass loss is the leading edge of cell death. But with cell cycle specific drugs, more time may be required to expose the *ex-vivo* cells as these cells need to progress through the cell cycle. Additionally, eventually most *ex vivo* cells stop growing all together.

Together these two drug classes can provide new insights on the use of HSLCI in as predictor of treatment success *ex vivo*.

#### Proteasome inhibitors



Proteasome inhibitors (PIs) target the process of protein degradation via the ubiquitin-proteasome system. Degradation of proteins through proteasome activity is essential for the maintenance of cell homeostasis. Blocking the activity of the proteasome leads to the accumulation of toxic poly-ubiquitinated proteins within the cell. This accumulation is more pronounced in cancer cells given their higher rate of proliferation and subsequently increased rate of protein synthesis [60]. PIs have become very successful in treating hematologic malignancies, and are being investigated for use in solid cancers, including TNBC.

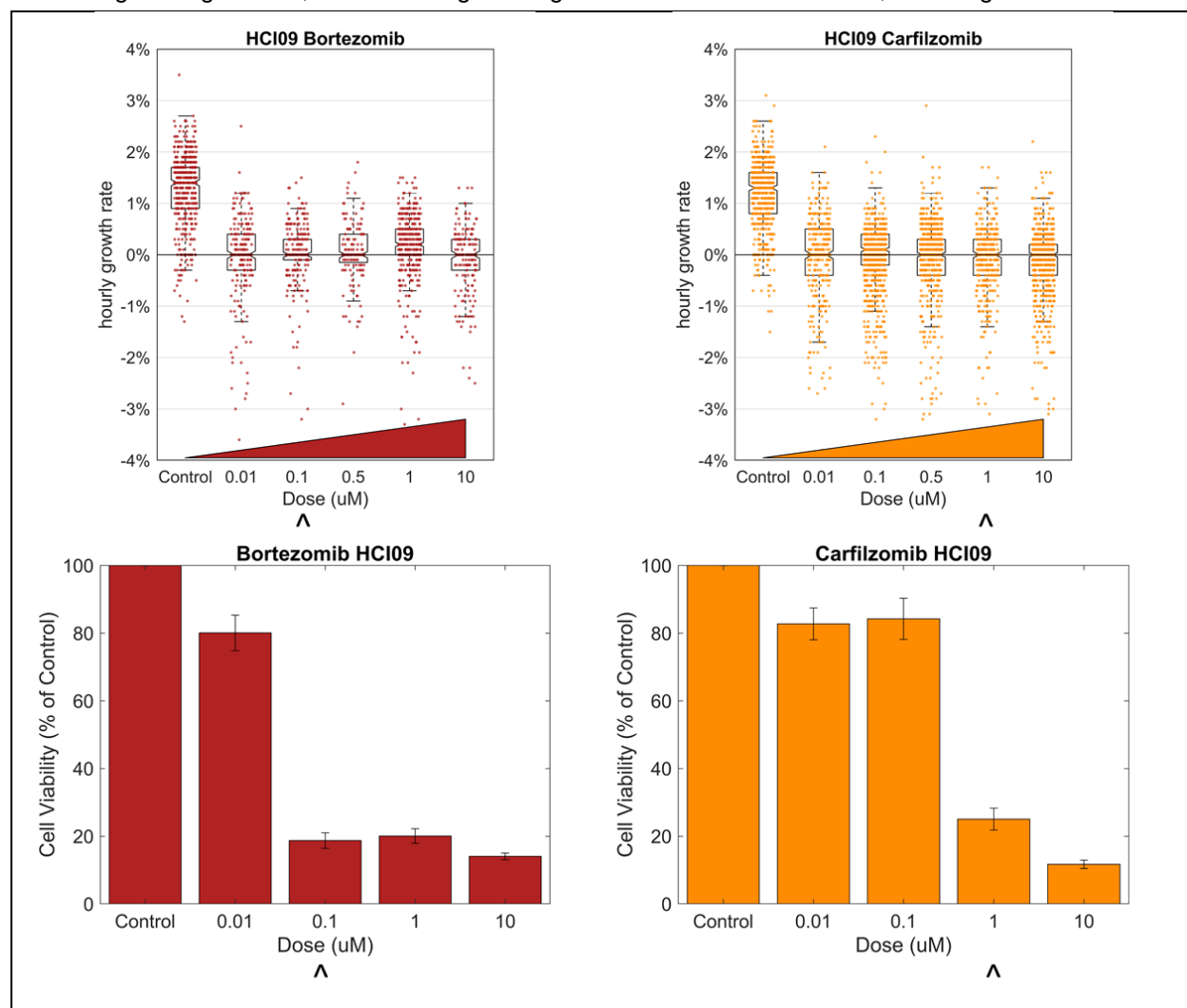


**Figure 17: HCl09 screen of proteasome inhibitors**

Effect of the proteasome inhibitors bortezomib and carfilzomib in TNBC PDX HCl09, measured by HSLCI (top) and standard luciferase assays (bottom). Individual dots in the overlaying the box plot represent the mass accumulation rates of single cells measured over the interval 24 to 40 hours post-dosing. Box-plot notches are indicative of 95% confidence intervals for the medians. The “A” symbol indicates the in vitro dose that corresponds to the maximum tolerated serum concentration in humans [57, 58]. In HSLCI experiments, the data shown was pooled from two replicates. In luciferase assays, error bars represent standard deviation.

Results from experiments on TNBC cell lines and xenograft models have shown that a subpopulation of cells usually survive after treatment with PIs [61]. This has been attributed to the ability of the resistant cells’ proteasomes to utilize alternative enzymatic sites not blocked by the inhibitor molecule. [61]. These findings provide a rationale for screening with a method like HSLCI that can resolve intra-tumor heterogeneity to



better identify risks of failure due to minority resistant populations. Furthermore, since proteasome inhibitors directly interfere with the protein synthesis functions of the cell, one would expect that mass accumulation would serve as a good reporter for response in this therapeutic class.

We used HSLCI to measure the response of two TNBC PDX tumors to the FDA-approved PI bortezomib, a drug currently used to treat multiple myeloma and certain lymphomas, and the same class of drug that is currently being tested in TNBC (ClinicalTrials.gov Identifier: NCT02993094). Additionally, we screened with next generation PIs carfilzomib and ixazomib which are designed to be less toxic. Tumors were excised from mice and enzymatically digested to single-cell suspensions following previously-described protocols [50, 55]. Cells were then treated for 24 hours and then monitored by HSLCI for the following 16 hours (24-40 hours after treatment). Each HSLCI assay included parallel measurements of cells exposed to a log-scale dose range of proteasome inhibitors (**Figure 16 & Figure 17**). For comparison, we also conducted standard luciferase viability assays under the same conditions. These assays differ from HSLCI in that rather than measuring cell-by-cell kinetic responses, they quantify average ATP content of the sample at a fixed time point (usually 72 hours after dosing).

Bortezomib, carfilzomib, and ixazomib were all effective in reducing the mass accumulation rates of both PDX tumors, even at the lowest dose of 10 nM from ~1% to ~0%. In previous studies, a median growth rate of 0% at a dose equivalent to the highest concentration seen in patients reduced tumor burden in mice [55]. But more studies are required to determine the exact level of mass accumulation reduction that will correlate in patients. The data in **Figure 16 & Figure 17** is pooled from two replicates. For the individual replicates, the median growth rates for each condition were within 0.1% of each other with p values > 0.11 in both PDX models, demonstrating reproducibility of these HSLCI screens. Despite the drastic decrease in median growth, at all doses we observed many individual cells that vigorously accumulated mass during the observation period, indicating little or no drug response. This included doses well above the maximum tolerated serum concentration in patients (0.1  $\mu\text{M}$ ). The mass versus time behaviour for one such 'resistant' cell from a UCD52 PDX is shown in **Figure 18**. As discussed previously, it is possible that these 'resistant' cells are effectively utilizing non-targeted proteasome sites [61]. We note that the actual fraction of drug resistant cells is likely smaller than measured, as many drug responsive cells have died and become debris after 24 hours.

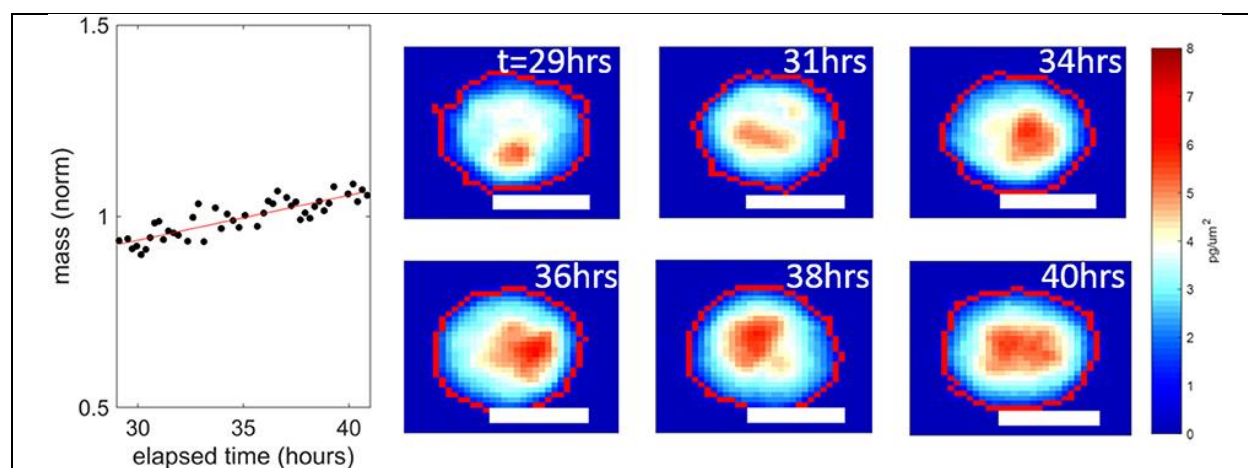


**Figure 18** An example UCD52 cell resistant to 1  $\mu\text{M}$  bortezomib.

This cell is from the data set presented in **Figure 16**. This cell continued accumulating mass a  $1.2 \pm 0.1\%$  per hour over the interval 30–40 h post dosing. The white scale bars are all 10  $\mu\text{m}$ .

In concordance with the HSLCI results, luciferase assays found significant decreases in the median sample viability due to bortezomib treatment for both PDXs at concentrations of 0.1  $\mu\text{M}$  and above and higher doses for carfilzomib and ixazomib (**Figure 16 & Figure 17**). The luciferase assay indicated a less dramatic response for both PDXs at low drug concentrations (0.01  $\mu\text{M}$ ) than did the mass accumulation assay. Our

interpretation of these results is that at the 0.01 $\mu$ M concentration, the PIs effectively inhibits biomass synthesis, which is primarily due to protein production. However, PIs may only modestly impact cell viability as measured by ATP production at 72 hours. The clinical significance of this difference could be resolved by comparison to *in vivo* anti-tumor response at the same dose. *In vivo* studies of PIs performed by the Harrell lab resulted in too much toxicity and had to be discontinued possibly indicating HSLCI may better show this toxicity. This issue remains unresolved.

Unlike past experiments, instead of screening just one drug (carboplatin) on a plate, increased throughput enabled the screening of up to three at a time. Again, showcasing the usefulness of the new throughput.

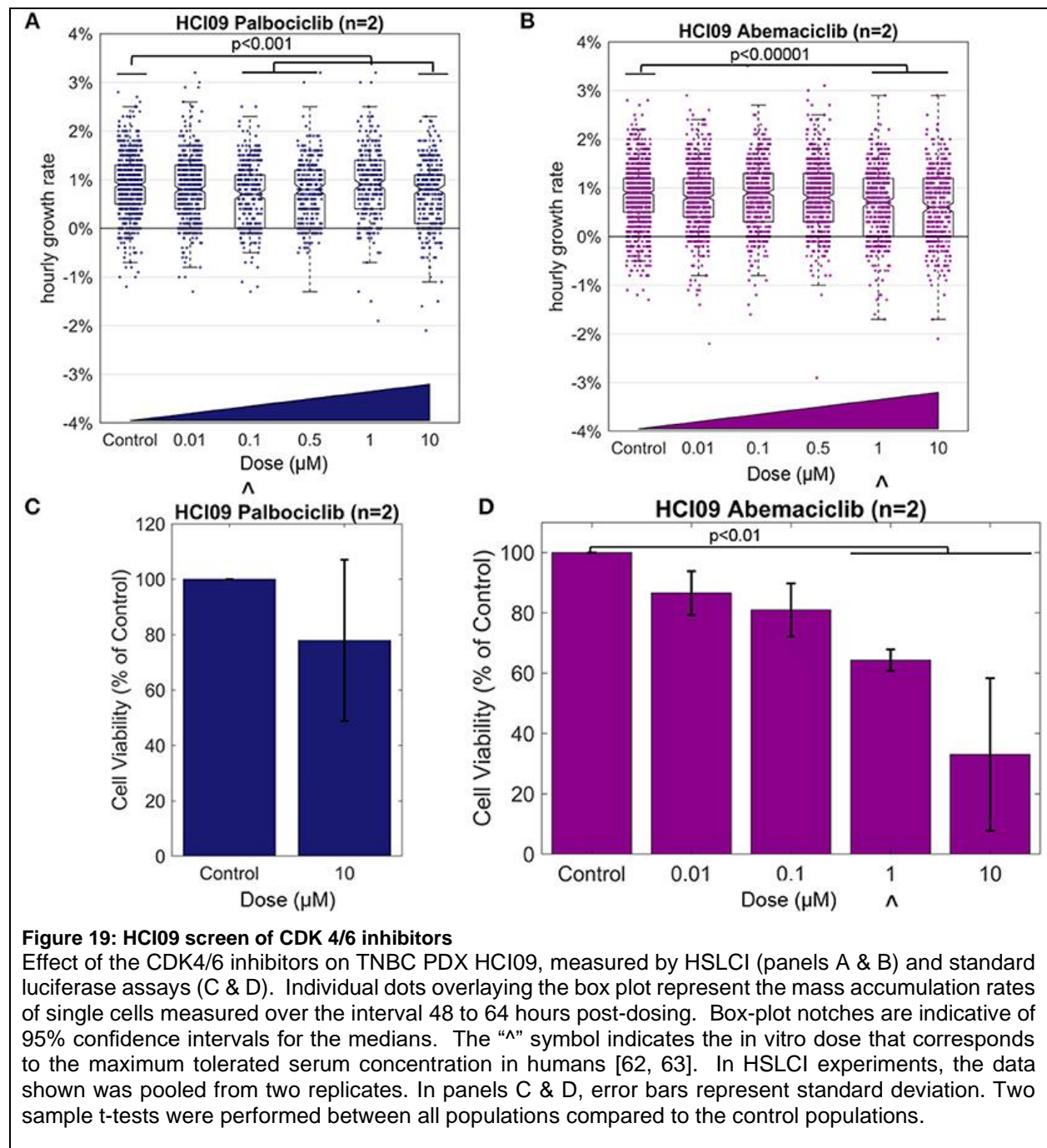


**Figure 19: HCl09 screen of CDK 4/6 inhibitors**

Effect of the CDK4/6 inhibitors on TNBC PDX HCl09, measured by HSLCI (panels A & B) and standard luciferase assays (C & D). Individual dots overlaying the box plot represent the mass accumulation rates of single cells measured over the interval 48 to 64 hours post-dosing. Box-plot notches are indicative of 95% confidence intervals for the medians. The " $\wedge$ " symbol indicates the *in vitro* dose that corresponds to the maximum tolerated serum concentration in humans [62, 63]. In HSLCI experiments, the data shown was pooled from two replicates. In panels C & D, error bars represent standard deviation. Two sample t-tests were performed between all populations compared to the control populations.

As tumor growth can be variable from mouse to mouse and the need for a large number of cells to re-seed tumors in the next generation of mice, the number of doses tested in the luciferase assay was limited by the amount of material available at the time of testing.

*CDK 4/6 Inhibitors*

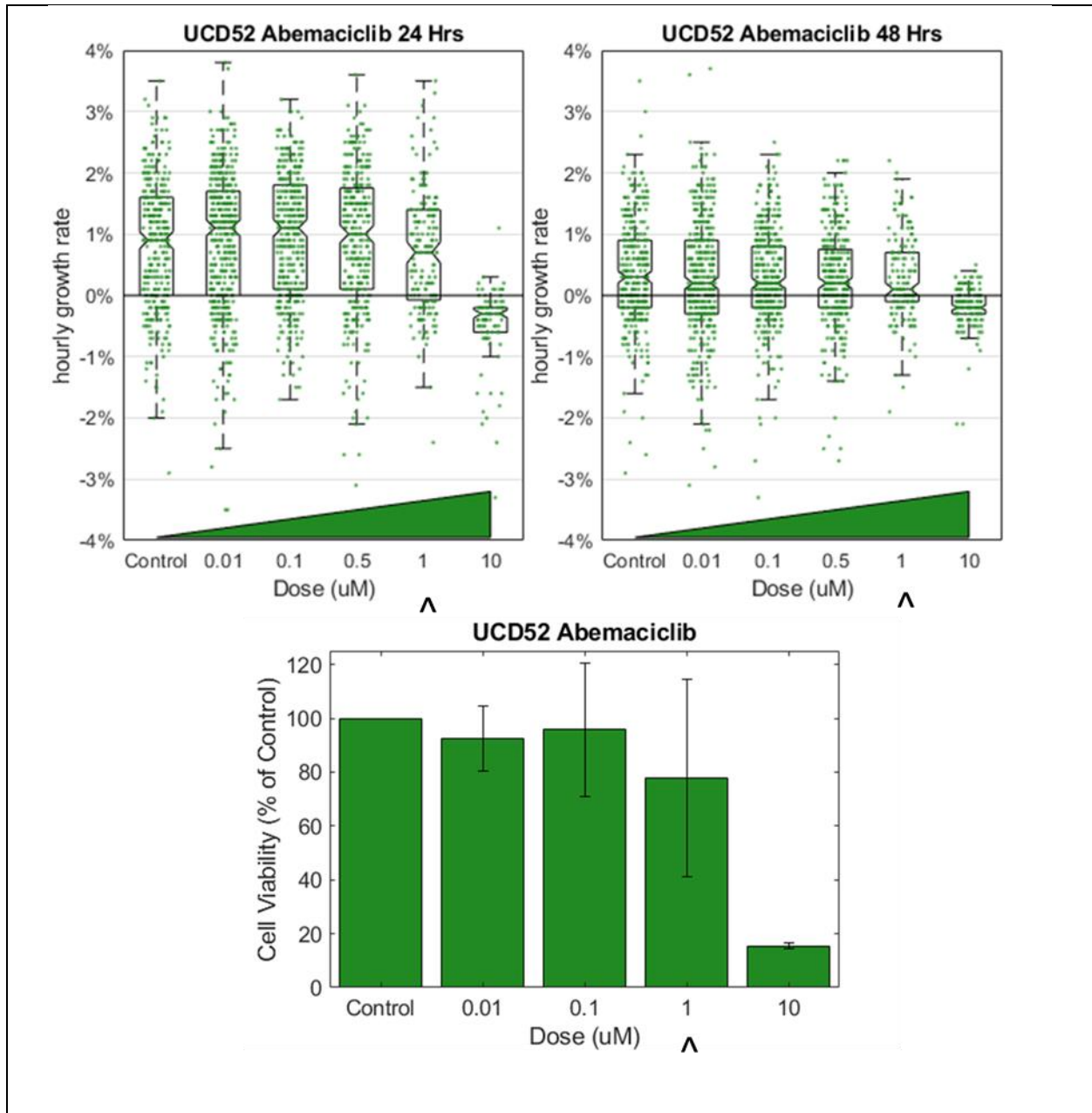


**Figure 20: UCD52 screen of CDK 4/6 inhibitor Abemaciclib, 24 vs 48 hr comparison**

UCD52 TNBC PDX cells were plated and dosed with abemaciclib and then monitored by HSLCI after 24 and 48 hours (top) and measured by luciferase activity after 72 hours (bottom). Individual dots overlaying the box plot represent the mass accumulation rates of single cells measured over the interval 24 to 40 hours or 48 to 64 hours post-dosing. Box-plot notches are indicative of 95% confidence intervals for the medians. The “A” symbol indicates the in vitro dose that corresponds to the maximum tolerated serum concentration in human [62]. In the luciferase assay, the error bars represent standard deviation.

CDK 4/6 inhibitors block cyclin dependent kinases, which serve to progress cells through the cell cycle. They are typically upregulated in cancer cells as part of an increase in proliferation. Several drugs of this class are approved for the treatment of hormone receptor-positive, HER2-negative breast cancer. These drugs are not effective in the common basal type TNBCs, however recent work has shown that luminal androgen receptor-positive TNBCs are sensitive to CDK 4/6 inhibitors [64], and thus they are becoming a more clinically relevant class of drugs for this disease.

Drugs that target the CDK cell cycle control pathway have not been previously tested using HSLCI. Because they specifically target the G1 cell cycle checkpoint, timing of exposure and the window in which the mass accumulation measurement occurs may impact the observed response differently than do drugs such as bortezomib, which are not cell cycle specific.

To gain insight into the timing and magnitude of response measurable with HSLCI, we prepared cells from the luminal androgen receptor-positive PDX HCl09 as described in the Methods (**section 5.3**) and exposed them to CDK4/6 inhibitors palbociclib or abemaciclib at a range of escalating concentrations for 64 hours. We monitored the samples for 16 hours with HSLCI, starting at hour 48 after dosing. (**Figure 19**).

The median hourly mass accumulation rate of cells treated with palbociclib was slightly reduced for three of the four doses above 0.01  $\mu\text{M}$  (median treated growth rate  $\sim 0.8\%$  per hour vs.  $0.9\%$  for control;  $p < 0.001$ ). Though statistically significant, the small magnitude of response and the lack of a clear relationship to escalating doses suggests that palbociclib would not be an effective treatment *in vivo* for this tumor. Past experience with HSLCI dose response curves informs us that a fluctuation of this magnitude ( $\sim 0.1\%$ ) is relatively insignificant and within typical random error (such as tumor sampling heterogeneity or pipetting error) for such samples [49, 55]. This conclusion is supported by the results of a luciferase assay, which showed a similar marginal response at the highest tested dose of 10  $\mu\text{M}$ . However, we note that 10  $\mu\text{M}$  is well above the maximum tolerated serum concentration in humans (0.01  $\mu\text{M}$ ).

In the HSLCI assay, the magnitude of response to abemaciclib was similar to that seen with palbociclib, except that the dose response was more clearly defined. Above 1  $\mu\text{M}$ , the maximum tolerated serum concentration in humans, the reduction in median mass accumulation rate versus control became statistically significant. Similarly, the luciferase assay showed a scaled reduction in viability corresponding to increasing doses which also became significant at 1  $\mu\text{M}$ , but again the small magnitude of response indicates abemaciclib may only be marginally effective *in vivo*. Due to smaller than anticipated tumor size, the number of doses tested in the luciferase assay was limited by the amount of material available at the time.

Screening UCD52 with abemaciclib provided even more insight to cell cycle specificity and *ex vivo* data collection. **Figure 20** shows the same UCD52 cells screened after 24 and 48 hours of drug exposure. The 48 hours screen agrees with a replicate done independently (not shown). After 48 hours, the *ex vivo* untreated UCD52 cells have lost a significant amount of growth from a median of  $\sim 1\%$  to only  $\sim 0.25\%$ . This is not unsurprising as most cells extracted from a tumor stop growing eventually without 3-D organoid culture or special stimulants. Overcoming this limitation, the screen after 24 hours matches the luciferase assay data collected after 72 hours. The metabolism of these PDX cells that the luciferase assay measures may be greatly reduced 72 hours *ex vivo* leading to large amounts of noise. While HSLCI matches gold standard *ex vivo*, further comparison to *in vivo* treatments is necessary.

### 5.3 Methods

#### HSLCI Screens

PDX cells were plated on 24-well glass bottom plates at  $5-7.5 \times 10^4$  cells per well in M87 medium [50]. Cells were treated for 24 or 48 hours depending on whether the drug was cell cycle specific and then monitored for the following 16 hours by HSLCI using a 40x objective (Nikon, NA 0.75).

As in past experiments, data was quality filtered such that only biomass tracks (mass vs. time) exhibiting linear fit standard errors of less than 0.002 normalized mass units per hour and a total mass of greater than 300 pg but less than 3000 pg were included. These error bounds ensure our confidence in the hourly mass accumulation rates is +/- 0.2% and that only true physiologic cell growth is measured. The minimum mass filter ensures that our data only include individual cells or two-three cell clusters, and not cell debris.

### Luciferase Assays

HCI09 and UCD52 cells were plated in M87 medium [50], in triplicate (25,000 cells/100  $\mu$ l per well) in 96-well plates and incubated at 37°C for 3 days with each drug by the Harrell Lab. To assess cell viability over time, D-luciferin (10  $\mu$ l/well) was added and plates were imaged using an In Vivo Imaging System (IVIS) on day 3.

### Fine Needle Biopsy

Tumors were excised and then biopsied with a 22-gauge needle. Debris and dead cells were removed with Easy Sep® Dead Cell Removal kits. Cells were then plated and dosed for 24 hours, and then monitored by HSLCI for 12 hours.

## 6 Chapter 6: Isolation of Cells

The technologic improvements to enable real-time processing discussed in **Chapter 4.2** allow a new type of experiment to be performed with HSLCI. As the cell's biomass growth is identified in real-time, those cells which are drug resistant, continued biomass growth despite drug treatment, could be isolated for analysis.

### 6.1 Addition of micropipette system

While data could now be processed in real-time, it was necessary to build an addition to the system which enabled isolation of cells of interest due to their biomass growth. Various methods exist for single cell isolation including microfluidic channels, acoustic trapping, or fluorescent activated cell sorting, but the most suitable to integration in to the HSLCI system is semi-automated cell picking with a micropipette [65, 66].

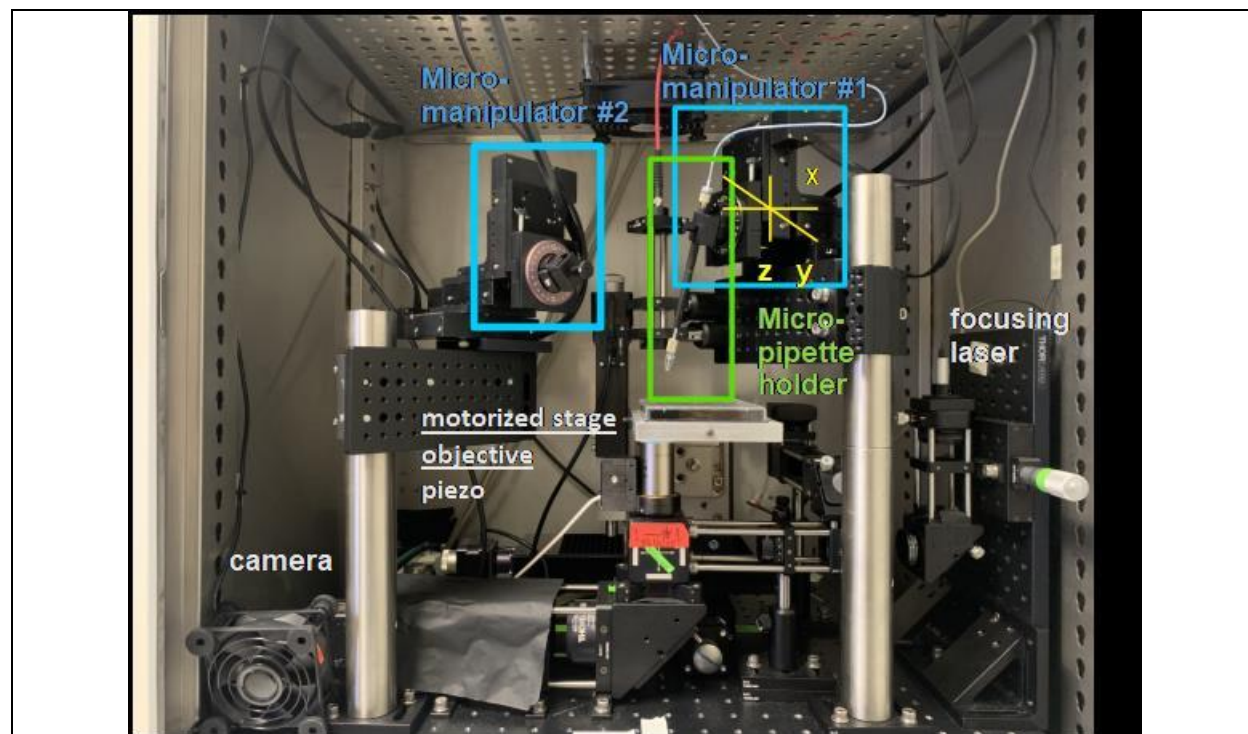
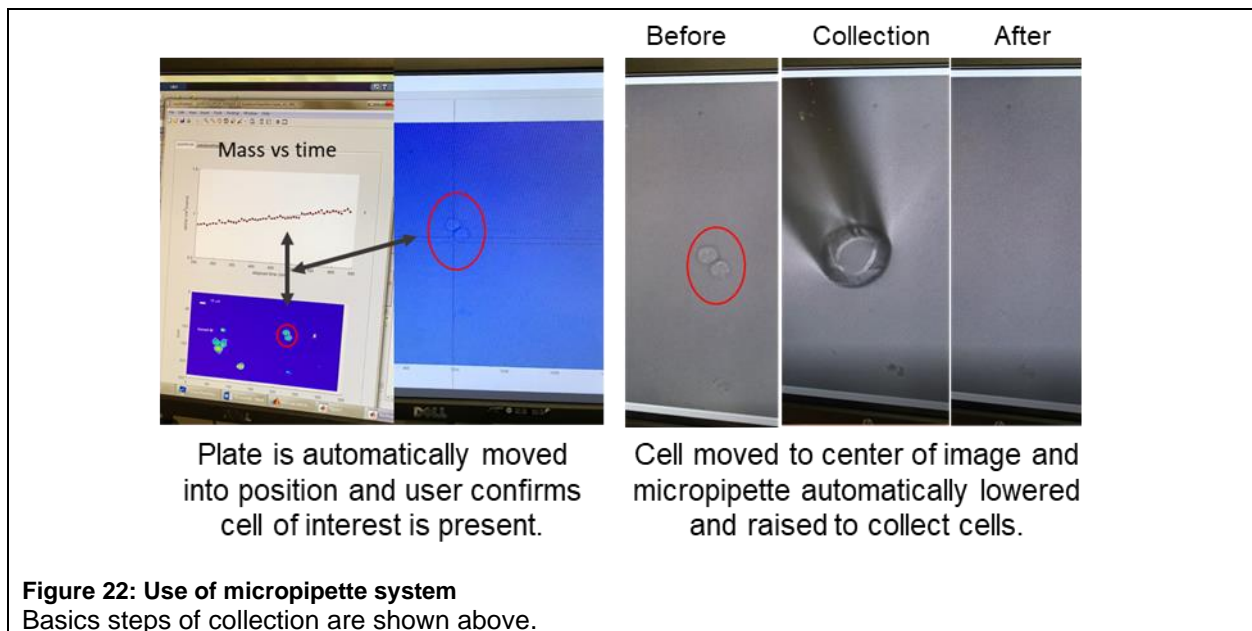


**Figure 21: Additions to HSLCI system for cell isolation**

To isolate cells by micropipette two micromanipulators (blue, Sutter Instruments MPC-200) were added above stage (one in use). With micron precise movement in the x, y, & z directions (yellow) a micropipette inserted into the micropipette holder (green) could be raised and lowered into wells to collect cells with capillary pressure. The micropipette holder is connected to a syringe through thin tubing for ejection of cells into a PCR collection tube at the end of experiments. Objects previously described in **Figure 3** are written in gray for reference.

With the micropipette in place, software additions were required to enable use. After all the data has been processed in real-time (**Chapter 4.2**), the user determines which cells they would like to isolate based on the cell's or cells' growth rate. Typically, the top 1-10% of growing cells are of interest. On the Processing computer, script\_IsolateResistantCells is run to bring up the biomass growth track of an identified cell of interest (**Figure 22**) and the location of cell is sent to the control computer. On the control computer, the "isolate cell" button is selected, and the stage is automatically moved to the location of the cell of interest.

After the user confirms the cell of interest is present, the user selects it on an image, and that cell is moved to the center of image. The micropipette automatically lowers below the media level for 0.4 seconds to pick up the cells with an image taken before and after collection. After the user confirms capture, the processing computer moves on to the next cell of interest. After all cells of interest have been captured, the tip of the micropipette is broken into a PCR tube and the media (~2 uL) is retrieved using a syringe.



This system was then trialed on isolating drug resistant cells from a mixed population of drug sensitive (99%) and drug resistant (1%) cells with the eventual goal of studying drug tolerance after the initial drug exposure.

**6.2 Targeted therapy and the need to study drug tolerance**

Targeted therapies use novel agents that specifically target one or more proteins in a cell and are administered based on the genetic make-up of the patients' cancer. As these drugs are personalized to the patients' specific cancer, they can be very effective and are considerably less toxic to normal cells than are chemotherapies. While targeted therapies continue to change the landscape of cancer therapeutics and lead to tumor shrinkage in many cases, the major drawback is patients' cancers eventually grow back in the presence of the drug, a phenomenon known as "acquired resistance." Unfortunately, this usually occurs

within one year, and afterwards there are limited treatment options [67]. In some cases, secondary mutations that confer resistance to targeted inhibitors can exist-- usually at hard-to detect frequencies-- prior to initiation of treatment, or alternatively, appear *de novo* [68]; similarly, other non-genetic-based resistant mechanisms can also appear *de novo*, in response to the selection pressure of the targeted inhibitor [69].

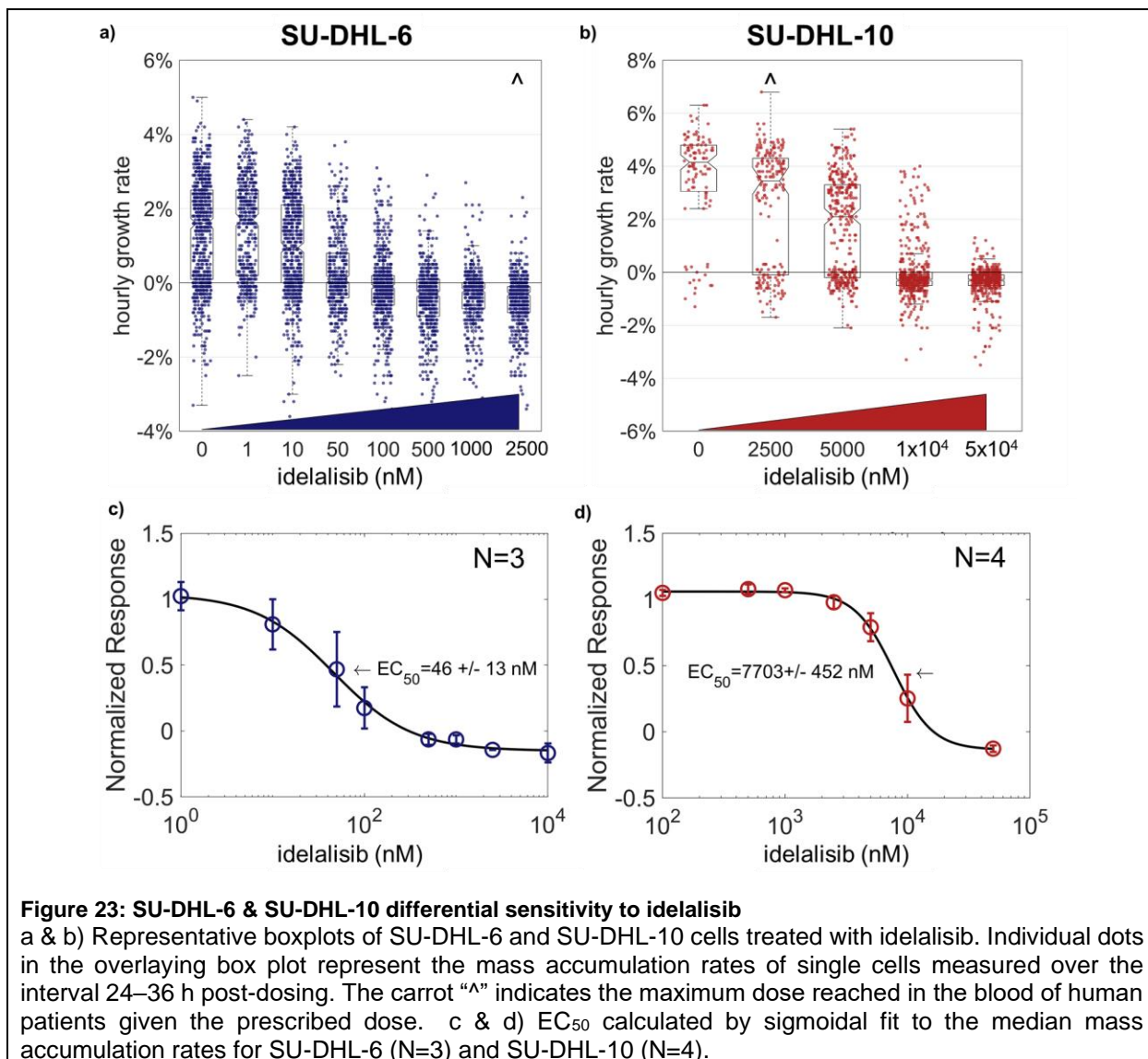
In the case of non-pre-existing resistant clones (whether mutation based or otherwise), it remains largely unknown how some cancer cells survive initial treatment, allowing them to eventually acquire resistance, usually by multiple, heterogeneous mechanisms. An increasingly-recognized reason for treatment failure involves a subpopulation of cells possessing immediate drug tolerance, at least for some period of time [70-72]. These drug-tolerant cells survive long enough during initial treatment to spontaneously acquire genetic or non-genetic changes that confer long-term (stable) resistance. There remains no precise method to study these drug-tolerant subpopulations because transient growth and survival at the single cell level during initial treatment is very difficult to measure.

In this work we overcome this hurdle and quickly identify and isolate rare diffuse large B cell lymphoma (DLBCL) cells tolerant of the targeted therapeutic agent, idelalisib, using a novel single cell biomass tracking approach. Idelalisib is an inhibitor of phosphatidylinositol 3-kinase (PI3K) that is sometimes used for salvage therapy in treatment refractory DLBCL patients to simulate rare drug tolerant cells. We created an *ex vivo*, drug-resistant-clone-containing tumor using a 1:100 mixture of two DLBCL cell lines, SU-DHL-10 and SU-DHL-6 [73], which have differential sensitivity to idelalisib. We then identified idelalisib-tolerant cells in real time by their substantial and distinct biomass growth in the presence of drug using High Speed Live Cell Interferometry (HSLCI), a multi-well biomass accumulation assay [18, 24, 55]. Fast growing cells were isolated via an automated micropipette system and re-cultured to confirm their idelalisib resistance. Both cell lines have IGH-BCL2 (t14:18) fusions. SU-DHL-6 has a breakpoint in the major breakpoint region (MBR). SU-DHL-10 has a different breakpoint, in the intermediate cluster region (ICR), of chromosome 18. This difference in translocation breakpoints between the two cell lines enables the identification of the two lines through PCR [74]. SU-DHL-10 cells were isolated within 40 hours of drug exposure. This quick turnaround enables future quantification of epigenetic and metabolic changes of drug tolerant cells in treatment naïve tumors.

While DLBCL provides a specific scenario in which characterizing drug-resistant subpopulations before relapse becomes clinically relevant, cancer relapse is a problem affecting nearly all cancers and isolating and studying drug-resistant subpopulations at an early stage could inform clinical decision making in nearly all of them.

### 6.3 SU-DHL-10 & SU-DHL-6 differential sensitivity to idelalisib

To measure the sensitivity of both SU-DHL-6 and -10 to idelalisib, cells were dosed at a range of concentrations from 0  $\mu$ M to 50  $\mu$ M for 24 hours, followed by monitoring biomass growth by HSLCI for 12 hours (**Figure 23**). We found that SU-DHL-6 had a half maximal effective concentration ( $EC_{50}$ ) of 46 +/- 13 nM (n= 3), while SU-DHL-10 had an  $EC_{50}$  of 7,703 +/- 452 nM (n = 4). Therefore, SU-DHL-10 requires greater than two orders of magnitude more idelalisib to experience a similar effect on biomass growth as SU-DHL-6. For reference, a patient taking the recommended dose of idelalisib and the dose used in the clinical trial, 150 mg, will have a maximum concentration of idelalisib of approximately 2-3  $\mu$ M in their blood [75]. At 2.5  $\mu$ M, SU-DHL-10 cell growth remains close to untreated cell growth (97.8% +/- 4.9% of the normalized response), while the median growth of SU-DHL-6 cells is negative even at 1  $\mu$ M (p<0.001 vs untreated cells). Of note, while SU-DHL-6 untreated cells appear to have an even spread of hourly growth rates from -2%-5%, SU-DHL-10 untreated or low dosed cells appear to fall into one of two categories: growing at ~4% or dying or dormant at ~0%.



#### 6.4 SU-DHL-10/SU-DHL-6 1:100 idelalisib resistant cell isolation

Individual cultures of SU-DHL-10 and -6 cells were collected and counted, and then mixed at a 1:100 ratio on a six well plate. Cells were then treated with either 0 or 2.5  $\mu$ M of idelalisib, which is a dose commensurate with the highest concentration seen in the blood of patients. After 24 hours the biomass growth of single cells or cell clusters was measured every 8 minutes by HSLCI for the next 12-16 hrs. At the end of the observation period, single fast growing cells or clusters were located and automatically collected into a micropipette (**Supplementary Figure 1**). This process was repeated until the desired number of cells were collected. These isolated cells were then re-cultured for two to three weeks and then re-screened in 2.5  $\mu$ M idelalisib to confirm that they were indeed resistant to the drug.

Three drug resistant cell isolations were performed with a representative example shown in **Figure 24** (see also **Supplementary Figure 2**). The median hourly growth rates of the untreated 1:100 cell mixtures ranged from 1.5% +/- 0.1% to 1.9% +/- 0.1% in the three trials. In contrast, the median hourly growth rates of the cells treated with 2.5  $\mu$ M idelalisib ranged from -0.3% +/- 0.02% to 0% +/- 0.07%, indicating idelalisib had significant growth inhibition effects at 2.5  $\mu$ M on the 1:100 mixture. When evaluated with two sample t-test, the comparison of corresponding treated and untreated population for each trial yields  $p < 0.0001$  for all three trials.



The fastest growing 1% of cells were isolated from each of the treated population, as indicated by the red asterisk “\*”. These cells were then re-cultured for approximately two to three weeks. Median growth rates of untreated populations ranged from 4.0% +/- 0.1% to 4.4 +/- 0.1% while median growth rates of treated populations ranged from 3.8% +/- 0.1% to 4.4 +/- 0.07% in the three trials. When evaluated with two sample t-test, the comparison of corresponding treated and untreated population for each trial yields  $p > 0.30$  for all three trials. The identity of the re-cultured resistant cells as SU-DHL-10 was further confirmed through PCR (**Figure 24d, Supplementary Figure 3**) [74]. These results indicate the successful isolation of the 1% idelalisib tolerant sub-population. As a further control, cultures of media from micropipettes that were exposed in the media but collected no cells resulted in no cell growth. Additionally, collection of approximately 10 random cells in the bottom 95% of growth rates resulted in no cell growth (**Figure 24c, Supplementary Figure 4**).

Future developments of this technique will include adaptation to primary cells extracted from tissue, which typically have a shorter viability window, versus cell lines which grow robustly in culture for extended periods. HSLCI has been used successfully with primary tissue from triple negative breast cancer patient-derived xenografts, including very limited quantity samples obtained from a fine needle biopsy [55, 76]. However, it is likely that additional optimization of media conditions would be needed for some types of primary samples.

Traditional dye exclusion cell viability assays conducted via microscopy at a single point in time could differentiate live cells from apoptotic or necrotic cells for isolation. However, this method would not discriminate slow growing or quiescent cells from vigorously growing cells, as does biomass tracking. Biologically, the cells growing vigorously in the presence of drug are likely to be the most interesting candidates for mechanistic studies. Furthermore, in contrast to the snapshot nature of dye exclusion assays, the kinetics of single cell responses captured by biomass tracking may prove to be particularly informative in fragile primary cultures which remain viable for only short periods after isolation.

In addition to biomass tracking, other single cell analytical methodologies can explore the heterogeneity of the drug response such as fluorescence lifetime assays (FLT) or Raman spectroscopy[77, 78]. While both techniques provide insights into metabolic responses to drugs, they have not been used to isolate low abundance drug-tolerant cells from mixed samples. Higher throughput FLT assays are prone to photo bleaching, can have trouble resolving multi exponential decays, and data processing is not yet real-time[78]. High throughput Raman based methods have only been able to provide a snapshot in time of drug response unlike the time dynamic measurements acquired by HSLCI[79].

The ability to identify and isolate live resistant subpopulations via HSLCI can be a valuable tool for both basic research and clinical decision making in solid and liquid tumors alike. Identification and re-culturing of resistant subpopulations in cell lines or primary samples could facilitate the study of mechanisms of drug-resistance. In the clinical setting, HSLCI could be used to identify and characterize drug resistant clones, before disease relapse becomes evident in the patient.

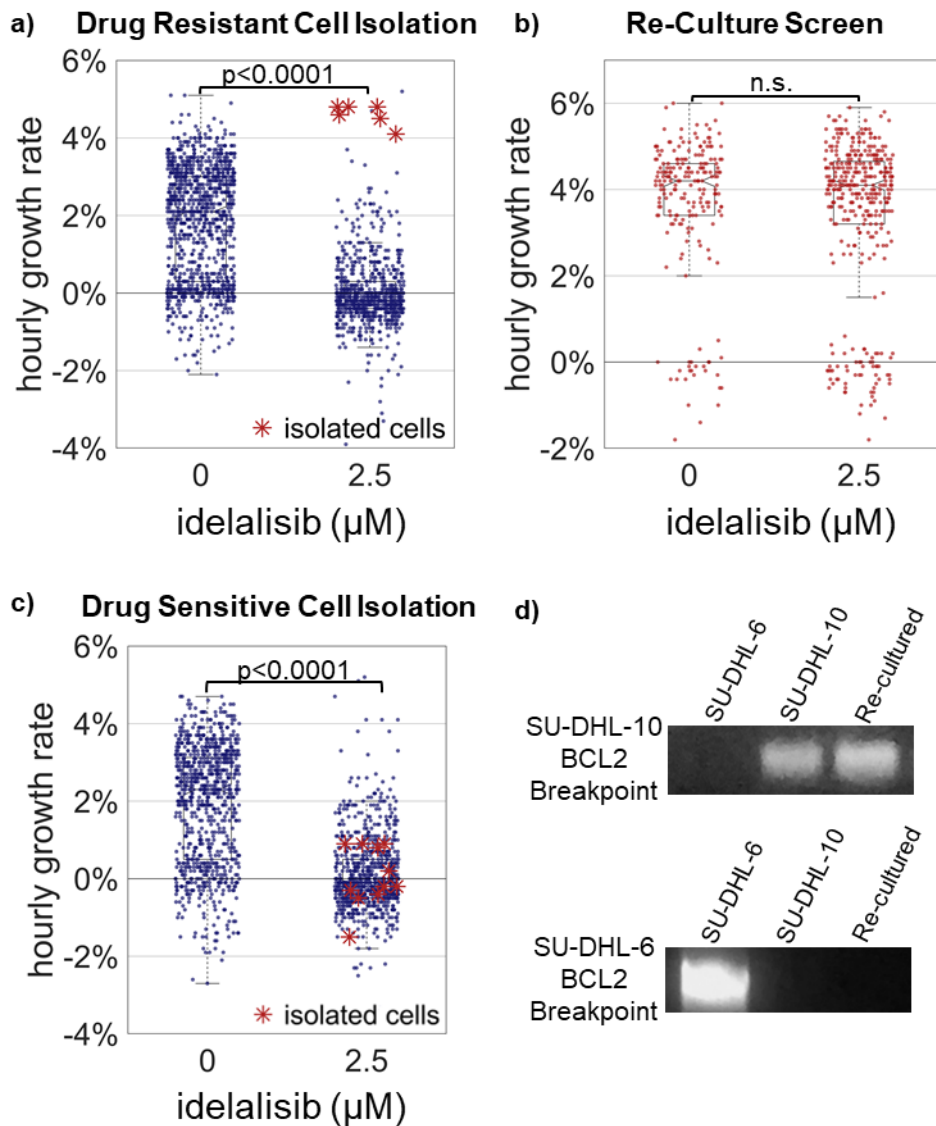


**Figure 24: Isolation and re-culture of idelalisib resistant cells**

a) Representative example (n=3) of the isolation of the top 1% of growing cells from 1:100 SU-DHL-10/SU-DHL-6 mixture. Cells were treated with 2.5  $\mu\text{M}$  idelalisib for 24 hours and mass accumulation rates were measured from 24-40 hours post dosing at which point the top 1% of growing cells were isolated by micropipette. b) Cells isolated in (a) were cultured for 20 days then rescreened at 2.5  $\mu\text{M}$  idelalisib. The median growth rate at 2.5  $\mu\text{M}$  idelalisib increased from -0.2%  $\pm$  0.02% per hour in the isolation to 4.1%  $\pm$  0.12% per hour after re-culture. c). In an experiment identical to (a), cells in the bottom <95<sup>th</sup> percentiles were isolated and cultured, but no growth occurred. d) PCR at the IGH-BCL2 loci for the cell line-specific breakpoints was performed on cells from stock SU-DHL-6 and -10 lines, and re-cultured cells indicating SU-DHL-10 cells were isolated from the 1:100 mixture.

## 6.5 Methods

### Cells and Cell Culture

SU-DHL-6 and -10 cells were obtained from American Type Culture Collection (ATCC) and maintained with RPMI 1640 supplemented with 10% FBS also obtained from ATCC. Cells isolated from HSLCI screenings

were at first maintained in 200  $\mu$ L of RPMI 1640 in a 96-well plate until they had grown out to about 100,000 cells at which point cells were maintained in a 24 well plate, and then finally in T25s.

### HSLCI Screening Experiments

The HSLCI platform is a custom-built inverted optical microscope coupled to an off axis quadriwave lateral shearing interferometric camera (SID4BIO, Phasics, Inc.). Cells are imaged in single, standard-footprint (128  $\times$  85 mm), glass-bottomed, 6 or 24 well plates (Cellvis). Acquired images are processed by a downstream PC using NVIDIA K2000 GPU and a MATLAB pipeline. All of the platform's hardware and software components are available commercially. A 40x objective (Nikon, NA 0.75) was used for all the studies. The imaging platform is installed within a standard cell culture incubator.

Between 50,000-100,000 cells per well were plated in either 24 or 6 well plates. Cells were then treated with the proper doses of idelalisib (ApeXBio). After 24 hours for treatment to take effect, cells were monitored for 12-16 hours.

To ensure the quality of hourly growth rates recorded, data was filtered such that only biomass tracks (mass vs. time) exhibiting linear fit standard errors less than 0.002 normalized mass units per hour were included. This excludes tracks where noise is introduced by cell debris or drifting interrupts the tracks of otherwise stable cells. Only cells greater than 300 pg were included, as objects smaller than that never grew and appeared to be just debris.

### HSLCI Isolation Experiments

100,000 cells per well were plated in 6 well plates. Cells were treated with either 0 or 2.5  $\mu$ M of idelalisib. After 24 hours, cells were monitored for 12-16 hours. Data from 2.5  $\mu$ M condition was processed in real-time, and the 0  $\mu$ M data processed after the experiment. Images are then tracked frame to frame and hourly growth rates determined. Cells were then isolated with a micropipette (0.5 mm, borosilicate glass, Sutter Instruments) that was pulled using P-2000 micropipette puller (Heat=290, Pull=25, Delay=150, Velocity=20, Sutter Instruments).

The locations of cells with growth rates in top ~1% are then sent from a processing computer to a control computer. HSLCI machine then automatically goes to each location, the user then indicates whether the tracked cell or cell cluster is present and should be isolated. Then the micropipette automatically comes down and retrieves the cell or cell cluster using capillary pressure. The micropipette then goes back above the surface of the media, and machine moves to the next location. After completion of collection, the liquid is deposited into 100  $\mu$ L of RPMI 1640 media for re-culture.

### PCR

PCR was performed on the re-cultured samples from Trials #1, 2, and 3 for detection of distinct breakpoints in BCL2 due IGH-BCL2 fusions in SU-DHL-6 and SU-DHL-10. Primer sequences and genomic coordinates are available in **Supp. Table #1**. Genomic DNA was extracted with Qiagen's MagAttract HMW DNA kit. DNA concentration was then measured with ThermoFisher's Quibit dsDNA HS Assay kit. Next the PCR solution composed of primers identified by Bouamar et al [74] for identifying SU-DHL-6 and SU-DHL-10 cells, millipure water and New England Biotechnologies Long AMP PCR Master Mix, was mixed with the samples. The solution was then heated to 95C for 1 minute and cycled 45 times at 95C for 15 seconds, 57C for 15 seconds and then 60C for 1 minute. 5 $\mu$ L aliquots were run on a 2% agarose gel.

## 7 Chapter 7: Senescence

Biomass is a dynamic biomarker that provides more information on the single cell level than just a binary designation of drug resistance or sensitivity. In fact, biomass growth captures a spectrum of responses. There exist multiple processes through which cells exhibit effects from drugs without succumbing to the drugs. One of these processes is known as senescence and involves large scale changes in biomass distribution.

## 7.1 Introduction

Cellular senescence was first characterized by Leonard Hayflick when he demonstrated that fibroblasts have a finite capacity for replication *in vitro*. He considered it as aging at the cellular level [80]. Since the 1960s, there has been considerable progress in characterizing senescence with new molecular techniques that identify it with specific features [81] such as changes in cell size, activation of the DNA damage repair response [82], enhanced lysosomal biogenesis as measured by increased Senescence-Associated- $\beta$ -galactosidase (SA- $\beta$ -gal) enzyme activity [83], alterations in gene expression [84-86], epigenetic modifications known as Senescence-Associated Heterochromatic Foci (SAHF) [87, 88], and finally secretion of a spectrum of chemokines and cytokines collectively known as Senescence-Associated Secretory Phenotype (SASP) [89, 90].

The primary characteristic of senescence is still considered to be proliferative arrest [91]. This response of proliferative arrest and changes in DNA expression at every level of regulation is not just limited to aging but also the response to various DNA damaging anti-tumor drugs [92]. Permanent proliferative arrest would be a desirable outcome of drug therapy if secondary to cell killing, but evidence is beginning to mount that senescence is not a homogenous response and this proliferative arrest is not uniformly durable [85, 93-98]. These cells which enter a "senescence-like state" and then escape emerge with dynamic genotypic and phenotypic changes which tend to make them more malignant and likely to lead to cancer recurrence [97, 99].

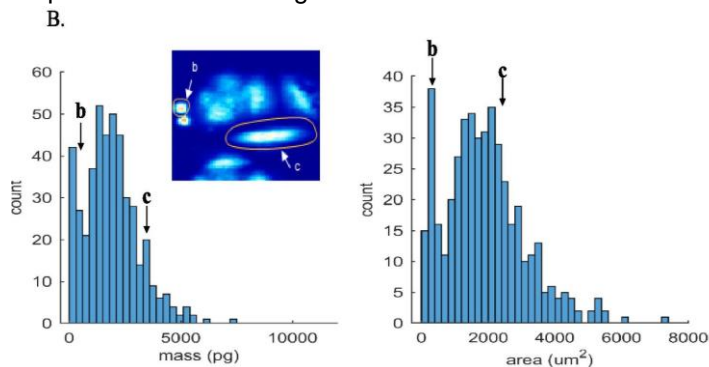
In this chapter, we will address some of these questions by first using HSLCI to distinguish senescent cells based on cell size and cell growth. Next, we evaluate cells that escape from senescence and finally test BCL-2 inhibitor navitoclax (ABT-263) as a potential therapy for eliminating senescent cells.

Before, these HSLCI studies are elaborated upon a matter of semantics must be addressed. Frequently the debate about senescence has suffered from a circular argument. Even if cells express all the hallmarks of senescence (changes in size, increased SA- $\beta$ -gal expression, SASP, and SAHF) if they are observed to recover, these cells must not be senescent because senescence is irreversible by definition.

Many studies cited above and reviewed here [92] (including our own) have demonstrated either the heterogeneity of cells with senescent features and/or the ability of these cells to proliferatively recover. This work therefore views senescence on a spectrum of drug response ranging from cell death to quiescence to completely unaffected.

## 7.2 Changes in cell size

To investigate the observed change in single cell size at a population level, H460 lung cancer cells were exposed to the DNA-damaging drug etoposide for 24 hours. Mass and area measurements of control and etoposide-treated single cells were taken on day 4 post-etoposide exposure (



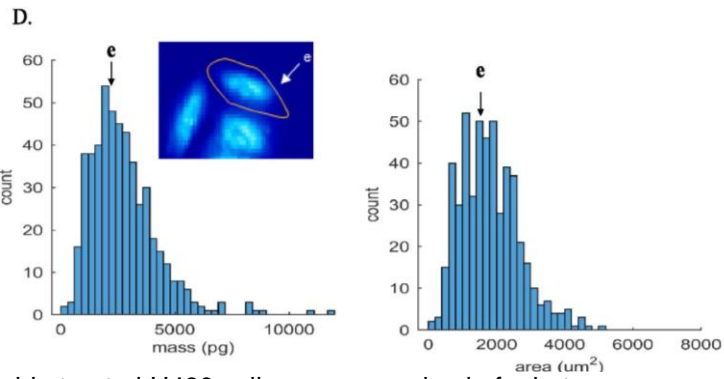
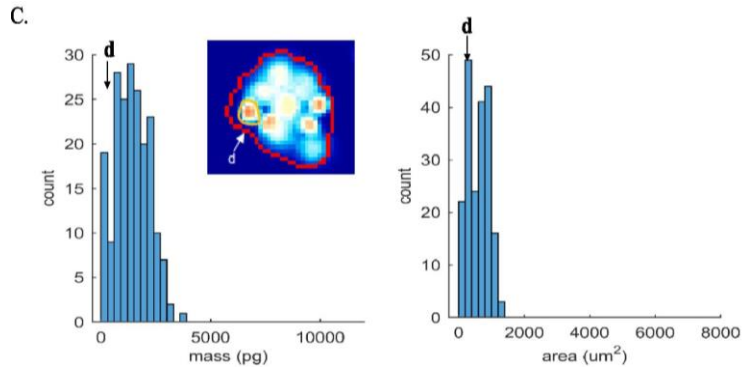
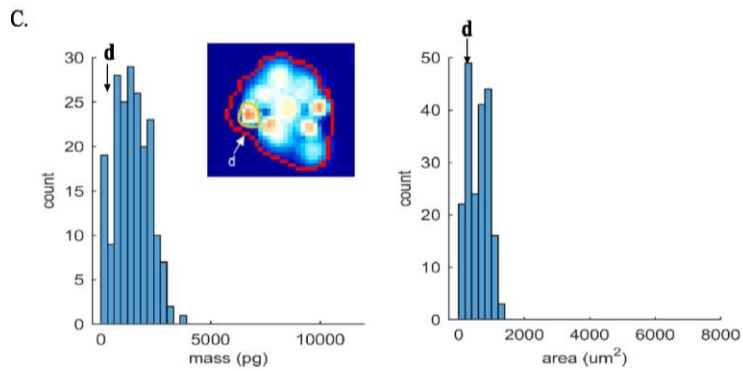
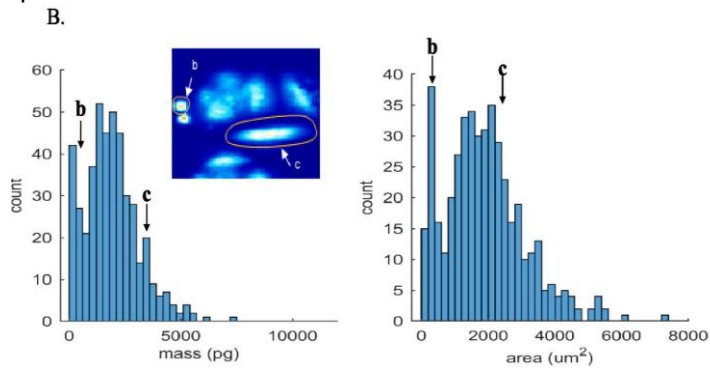


Figure 25). The etoposide treated H460 cells were comprised of a heterogeneous population that differed markedly in mass and area, consistent with the heterogeneous response to drug exposure in previous qualitative observations. As can be seen in the population histograms in



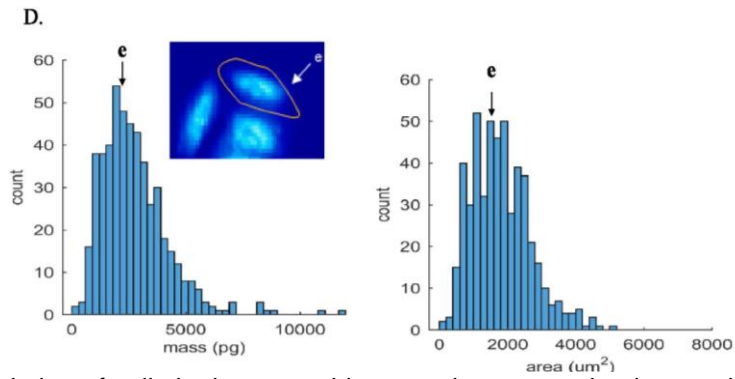
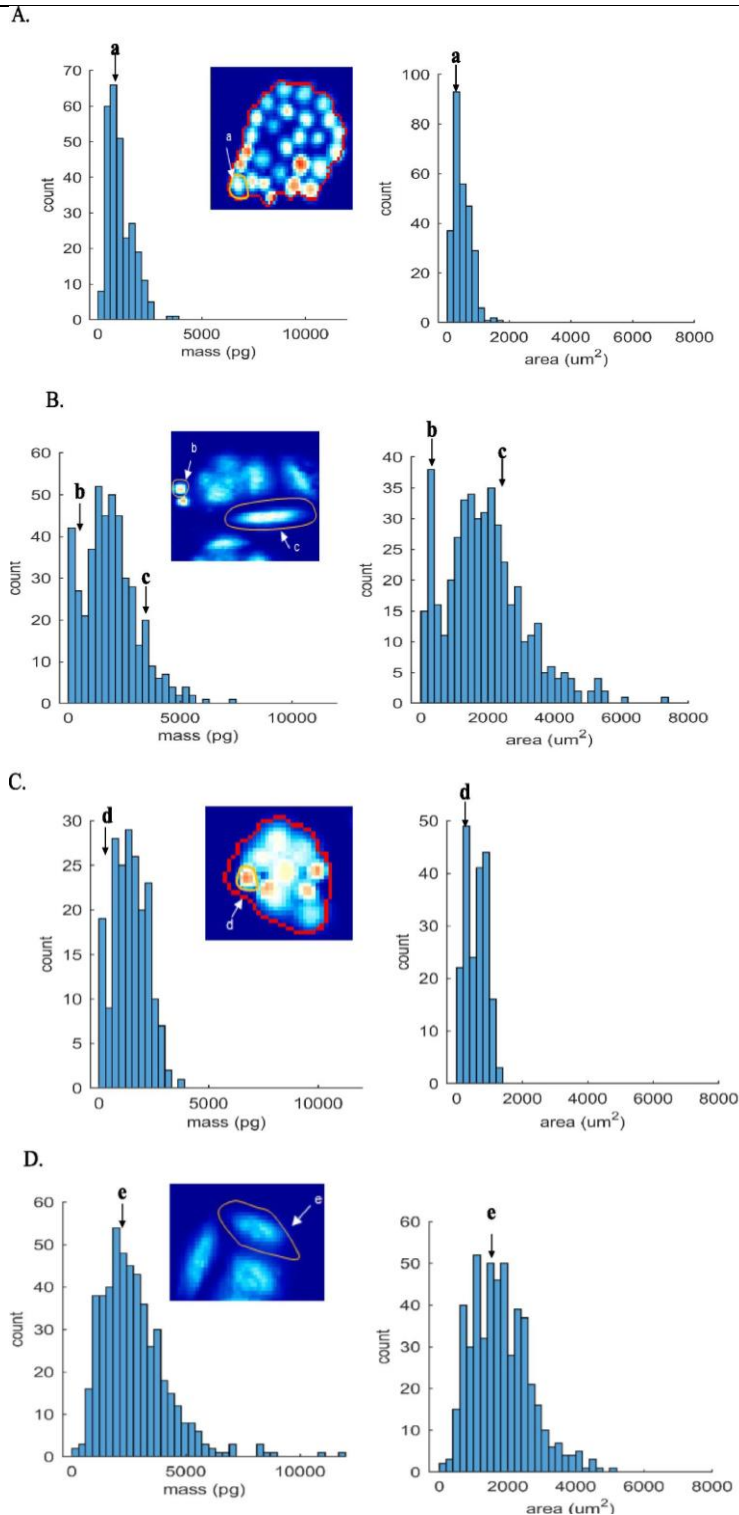


Figure 25, a subpopulation of cells in the etoposide treated group retained essentially the same mass as control cells while the majority of the population increased in mass and area. For example, in the same inset image of the etoposide treated, but unsorted population, cell **b** has a mass and area of 853 pg and 423  $\mu\text{m}^2$ , respectively, which is roughly comparable to that of control cell **a** (618 pg, 207  $\mu\text{m}^2$ ) while cell **c**, which exhibits a senescent-like, flat, enlarged morphology, has a mass of 4981 pg and an area of 2646  $\mu\text{m}^2$



**Figure 25: Mass and area distribution of etoposide-treated and etoposide-treated and enriched high- $C_{12}FDG$  and low- $C_{12}FDG$  H460 cells.**

A) Vehicle ( $n = 272$ ). (B) Etoposide-treated ( $n = 447$ ) (C) Low-  $C_{12}FDG$  ( $n = 199$ ) and (D) High-  $C_{12}FDG$  cells ( $n = 505$ ). The etoposide treated population appears to be composed of at least two populations, specifically the high-  $C_{12}FDG$  and low-  $C_{12}FDG$  cells, indicative of the heterogeneous size response to etoposide. Cell which are labeled in the histograms are shown in the insets.

When flow cytometry-based enrichment for SA- $\beta$ -gal fluorogenic substrate C<sub>12</sub>FDG was coupled to HSLCI, we were able to generate a profile of mass and area for the high and low expression populations. Representative example cells of the low C<sub>12</sub>FDG population, cell **d** (727 pg, 279  $\mu\text{m}^2$ ), and high C<sub>12</sub>FDG population, cell **e** (2515 pg, 2250  $\mu\text{m}^2$ ), reflect the observation that the high- C<sub>12</sub>FDG cells were increased in mass and area while the low C<sub>12</sub>FDG remained similar in mass and area to control cells. **Table 1** provides a summary of the median mass and area for control cells, unsorted cells after etoposide treatment, and high and low C<sub>12</sub>FDG populations. On a population level, control cells had a median mass of 917  $\pm$  79 pg and a median area of 431  $\pm$  71  $\mu\text{m}^2$  while the unsorted etoposide-treated cells had a median mass and area of 1799  $\pm$  149 pg and 1355  $\pm$  117  $\mu\text{m}^2$ , respectively ( $p < 0.001$ ). High- C<sub>12</sub>FDG cells (i.e. after sorting) had a median mass of 2491  $\pm$  171 pg, and median area per cell of 1683  $\pm$  131  $\mu\text{m}^2$ , while in the low- C<sub>12</sub>FDG population of cells, median mass was 1386  $\pm$  147 pg and median area was 627  $\pm$  99  $\mu\text{m}^2$  ( $p < 0.001$ ). These observations indicate that etoposide treatment results in a dramatic dysregulation of cellular biomass; the majority of cells are large in size, consistent with the cellular flattening that characterizes the senescence-like phenotype, while the minority of cells that maintain biomass regulation are unlikely to enter a senescence-like state after exposure to etoposide. These observations have been confirmed by other groups [3].

	<b>Median mass (pg)</b>	<b>Median area (<math>\mu\text{m}^2</math>)</b>
<b>Control</b>	917 $\pm$ 79	431 $\pm$ 71
<b>ETO</b>	1799 $\pm$ 149	1355 $\pm$ 117
<b>Low-C<sub>12</sub>FDG</b>	1386 $\pm$ 147	627 $\pm$ 99
<b>High-C<sub>12</sub>FDG</b>	2491 $\pm$ 171	1683 $\pm$ 131

**Table 1: HSLCI biomass and area measurements of pre and post sorted H460 cells.**

Post sorting high- C<sub>12</sub>FDG cells (n = 505) exhibit higher mass and area than the post-sorted low- C<sub>12</sub>FDG cells (n = 199) and the pre-sorted etoposide-treated H460 cells (n = 447).



### 7.3 Changes in cell growth and escape from senescence

Predictably, cell mass growth was depressed in the etoposide-treated population after about 12 hours of treatment. It then began to recover on day 2 as cells began to increase in size without dividing as shown in

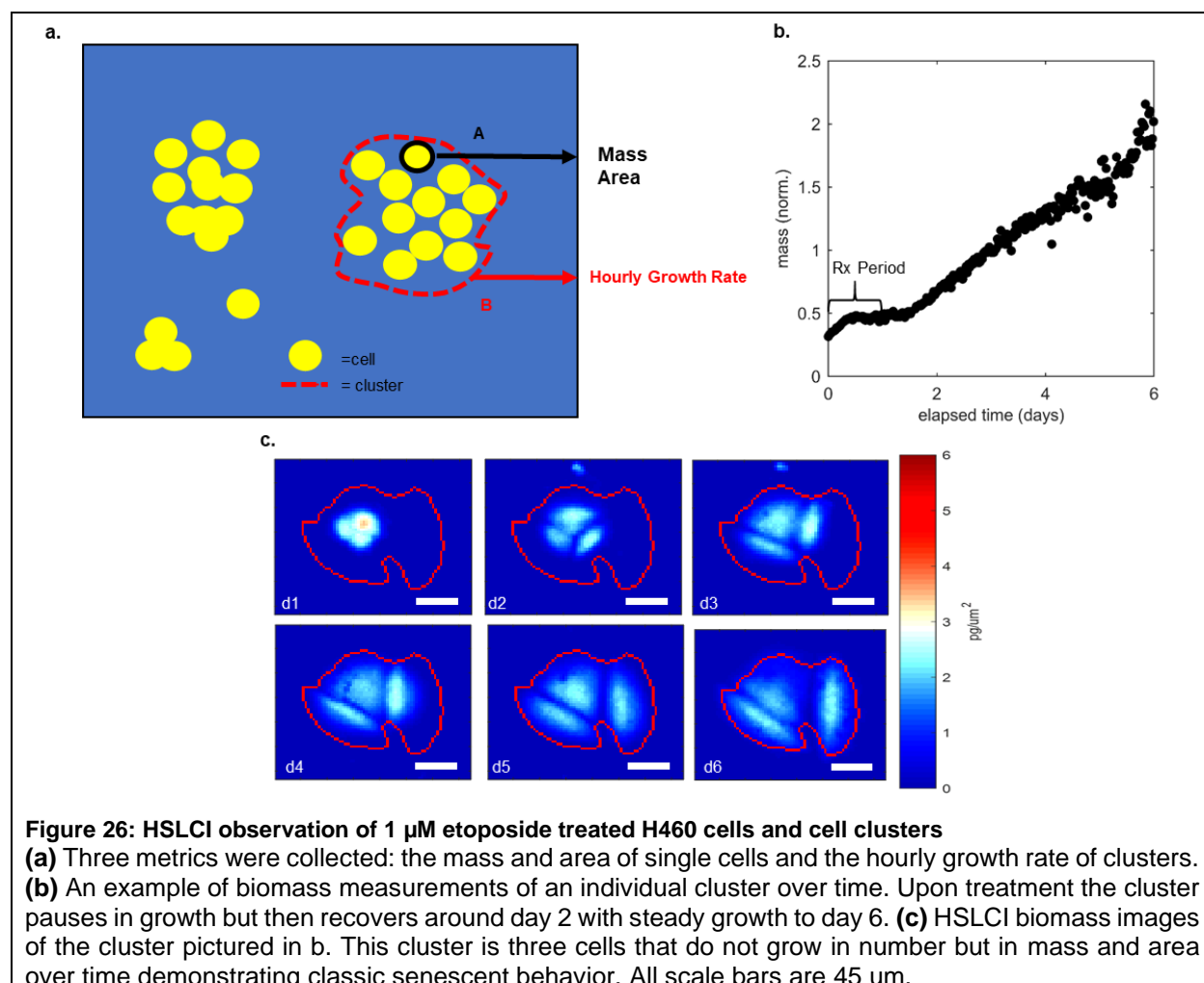


**Figure 26: HSLCI observation of 1  $\mu\text{M}$  etoposide treated H460 cells and cell clusters**  
(a) Three metrics were collected: the mass and area of single cells and the hourly growth rate of clusters.  
(b) An example of biomass measurements of an individual cluster over time. Upon treatment the cluster pauses in growth but then recovers around day 2 with steady growth to day 6.  
(c) HSLCI biomass images of the cluster pictured in b. This cluster is three cells that do not grow in number but in mass and area over time demonstrating classic senescent behavior. All scale bars are 45  $\mu\text{m}$ .

an example in **Figure 26**. As H460 cells often cluster tightly, analysis had to be performed on clusters instead of single cells.

The broad range of responses is shown in **Figure 27**. The normalized mass vs time plots for individual cell clusters is shown with each gray dot representing a measurement at one time point. The blue line is the median normalized mass at each time point and black lines representing the 95% confidence interval in the median at each point. Only biomass growth tracks which fit either linear or exponential model of growth with  $R^2 > 0.85$  were included.

Vehicle treated cells grew exponentially at a rate of 3.58% [3.56-3.59%] ([95%CI]) per hour. Cells treated with etoposide for 24 hours showed significantly delayed growth with median growth at 1.29% [1.27-1.31%] but with significant variance with exponential growth from 0.6% to 2.6%.

Four days after treatment, cells lacking the characteristic size increase and with low  $C_{12}\text{FDG}$  expression grew at an exponential hourly growth rate of 3.41% [3.38-3.45%] per hour recovering growth similar to cells never treated with etoposide (vehicle), 3.58% [3.56-3.59%] per hour. In contrast,  $C_{12}\text{FDG}$ - high cells continued expanding much more slowly (1.33% [1.30-1.35%] per hour) over the same 48 hour time period with some heterogeneity and a few cell clusters recovering modest growth, as previously published [94].

In clusters in which the number of cells was clearly countable, the mean single cell area and mean single cell mass were determined. A relatively linear relationship is evident between average cell size and mass growth rate of the cluster (**Supplementary Figure 5**). Clusters composed of small cells grew quickly while those with larger cells grew more slowly.

The heterogeneity of response to etoposide treatment extends not only to those cells which exhibit the characteristic signatures of senescent cells ( $C_{12}FDG$ -high) versus those that do not ( $C_{12}FDG$ -low) but even within the senescent population where some cluster grew at a rate of 3-4% which is almost equal to median growth of control cells while the majority of cells grew much more slowly.

Of special interest are cells that recover robustly from drug treatment. Cells that recover from drug treatment could be sources of resistance in patients and being able to identify them in a heterogenous population through biomass change can enable isolation and further study for research or clinical information.

**Figure 28** details examples of three biomass growth tracks. A control cell (orange) had steady exponential growth (4.0% [3.97-4.04%]) by day 5 of observation control cells had begun to overrun the plate. *Tx Track #1* (1.9% [1.87-1.98%]) (blue) starts with three cells that maintain their morphology dividing multiple times, while *Tx track #2* (grey) has cells that during the Tx period (0-24 hours) enlarge size at 1.49% [1.44-1.53%]. At day five there is a temporary loss in cell mass as division occurs and growth resumes. This loss is similar to what others have seen if slightly larger [25]. As etoposide is known to lead to mitotic dysfunction, it is perhaps unsurprising that an exaggerated loss of mass might occur [100].

During the screening period of 24-48 hours after drug treatment both tracks have growth rates above the median growth rate of  $C_{12}FDG$ -high cells of 1.2% [1.23-1.34] per hour four to six days after treatment.

Similar trends can be seen in sorted cells four to nine days after treatment. In **Figure 29**, examples of untreated (vehicle), non-senescent recovery ( $C_{12}FDG$ -low), senescence with recovery ( $C_{12}FDG$ -high #1) and senescence without recovery are shown ( $C_{12}FDG$ -high #2). The vehicle (black, 1<sup>st</sup> panel) and  $C_{12}FDG$ -low (orange, 2<sup>nd</sup> panel) grew exponentially at 4.37% [4.21-4.54] and 4.55% [4.45-4.66%] respectively while remaining small and overrunning the wells shortly after six days after treatment.

$C_{12}FDG$ -high #1 (blue, 3<sup>rd</sup> panel) has cell divisions on days four and six (images shown) after which cells regain their larger sizes, but by day nine many divisions have occurred, and cell size has shrunk. This behavior results in exponential growth at 1.99 [1.83-2.15%] over the days four to nine after treatment. In

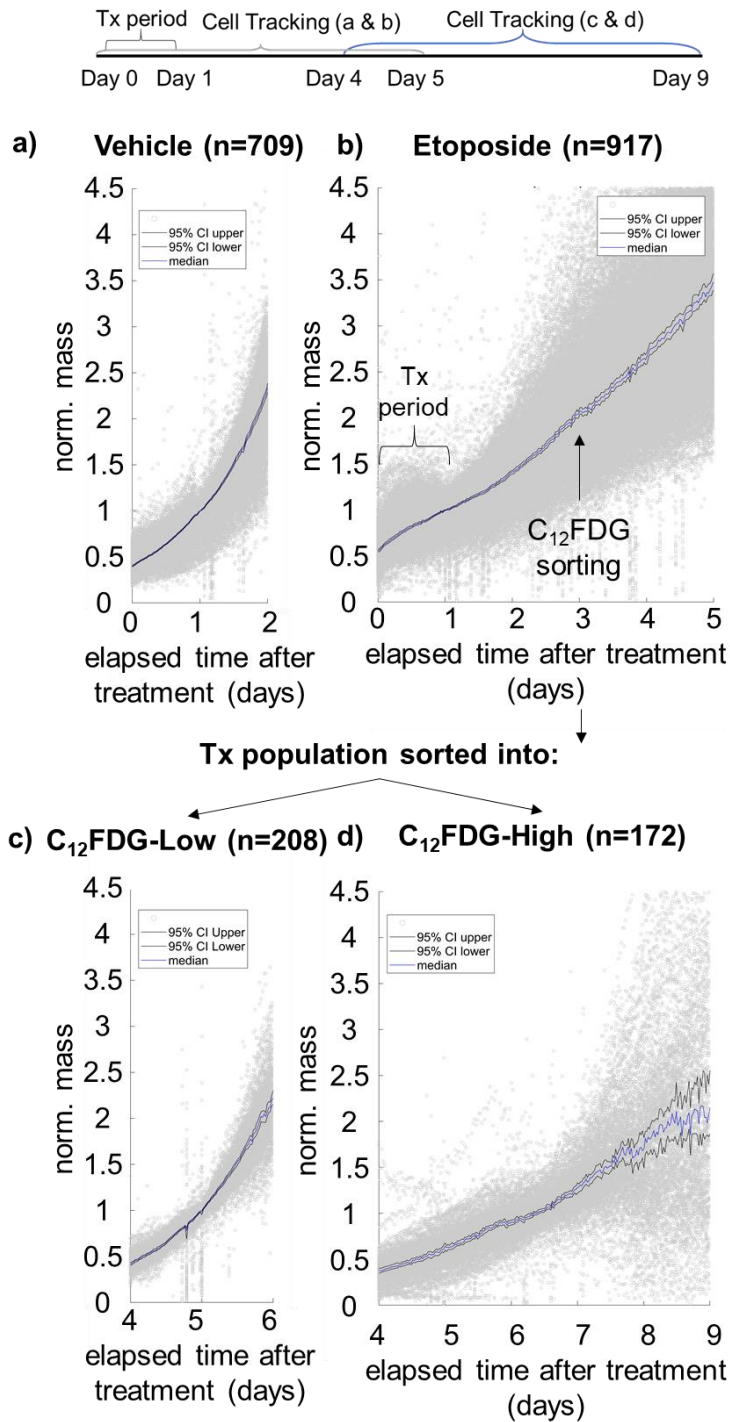


**Figure 27: Biomass growth rates of etoposide treated and C<sub>12</sub>FDG sorted H460 cells from 0 to up to 9 days after treatment**

Four representative examples of biomass growth rates of vehicle treated (a, 3 replicates, day 0-2), etoposide treated (b, Tx, 2 replicates day 0-5), C<sub>12</sub>FDG-high (d, 2 replicates, day 4-9), and C<sub>12</sub>FDG-low (c, 2 replicates, day 4-6) H460 cells. The n above the graphs refers to the number of cell cluster biomass growth tracks in the replicates shown. Only biomass growth tracks which fit either linear or exponential model of growth with  $R^2 > 0.85$  were included.

contrast, C<sub>12</sub>FDG-high #2 (orange, 4<sup>th</sup> panel) demonstrates more typical senescent growth in size at 1.04% [1.00-1.07%] with a decreasing density.

Just as previous work has shown heterogeneity in the senescent population with subpopulations of cells escaping senescence [94, 96, 97], this is yet another example that the expression of classical senescent phenotypes does not lead to one-type-fits-all behavior. This heterogeneity, which can lead to undesirable consequences such as the development of cancer stem cell characteristics, indicates a compelling need for careful considerations when using therapies which may produce senescent outcomes. A caveat must be made that H460 is an immortal robustly growing cell line, and these results must be taken in context. Studies in primary tissues would be an appropriate follow on.

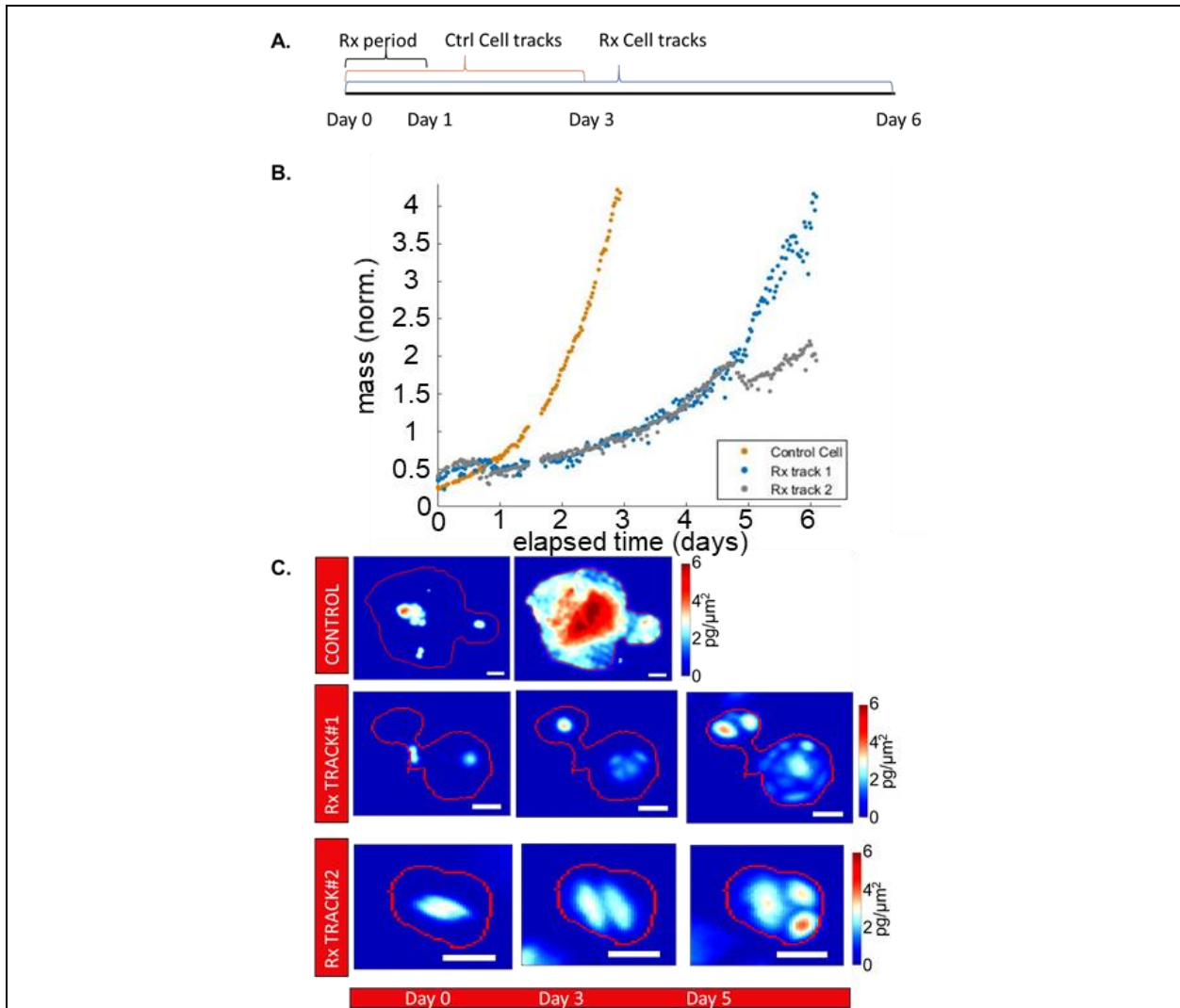


**Figure 28: HSLCI analysis of low-dose etoposide treatment shows variable patterns of growth arrest including a senescence phenotype**

A. A schematic representing the treatment (Rx) and live interferometry tracking periods for B & C which were performed at 10x. B. One control and two representative Rx growth tracks cell clusters shown in C. Mass is normalized to the median mass for each cell cluster over the tracking time period. Tracking began during the Rx period and an arrest of growth is seen between day 0-1. Rx track #1 cells show exponential growth by day 5. Rx track #2 shows continued growth with a decrease and subsequent recovery after a cell division C. Control cells remain small and grow quickly into a colony by day 3. Rx track #1 cells stay morphologically similar to control cells and have recovered exponential growth by day 5. Rx track #2 two cells become large similar to senescent cells and by day 5 have gone through two divisions. All scale bars are 45  $\mu\text{m}$

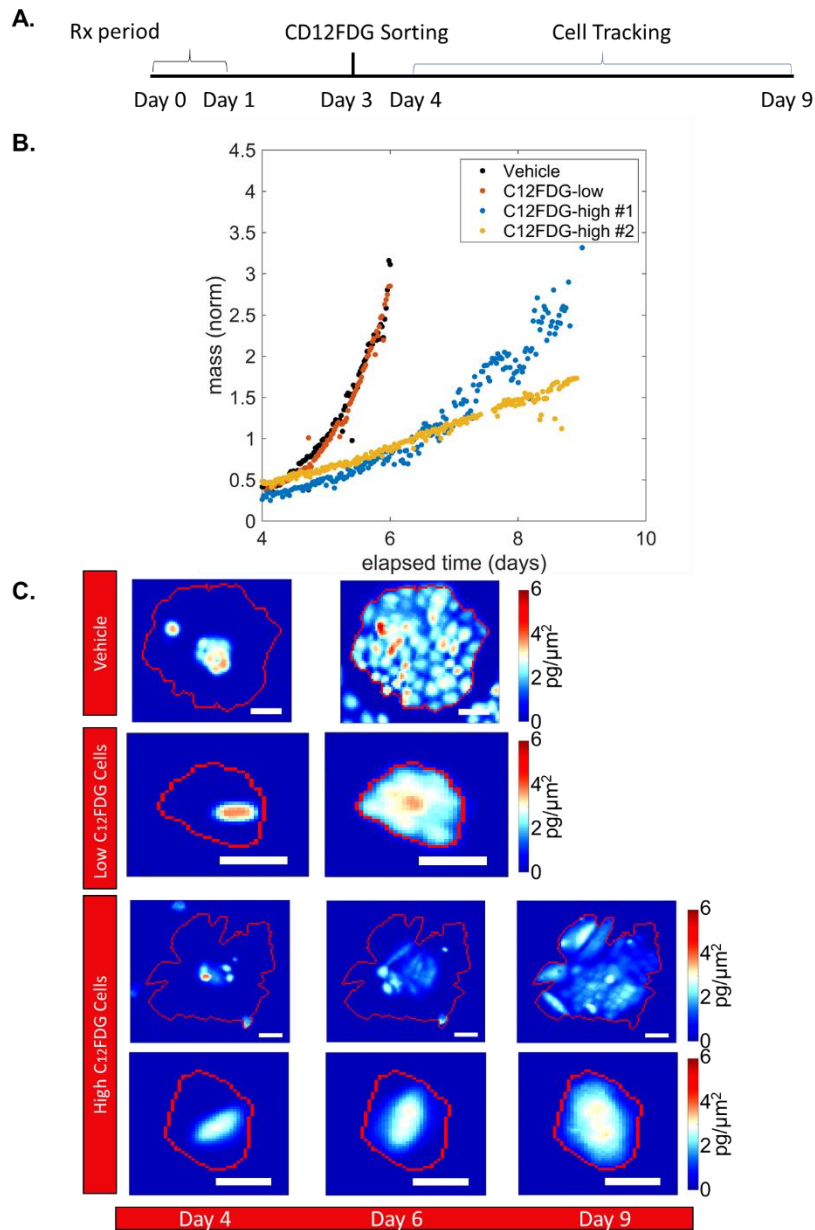
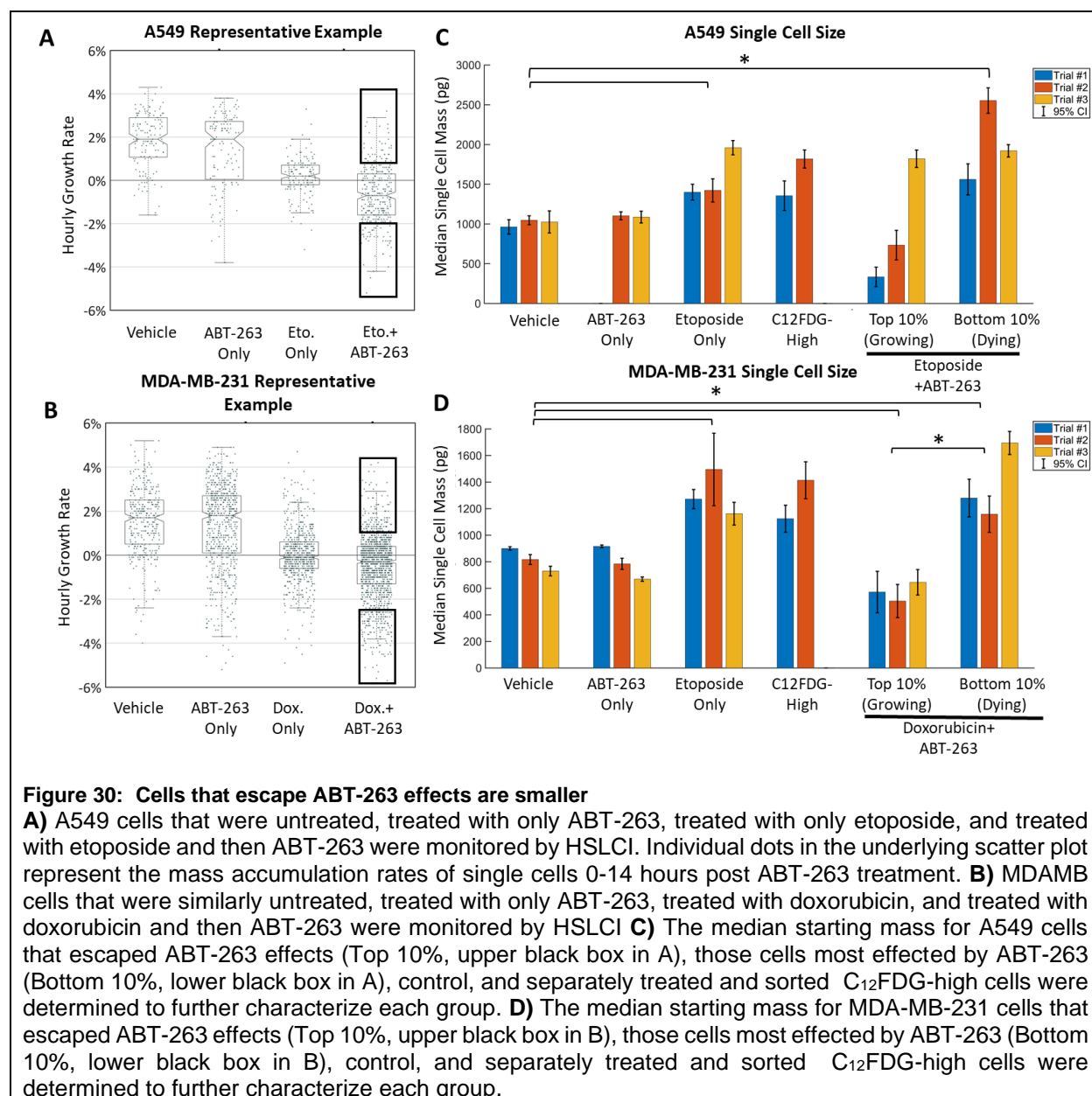


**Figure 29: HSLCI analysis of H460 sorted, senescent cells shows that proliferative recovery originates in  $\beta$ -gal positive cells.**

**A.** A schematic representing the treatment, sorting, and live interferometry tracking periods for B & C which were performed at 10x. **B.** The norm. mass versus time plots for the four cell clusters shown in C.

**C.** Control and C<sub>12</sub>FDG-low cells remained small and formed larger colonies by day 6 after treatment. The wells were overrun with cells shortly after day 6. In contrast, C<sub>12</sub>FDG-high #1 cells in the 3<sup>rd</sup> panel demonstrated proliferative recovery. These cells had the larger senescent phenotype and grew into colonies by day 9 with single cell sizes gradually shrinking. Recent cell divisions are shown in the images for days 4 and 6. The C<sub>12</sub>FDG-high #2 cells demonstrated more common growth with continue enlargement with a decrease in density. All scale bars are 45  $\mu\text{m}$ . Outlier points were removed from C<sub>12</sub>FDG-high #1.

## 7.4 Treatment with ABT-263



As it has become apparent that senescent cells could be a source of tumor recurrence, interest in targeting them with therapy has grown. The selective removal of senescent cells from progeroid animals has been shown to ameliorate several aging phenotypes and established pathologies where senescent cells play a pathogenic role such as myocardial infarction, obesity and diabetes [101, 102]. In this context, a powerful model to eliminate senescent cells is the use of the established BCL-2/BCL-XL inhibitor, ABT-263 (navitoclax) as a senolytic adjuvant in cancer therapy [103, 104]. BCL-2/BCL-XL are typically redundantly upregulated in senescent cells preventing apoptosis from clearing the cells [103].

While ABT-263 is usually applied in combination with chemotherapy, we have tested a novel sequential therapeutic approach; specifically, once the tumor cells enter into an established state of senescence, ABT-263 is used as a 'clearing' agent in an effort to eliminate the residual senescent tumor cells

To investigate which cells specifically responded to ABT-263, A549 lung cancer and MDA-MB-231 breast cancer cell lines were treated with either etoposide (Eto) or doxorubicin (Dox) respectively and then exposed to ABT-263. HSLCI was employed to monitor biomass changes of individual cells during this ABT-263 treatment. The addition of ABT-263 depressed median growth to 0% or below, indicating loss of mass and therefore cell death, but only in cells pretreated with Eto or Dox (**Figure 30A,B**), as shown previously. However, a small population within the Eto- and Dox-treated populations maintained a positive growth rate, indicating that some cells had escaped the effects of ABT-263 (**Figure 30A,B**). Determination of the single cell mass at the initiation of ABT exposure (time 0) confirmed our previous finding that SA- $\beta$ -gal-positive cells are significantly larger than either control or SA- $\beta$ -gal-negative cells [94].

In three replicates, A549 median control cell mass ranged from  $963 \pm 90$  pg to  $1047 \pm 56$  pg, while the median SA- $\beta$ -gal-positive cell mass ranged from  $1356 \pm 186$  pg to  $1818 \pm 114$  pg. MDA-MB-231 median control cell mass ranged from  $730 \pm 36$  pg to  $900 \pm 13$  pg, while the median SA- $\beta$ -gal-positive cell mass ranged from  $1124 \pm 102$  pg to  $1414 \pm 139$  pg.

For MDA-MB-231 cells treated with Dox + ABT-263, the top 10% of growing cells (cells that do not die with ABT-263) were consistently smaller than SA- $\beta$ -gal-positive cells, while the bottom 10% of cells by growth rate (dying cells) were the same size (**Figure 30D**). These cell size measurements suggest that the cells that are unaffected by ABT-263 are likely not senescent. Similar trends were observed in Eto + ABT-263-treated A549 cells (**Figure 30C**). Overall, these size analyses emphasize ABT-263 specificity, as ABT-263 affects characteristically large senescent cells while sparing smaller cells which have not undergone senescence as a response to the topoisomerase inhibitors.

## 7.5 Methods

### Cell staining and sorting

The  $C_{12}$ FDG staining protocol was adopted from Debacq-Chainiaux et al and performed by members of the Gewirtz Lab [105]. For the enrichment assay, H460, MDAMB-231, and A549 cells were seeded at  $1-2 \times 10^6$ /150 mm dish and cultured overnight before being exposed to etoposide or doxorubicin ( $1 \mu\text{M}$ ) for 24 h. On day 3, the cells were exposed to bafilomycin A1 ( $100 \text{ nM}$ ) for 1 h, followed by incubation with  $C_{12}$ FDG in complete medium for 2 h. Cells were then harvested and sorted by flow cytometry (using BD FACSCanto II and BD FACSDiva software at the Virginia Commonwealth University Flow Cytometry Core Facility) based on parameters detailed in previous work [94].

### HSLCI H460 senescence characterization experiments

For the unsorted cell experiment, H460 cells were plated in a 24-well optical glass-bottomed plate (catalog no. P24-0-N, Cellvis) at  $1 \times 10^4$  cells/ml with a total of 1 ml of medium (DMEM described above) in each well. Plated cells were allowed to adhere overnight. Cells were then exposed to  $1 \mu\text{M}$  of etoposide and put inside the HSLCI for imaging for 6 days at 10x or 20x,  $37^\circ \text{C}$ , and 5%  $\text{CO}_2$ . Media was replaced after 24 hours of drug exposure and then every 48 hours after that. When using sorted cells, high-  $C_{12}$ FDG, low-  $C_{12}$ FDG and untreated control cells were plated and allowed to adhere overnight, followed by monitoring in the HSLCI for 5 days at 10x or 20x at  $37^\circ \text{C}$ , and 5%  $\text{CO}_2$ . Media was replaced every 48 hours.

### HSLCI ABT-263 experiments

For these experiments, MDA-MB-231 or A549 cells were plated in a 24-well optical glass-bottomed plate (Cellvis, Mountain View, CA, USA) at  $1-5 \times 10^4$  cells per well and allowed to adhere. Cells were then exposed to  $8.7 \mu\text{M}$  of etoposide for 3 days (A549) or  $0.75 \mu\text{M}$  doxorubicin (MDA-MB-231) for 2 h. ABT-263 was given the same day as removal of etoposide or 4 days after the removal doxorubicin. After ABT-263 dosing, the plate was placed inside the HSLCI for imaging for 14 h at 20x,  $37^\circ \text{C}$ , and 5%  $\text{CO}_2$ . When using sorted cells, high-  $C_{12}$ FDG cells were plated and allowed to adhere overnight, followed by monitoring in the HSLCI for 14 h at 20x,  $37^\circ \text{C}$ , and 5%  $\text{CO}_2$ . Cell mass is tracked from image to image, either individually or in a cluster.

## 8 Conclusions and Future Directions

### 8.1 HSLCI as a clinical screening tool

The work comparing biomass growth rates of three TNBC PDXs treated with carboplatin *in vitro* to *in vivo* treatment in **Chapter 3** was the first step in developing HSLCI as a screening tool. Additionally, the work in **Chapter 5.1** proving HSLCI's compatibility with fine needle biopsy procedures demonstrates the feasibility of screening material from patients. While additional *in vivo-in vitro* correlations have been made (**Supplementary Figure 6**), what is still needed is a larger scale screen of more drugs both *in vivo* and *in vitro* to assess the strength and weakness of HSLCI as a screening tool.

Current gold standard *in vitro* drug screening methods are based on metabolic fluorescence assays, but their bulk averaging nature leads to low specificity (~70%) for identifying drug sensitivity [106]. When many drugs (30%) are considered sensitive *in vitro*, but fail *in vivo*, it is hard for a clinician to rely on such an assay for decision making. This high false positive rate could be due to the bulk averaging nature of metabolic fluorescence-based assays as the measurement of metabolic rate as read by fluorescence for the entire well.

The question that still must be answered is: will the single cell nature of HSLCI measurements lower this false positive rate by identifying significant drug resistant subpopulations? The first steps on how to answer this question are shown in **Figure 31**.

At the relevant doses (indicated by “^”) does a lack of drug tolerant cells in ABT-263 treated WHIM2 cells predict better *in vivo* response than afatinib where single cells continue growing robustly well above the max concentration of afatinib seen in patients?

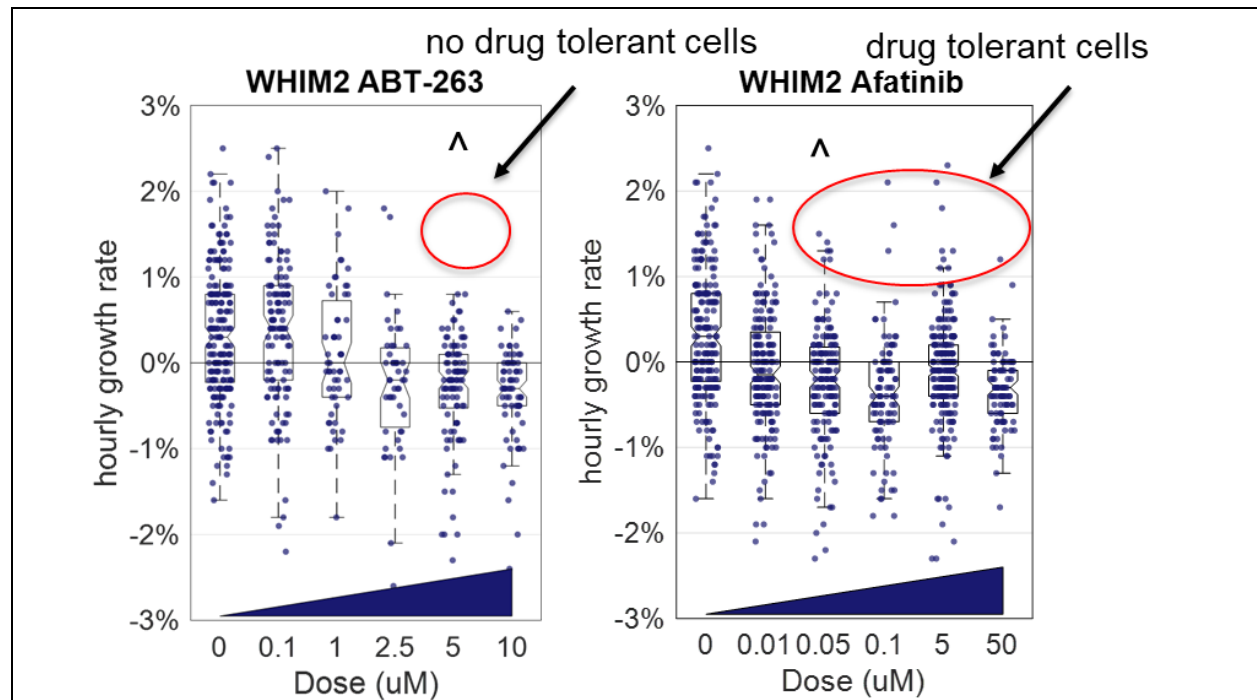


**Figure 31: HSLCI as a clinical screening tool**

HSLCI's advantage as a screening tool is its single cell level detection. Although both ABT-263 and afatinib have median growth below zero at corresponding maximum concentrations seen in patient's blood “^”, afatinib has a significant number of cells growing robustly while ABT-263 does not. Will the presence of these drug tolerant cells in afatinib lead to the development of drug resistance *in vivo* and can HSLCI predict this by detecting these cells at early stages?



The advantage of HSLCI in comparison to metabolic fluorescence assays is evident even with only these two drugs. While the median rates of single cells at relevant doses for both drugs is just below 0%, only afatinib has cells growing well above 1%, information that would be lost by bulk averaging. But only multiple *in vitro-in vivo* experiments will be able to answer these questions.

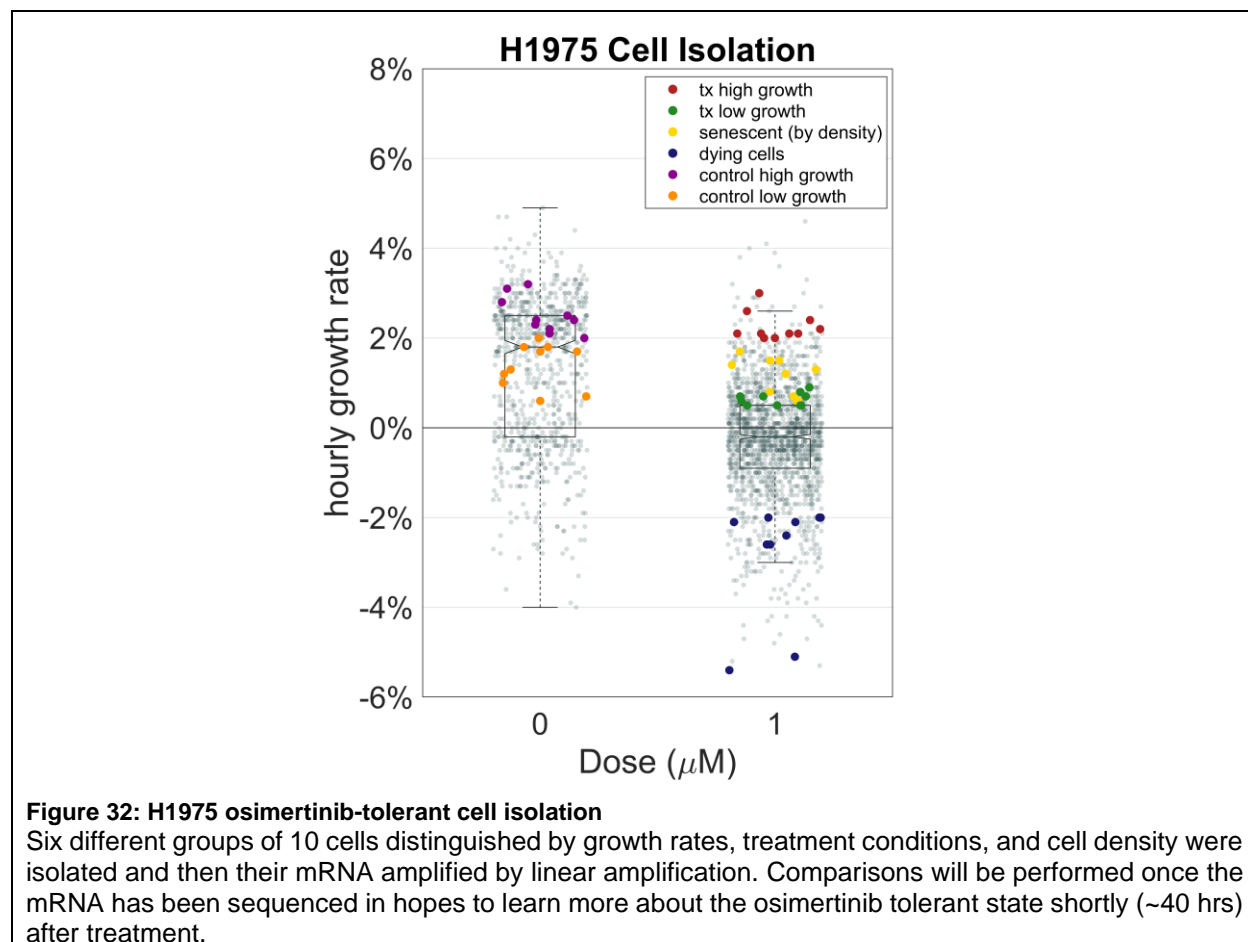
## 8.2 HSLCI as a translational research tool

With the micropipette cell isolation system now built and extensively tested, HSLCI can be used to identify drug tolerant cells and compare them to the greater population to identify possible druggable targets to prevent the development of drug resistance. In a first attempt at this, H1975 lung cancer cells were treated with 1 $\mu$ M of the epidermal growth factor receptor (EGFR) inhibitor osimertinib.

Six different groups of cells were isolated, demonstrating our systems compatibility with attached cells.

First, drug tolerant cells were isolated. Next, senescent cells identified by their decreased cell density, increased cell size, and decreased biomass growth rates were isolated. Then single cells with little growth and cells that were actively losing mass were isolated. Finally control cells displaying growth equivalent to the drug tolerant cells, and control cells with slightly depressed growth were isolated.

The messenger RNA in these six samples was then amplified by Eberwine amplification, which is linear anti-sense RNA amplification[107, 108]. Single cell PCR tends to favor high-abundance, while linear amplification preserves the expression of the lower expressed genes but is 3' biased [107-109]. The samples will be sent off for sequencing.



### *8.3 HSLCI as basic research tool*

Using HSLCI and other mass measurements tools we have begun to understand the process of the senescence in a new dynamic way [3, 94]. But in most cases basic understanding of how cells control their size under no perturbations and with drug treatments is still sorely lacking [1, 2]. Utilizing HSLCI's built in throughput connected with fluorescent reporting of specific gene expression may be key to unlocking a deeper understanding of how single size control works. This space remains open for exploration.

### *8.4 Conclusion*

Over the course of this work, HSLCI has matured to maximize throughput reaching the maximum speed of the camera (32 frames per second) and the ability to process data for thousands of cells in real time. While technological improvements will always continue, the groundwork has been laid for larger scale studies to test HSLCI's ability for clinical screening patient samples, isolating drug resistant cells and understanding the basic mechanisms of cell size regulation.

## List of References

1. Lloyd, A.C., *The regulation of cell size*. Cell, 2013. **154**(6): p. 1194-205.
2. Cadart, C., et al., *The physics of cell-size regulation across timescales*. Nature Physics, 2019. **15**(10): p. 993-1004.
3. Neurohr, G.E., et al., *Excessive Cell Growth Causes Cytoplasm Dilution And Contributes to Senescence*. Cell, 2019. **176**(5): p. 1083-1097 e18.
4. Caron, A., D. Richard, and M. Laplante, *The Roles of mTOR Complexes in Lipid Metabolism*. Annu Rev Nutr, 2015. **35**: p. 321-48.
5. Adhikary, S. and M. Eilers, *Transcriptional regulation and transformation by Myc proteins*. Nat Rev Mol Cell Biol, 2005. **6**(8): p. 635-45.
6. Yu, F.X., B. Zhao, and K.L. Guan, *Hippo Pathway in Organ Size Control, Tissue Homeostasis, and Cancer*. Cell, 2015. **163**(4): p. 811-28.
7. Kim, C., et al., *Chemoresistance Evolution in Triple-Negative Breast Cancer Delineated by Single-Cell Sequencing*. Cell, 2018. **173**(4): p. 879-893 e13.
8. Stewart, C.A., et al., *Single-cell analyses reveal increased intratumoral heterogeneity after the onset of therapy resistance in small-cell lung cancer*. Nature Cancer, 2020.
9. Dagogo-Jack, I. and A.T. Shaw, *Tumour heterogeneity and resistance to cancer therapies*. Nat Rev Clin Oncol, 2018. **15**(2): p. 81-94.
10. Gerlinger, M., et al., *Intratumor heterogeneity and branched evolution revealed by multiregion sequencing*. N Engl J Med, 2012. **366**(10): p. 883-892.
11. Barer, R., K.F. Ross, and S. Tkaczyk, *Refractometry of living cells*. Nature, 1953. **171**(4356): p. 720-4.
12. Barer, R., *Interference microscopy and mass determination*. Nature, 1952. **169**(4296): p. 366-7.
13. Brown, A.F. and G.A. Dunn, *Microinterferometry of the movement of dry matter in fibroblasts*. J Cell Sci, 1989. **92** ( Pt 3): p. 379-89.
14. Ross, K.F.A., *Phase Contrast and Interference Microscopy for Cell Biologists*. 1967, London: Edward Arnold.
15. Ruch, F. and G.F. Bahr, *Dry mass determination by interference microscopy; agreement with quantitative electron microscopy*. Exp Cell Res, 1970. **60**(3): p. 470.
16. Chun, J., et al., *Rapidly quantifying drug sensitivity of dispersed and clumped breast cancer cells by mass profiling*. Analyst, 2012. **137**(23): p. 5495-8.
17. Leslie, K.A., et al., *Reconstituting donor T cells increase their biomass following hematopoietic stem cell transplantation*. Analyst, 2018. **143**(11): p. 2479-2485.
18. Reed, J., et al., *Rapid, massively parallel single-cell drug response measurements via live cell interferometry*. Biophys J, 2011. **101**(5): p. 1025-31.
19. Reed, J., et al., *Live cell interferometry reveals cellular dynamism during force propagation*. ACS Nano, 2008. **2**(5): p. 841-6.
20. Burg, T.P., et al., *Weighing of biomolecules, single cells and single nanoparticles in fluid*. Nature, 2007. **446**(7139): p. 1066-9.
21. Cetin, A.E., et al., *Determining therapeutic susceptibility in multiple myeloma by single-cell mass accumulation*. Nature Communications, 2017. **8**: p. 1613.
22. Godin, M., et al., *Using buoyant mass to measure the growth of single cells*. Nature Methods, 2010. **7**(5): p. 387-U70.
23. Nie, Z., et al., *High-speed mass analysis of whole erythrocytes by charge-detection quadrupole ion trap mass spectrometry*. Anal Chem, 2007. **79**(19): p. 7401-7.
24. Huang, D., et al., *High-Speed Live-Cell Interferometry: A New Method for Quantifying Tumor Drug Resistance and Heterogeneity*. Anal Chem, 2018. **90**(5): p. 3299-3306.
25. Miettinen, T.P., et al., *Mammalian cell growth dynamics in mitosis*. Elife, 2019. **8**.
26. Kimmerling, R.J., et al., *Linking single-cell measurements of mass, growth rate, and gene expression*. Genome Biol, 2018. **19**(1): p. 207.
27. Stevens, M.M., et al., *Drug sensitivity of single cancer cells is predicted by changes in mass accumulation rate*. Nat Biotechnol, 2016. **34**(11): p. 1161-1167.
28. Zangle, T.A. and M.A. Teitell, *Live-cell mass profiling: an emerging approach in quantitative biophysics*. Nat Methods, 2014. **11**(12): p. 1221-8.

29. Michelson, A. and E. Morley, *On the Relative Motion of the Earth and the Luminiferous Ether*. American Journal of Science, 1887.
30. Allen, L., et al., *The Hubble Space Telescope Optical Systems Failure Report*, N.A.a.S. Administration, Editor. 1990.
31. Collaboration, L.S., et al., *Observation of Gravitational Waves from a Binary Black Hole Merger*. Physical Review Letters, 2016. **116**(6): p. 061102.
32. Lopez, C., et al., *Interferogram decodification on Nios II soft-core*, in *Semana Nacional de Ingeniería Electrónica*. 2014: Celaya, Mexico.
33. Thomas, D. and G. Duguid, *Optical coherence tomography--a review of the principles and contemporary uses in retinal investigation*. Eye (Lond), 2004. **18**(6): p. 561-70.
34. Zysk, A.M., et al., *Optical coherence tomography: a review of clinical development from bench to bedside*. J Biomed Opt, 2007. **12**(5): p. 051403.
35. Primot, J. and N. Guerineau, *Extended hartmann test based on the pseudoguiding property of a hartmann mask completed by a phase chessboard*. Appl Opt, 2000. **39**(31): p. 5715-20.
36. Bon, P., et al., *Quadriwave lateral shearing interferometry for quantitative phase microscopy of living cells*. Opt Express, 2009. **17**(15): p. 13080-94.
37. Leslie, K.A., *Evaluation and Adaptation of Live-Cell Interferometry for Applications in Basic, Translational, and Clinical Research*, in *Integrative Life Sciences*. 2018, Virginia Commonwealth University.
38. Guest, D., *Quantitative Analysis and Process of High Speed Live Cell Interferometry Measurements*, in *Department of Physics*. 2017, Virginia Commonwealth University.
39. Coit, D.G., et al., *Cutaneous Melanoma, Version 2.2019, NCCN Clinical Practice Guidelines in Oncology*. J Natl Compr Canc Netw, 2019. **17**(4): p. 367-402.
40. Noone AM, H.N., Krapcho M, Miller D, Brest A, Yu M, Ruhl J, Tatalovich Z, Mariotto A, Lewis DR, Chen HS, Feuer EJ, Cronin KA (eds). *SEER Cancer Statistics Review, 1975-2015*. 2017; Available from: [https://seer.cancer.gov/csr/1975\\_2015/](https://seer.cancer.gov/csr/1975_2015/).
41. Bevers, T.B., et al., *Breast Cancer Screening and Diagnosis, Version 3.2018, NCCN Clinical Practice Guidelines in Oncology*. J Natl Compr Canc Netw, 2018. **16**(11): p. 1362-1389.
42. Gradishar, W.J., et al., *Breast Cancer, Version 4.2017, NCCN Clinical Practice Guidelines in Oncology*. J Natl Compr Canc Netw, 2018. **16**(3): p. 310-320.
43. Giordano, S.H., A.D. Elias, and W.J. Gradishar, *NCCN Guidelines Updates: Breast Cancer*. J Natl Compr Canc Netw, 2018. **16**(5S): p. 605-610.
44. Merker, J.D., et al., *Circulating Tumor DNA Analysis in Patients With Cancer: American Society of Clinical Oncology and College of American Pathologists Joint Review*. J Clin Oncol, 2018. **36**(16): p. 1631-1641.
45. Sachs, N.a., *A Living Biobank of Breast Cancer Organoids Captures Disease Heterogeneity*. Cell, 2018. **172**: p. 373--386.
46. Aboulkheyr Es, H., et al., *Personalized Cancer Medicine: An Organoid Approach*. Trends Biotechnol, 2018. **36**(4): p. 358-371.
47. Reed, J., et al., *Rapid, massively parallel single-cell drug response measurements via live cell interferometry*. Biophysical journal, 2011. **101**(5): p. 1025--1031.
48. Chun, J., et al., *Rapidly quantifying drug sensitivity of dispersed and clumped breast cancer cells by mass profiling*. The Analyst, 2012. **137**(23): p. 5495.
49. Huang, D., et al., *High Speed Live Cell Interferometry: A New Method for Rapidly Quantifying Tumor Drug Resistance and Heterogeneity*. Analytical chemistry, 2018(90(5)): p. 3299-3306.
50. DeRose, Y.S., et al., *Patient-Derived Models of Human Breast Cancer: Protocols for In Vitro and In Vivo Applications in Tumor Biology and Translational Medicine*. 2013. **Chapter 14**: p. Unit14.23.
51. Oguri, S., et al., *Clinical Pharmacokinetics of Carboplatin*. The Journal of Clinical Pharmacology, 1988. **28**(3): p. 208--215.
52. Nair, A.B. and S. Jacob, *A simple practice guide for dose conversion between animals and human*. Journal of basic and clinical pharmacy, 2016. **7**(2): p. 27--31.
53. Turner, T.H., et al., *Characterizing the efficacy of cancer therapeutics in patient-derived xenograft models of metastatic breast cancer*. Breast cancer research and treatment, 2018. **170**: p. 221-234.

54. Sheetz, M.P., J.E. Sable, and H.-G. Dbereiner, *Continuous Membrane-Cytoskeleton Adhesion Requires Continuous Accommodation to Lipid and Cytoskeleton Dynamics*. Annual Review of Biophysics and Biomolecular Structure, 2006. **35**(1): p. 417-434.
55. Murray, G.F., et al., *Live Cell Mass Accumulation Measurement Non-Invasively Predicts Carboplatin Sensitivity in Triple-Negative Breast Cancer Patient-Derived Xenografts*. ACS Omega, 2018. **3**(12): p. 17687-17692.
56. Technologies, S. *EasySep™ Dead Cell Removal (Annexin V) Kit 2017; 1\_0\_1*:[
57. LoRusso, P.M., et al., *Pharmacokinetics and safety of bortezomib in patients with advanced malignancies and varying degrees of liver dysfunction: phase I NCI Organ Dysfunction Working Group Study NCI-6432*. Clin Cancer Res, 2012. **18**(10): p. 2954-63.
58. Brown, J., et al., *A Phase 1 Study Evaluating Pharmacokinetics (PK) and Safety of Carfilzomib in Patients with Advanced Malignancies and Varying Degrees of Hepatic Impairment (HI)*. Blood, 2016. **128**(22).
59. Gupta, N., et al., *Pharmacokinetics of ixazomib, an oral proteasome inhibitor, in solid tumour patients with moderate or severe hepatic impairment*. Br J Clin Pharmacol, 2016. **82**(3): p. 728-38.
60. Crawford, L.J., B. Walker, and A.E. Irvine, *Proteasome inhibitors in cancer therapy*. Journal of Cell Communication and Signaling, 2011. **5**(2): p. 101-110.
61. Weyburne, E.S., et al., *Inhibition of the Proteasome beta2 Site Sensitizes Triple-Negative Breast Cancer Cells to beta5 Inhibitors and Suppresses Nrf1 Activation*. Cell Chem Biol, 2017. **24**(2): p. 218-230.
62. Tate, S.C., et al., *A Population Pharmacokinetic and Pharmacodynamic Analysis of Abemaciclib in a Phase I Clinical Trial in Cancer Patients*. Clin Pharmacokinet, 2018. **57**(3): p. 335-344.
63. Yu, Y., et al., *Physiologically Based Pharmacokinetic Modeling of Palbociclib*. J Clin Pharmacol, 2017. **57**(2): p. 173-184.
64. Asghar, U.S., et al., *Single-Cell Dynamics Determines Response to CDK4/6 Inhibition in Triple-Negative Breast Cancer*. Clin Cancer Res, 2017. **23**(18): p. 5561-5572.
65. Hu, P., et al., *Single Cell Isolation and Analysis*. Front Cell Dev Biol, 2016. **4**: p. 116.
66. Guo, F., et al., *Three-dimensional manipulation of single cells using surface acoustic waves*. Proc Natl Acad Sci U S A, 2016. **113**(6): p. 1522-7.
67. Boumahdi, S. and F.J. de Sauvage, *The great escape: tumour cell plasticity in resistance to targeted therapy*. Nature Reviews Drug Discovery, 2020. **19**(1): p. 39-56.
68. Hata, A.N., et al., *Tumor cells can follow distinct evolutionary paths to become resistant to epidermal growth factor receptor inhibition*. Nature medicine, 2016. **22**(3): p. 262-269.
69. Song, K.-A., et al., *Increased Synthesis of MCL-1 Protein Underlies Initial Survival of EGFR<sup>WT</sup>/EGFR<sup>mutant</sup>-Mutant Lung Cancer to EGFR Inhibitors and Provides a Novel Drug Target*. Clinical Cancer Research, 2018. **24**(22): p. 5658.
70. Hangauer, M.J., et al., *Drug-tolerant persister cancer cells are vulnerable to GPX4 inhibition*. Nature, 2017. **551**(7679): p. 247-+.
71. Terai, H., et al., *ER Stress Signaling Promotes the Survival of Cancer "Persister Cells" Tolerant to EGFR Tyrosine Kinase Inhibitors*. Cancer Research, 2018. **78**(4): p. 1044-1057.
72. Obenauf, A.C., et al., *Therapy-induced tumour secretomes promote resistance and tumour progression*. Nature, 2015. **520**(7547): p. 368-+.
73. Epstein, A.L., et al., *Biology of the human malignant lymphomas. IV. Functional characterization of ten diffuse histiocytic lymphoma cell lines*. Cancer, 1978. **42**(5): p. 2379-91.
74. Bouamar, H., et al., *A capture-sequencing strategy identifies IRF8, EBF1, and APRIL as novel IGH fusion partners in B-cell lymphoma*. Blood, 2013. **122**(5): p. 726-33.
75. Ramanathan, S., et al., *Clinical Pharmacokinetic and Pharmacodynamic Profile of Idelalisib*. Clin Pharmacokinet, 2016. **55**(1): p. 33-45.
76. Murray, G.F., et al., *QPI Allows in vitro Drug Screening of Triple Negative Breast Cancer PDX Tumors and Fine Needle Biopsies*. Frontiers in Physics, 2019. **7**: p. 158.
77. Meyer-Almes, F.J., *Fluorescence lifetime based bioassays*. Methods Appl Fluoresc, 2017. **5**(4): p. 042002.
78. Poudel, C., I. Mela, and C.F. Kaminski, *High-throughput, multi-parametric, and correlative fluorescence lifetime imaging*. Methods Appl Fluoresc, 2020. **8**(2): p. 024005.

79. Zhang, Q., et al., *Towards high-throughput microfluidic Raman-activated cell sorting*. Analyst, 2015. **140**(18): p. 6163-74.
80. Hayflick, L., *The Limited in Vitro Lifetime of Human Diploid Cell Strains*. Exp Cell Res, 1965. **37**: p. 614-36.
81. Hernandez-Segura, A., J. Nehme, and M. Demaria, *Hallmarks of Cellular Senescence*. Trends Cell Biol, 2018. **28**(6): p. 436-453.
82. d'Adda di Fagagna, F., *Living on a break: cellular senescence as a DNA-damage response*. Nat Rev Cancer, 2008. **8**(7): p. 512-22.
83. Kurz, D.J., et al., *Senescence-associated (beta)-galactosidase reflects an increase in lysosomal mass during replicative ageing of human endothelial cells*. J Cell Sci, 2000. **113 ( Pt 20)**: p. 3613-22.
84. Nagano, T., et al., *Identification of cellular senescence-specific genes by comparative transcriptomics*. Sci Rep, 2016. **6**: p. 31758.
85. Shelton, D.N., et al., *Microarray analysis of replicative senescence*. Curr Biol, 1999. **9**(17): p. 939-45.
86. Zhang, H., K.H. Pan, and S.N. Cohen, *Senescence-specific gene expression fingerprints reveal cell-type-dependent physical clustering of up-regulated chromosomal loci*. Proc Natl Acad Sci U S A, 2003. **100**(6): p. 3251-6.
87. Kosar, M., et al., *Senescence-associated heterochromatin foci are dispensable for cellular senescence, occur in a cell type- and insult-dependent manner and follow expression of p16(ink4a)*. Cell Cycle, 2011. **10**(3): p. 457-68.
88. Zhang, R. and P.D. Adams, *Heterochromatin and its relationship to cell senescence and cancer therapy*. Cell Cycle, 2007. **6**(7): p. 784-9.
89. Coppe, J.P., et al., *The senescence-associated secretory phenotype: the dark side of tumor suppression*. Annu Rev Pathol, 2010. **5**: p. 99-118.
90. Saleh, T., et al., *Non-Cell Autonomous Effects of the Senescence-Associated Secretory Phenotype in Cancer Therapy*. Front Oncol, 2018. **8**: p. 164.
91. Sharpless, N.E. and C.J. Sherr, *Forging a signature of in vivo senescence*. Nat Rev Cancer, 2015. **15**(7): p. 397-408.
92. Saleh, T., et al., *Therapy-Induced Senescence: An "Old" Friend Becomes the Enemy*. Cancers (Basel), 2020. **12**(4).
93. Roberson, R.S., et al., *Escape from therapy-induced accelerated cellular senescence in p53-null lung cancer cells and in human lung cancers*. Cancer Res, 2005. **65**(7): p. 2795-803.
94. Saleh, T., et al., *Tumor cell escape from therapy-induced senescence*. Biochem Pharmacol, 2018.
95. Elmore, L.W., et al., *Evasion of a single-step, chemotherapy-induced senescence in breast cancer cells: implications for treatment response*. Clin Cancer Res, 2005. **11**(7): p. 2637-43.
96. Hernandez-Segura, A., et al., *Unmasking Transcriptional Heterogeneity in Senescent Cells*. Curr Biol, 2017. **27**(17): p. 2652-2660 e4.
97. Milanovic, M., et al., *Senescence-associated reprogramming promotes cancer stemness*. Nature, 2017. **553**(7686): p. 96.
98. Puig, P.E., et al., *Tumor cells can escape DNA-damaging cisplatin through DNA endoreduplication and reversible polyploidy*. Cell Biol Int, 2008. **32**(9): p. 1031-43.
99. Yang, L., J. Fang, and J. Chen, *Tumor cell senescence response produces aggressive variants*. Cell Death Discov, 2017. **3**: p. 17049.
100. Rello-Varona, S., et al., *Metaphase arrest and cell death induced by etoposide on HeLa cells*. Int J Biochem Cell Biol, 2006. **38**(12): p. 2183-95.
101. Aguayo-Mazzucato, C., et al., *Acceleration of beta Cell Aging Determines Diabetes and Senolysis Improves Disease Outcomes*. Cell Metab, 2019. **30**(1): p. 129-142 e4.
102. Walaszczyk, A., et al., *Pharmacological clearance of senescent cells improves survival and recovery in aged mice following acute myocardial infarction*. Aging Cell, 2019. **18**(3): p. e12945.
103. Chang, J., et al., *Clearance of senescent cells by ABT263 rejuvenates aged hematopoietic stem cells in mice*. Nat Med, 2016. **22**(1): p. 78-83.
104. Short, S., et al., *Senolytics and senostatics as adjuvant tumour therapy*. EBioMedicine, 2019. **41**: p. 683-692.

105. Debacq-Chainiaux, F., et al., *Protocols to detect senescence-associated beta-galactosidase (SA-beta-gal) activity, a biomarker of senescent cells in culture and in vivo*. Nat Protoc, 2009. **4**(12): p. 1798-806.
106. Blom, K., et al., *Predictive Value of Ex Vivo Chemosensitivity Assays for Individualized Cancer Chemotherapy: A Meta-Analysis*. SLAS Technol, 2017. **22**(3): p. 306-314.
107. Phillips, J. and J.H. Eberwine, *Antisense RNA Amplification: A Linear Amplification Method for Analyzing the mRNA Population from Single Living Cells*. Methods, 1996. **10**(3): p. 283-8.
108. Van Gelder, R.N., et al., *Amplified RNA synthesized from limited quantities of heterogeneous cDNA*. Proc Natl Acad Sci U S A, 1990. **87**(5): p. 1663-7.
109. Li, J. and J. Eberwine, *The successes and future prospects of the linear antisense RNA amplification methodology*. Nat Protoc, 2018. **13**(5): p. 811-818.
110. Brawer, M.K., *New treatments for castration-resistant prostate cancer: highlights from the 44th annual meeting of the american society of clinical oncology, may 30-june 3, 2008, chicago, IL*. Rev Urol, 2008. **10**(4): p. 294-6.
111. Handratta, V.D., et al., *Novel C-17-heteroaryl steroidal CYP17 inhibitors/antiandrogens: synthesis, in vitro biological activity, pharmacokinetics, and antitumor activity in the LAPC4 human prostate cancer xenograft model*. J Med Chem, 2005. **48**(8): p. 2972-84.
112. Vasaitis, T., et al., *Androgen receptor inactivation contributes to antitumor efficacy of 17{alpha}-hydroxylase/17,20-lyase inhibitor 3beta-hydroxy-17-(1H-benzimidazole-1-yl)androsta-5,16-diene in prostate cancer*. Mol Cancer Ther, 2008. **7**(8): p. 2348-57.
113. Njar, V.C. and A.M. Brodie, *Discovery and development of Galeterone (TOK-001 or VN/124-1) for the treatment of all stages of prostate cancer*. J Med Chem, 2015. **58**(5): p. 2077-87.

## 9 Appendix

### 9.1 Data Collection and Processing Details

#### Collection

Improved bandwidth of the autofocus feedback loop enabled the system to reach speeds of 8 mm/s (~32 fps), maxing out the camera's ability. New problems arose due to the file size of a single subcolumn (420 images, 100mm down or back). A single subcolumn was now approximately 1.6 gigabytes. When this was saved as ".mj2" file, it took approximately ~40 seconds to save. Originally saving the files was done after the completion of image collection for that subcolumn. At 32 fps, this meant image collection took ~12.5 seconds (100mm/8mm/s) with 40 seconds of saving for a total of 52.5 seconds per subcolumn. This wait removed any benefits from moving faster.

To improve this, saving was then changed so that images are saved as a binary file, the simplest and quickest format to save. ".mj2" files include specifications on how to encode and decode the images as well as some compression. As more images are added, the encoding and compression takes longer and longer. Binary files lack these specifications and compression, so this step is removed, and the files can be saved immediately. On the downside, the files increase in size due to the lack of compression, and the user must know what is in the binary file and how to interpret. This latter step is easy as every file contains 420 images of a certain pixel size, while the former step just requires more hard drive space.

Next instead of saving at the end of each loop, the previously collected subcolumn is saved from memory while the next subcolumn is being collected. With saving times now ~12.5 seconds, the same speed as collection, the system operated close to its theoretical maximum.

#### Processing

When performing real-time processing at 40x, the bottleneck remains the processing. Eight subcolumns can be processed in <10 minutes. For comparison, 32 subcolumns can be imaged in 10 minutes. For experiments that don't require real-time processing, all 32 subcolumns can be imaged and then processed later. For experiments that require real-time processing, a six-well plate is used (two columns: A and B). When resistant cells need to be isolated, the column "A", in which the treated cells of interest are, is processed in real-time. As this processing occurs, the control column ("B") can be imaged and analyzed later.

But before the column B is imaged, a MATLAB worker (one CPU core) on the Control computer starts sending the files from column A to an internal SSD hard drive on the Processing computer. Columns A and B are originally saved on two separate external hard drives.

These two things are necessary to prevent the Control computer from trying to save images from column B on the same hard drive that the MATLAB worker in the background of the Control computer is trying to move Column A to the Processing computer. If accessed at the same time, either the image collection or the moving of files over would come to a halt. This same dance is happening on the Processing Computers SSD. Files are only moved to Processing computer SSD when Control computer knows the Processing computer is not accessing that SSD hard drive.

As these files are big and saving them takes around ~12.5 seconds, if there is constantly a queue forming at the different hard drives, both collection and processing would slow significantly. After the collection of column "B" is complete of loop  $n$ , and files from column "A" loop  $n$  have been moved to the Processing computer, the Control computer waits for the Processing computer to finish processing column A loop  $n-1$  before collection of loop  $n+1$  column A begins.

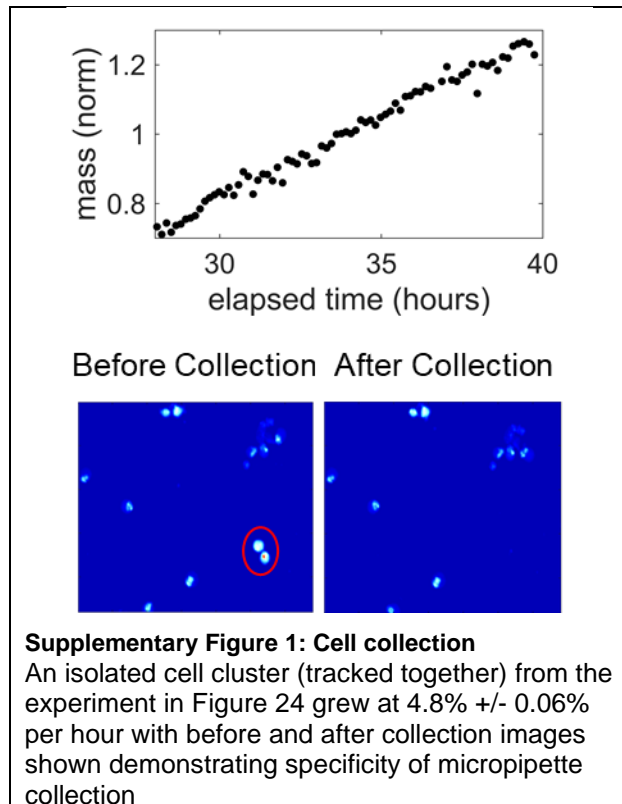
From the perspective of the Processing computer, files appear on its internal SSD hard drive and begins processing them. If loop  $n$  is being unwrapped, unwrapped images from loop  $n-1$  are sent to 12 workers to

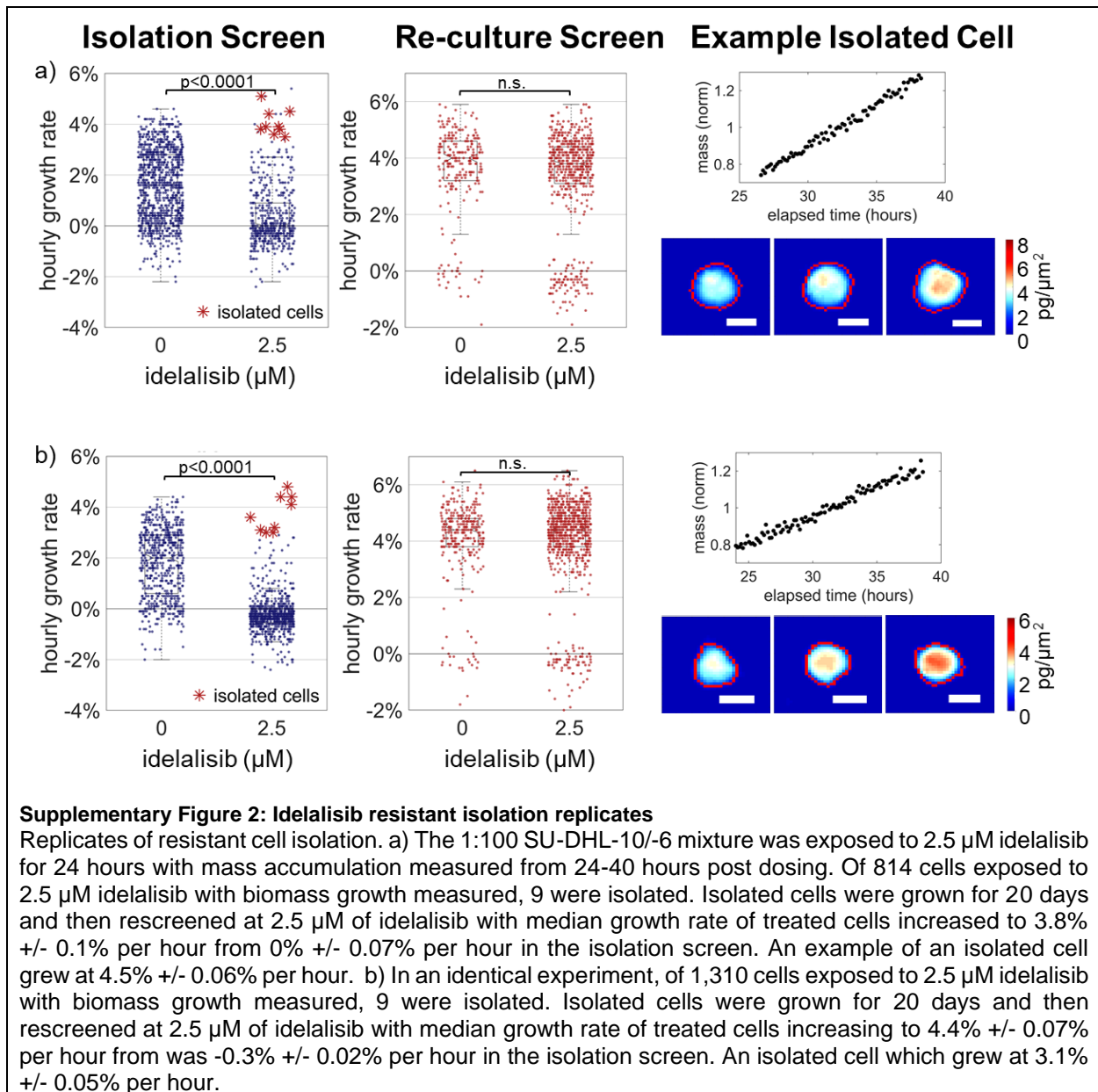


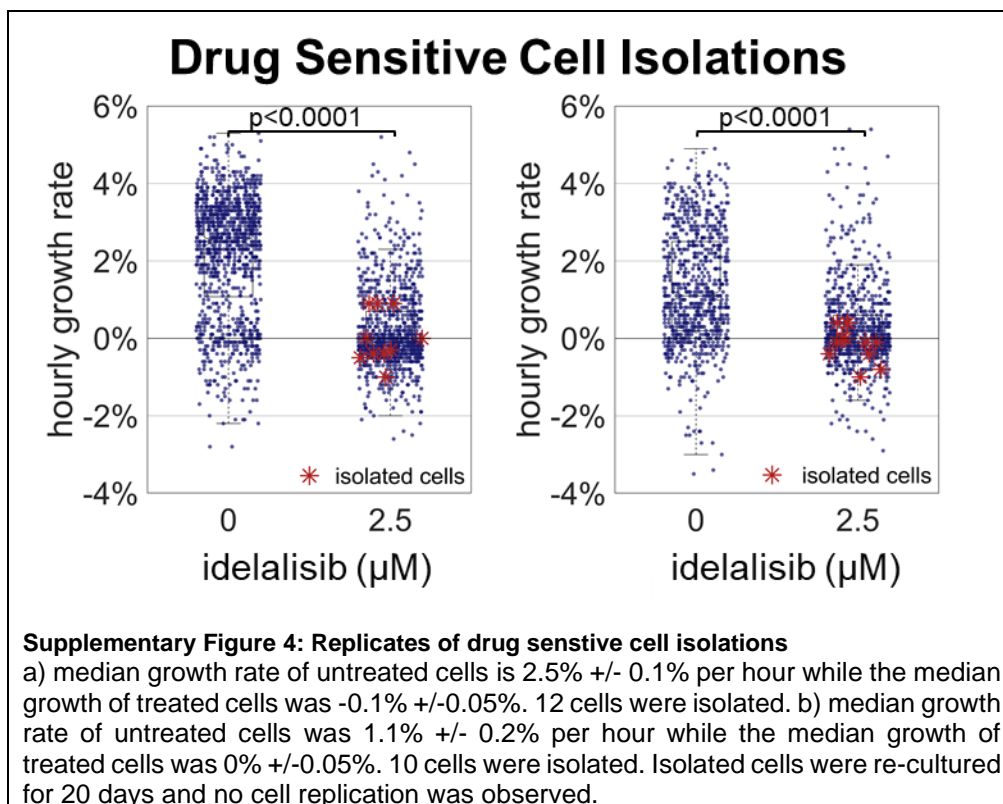
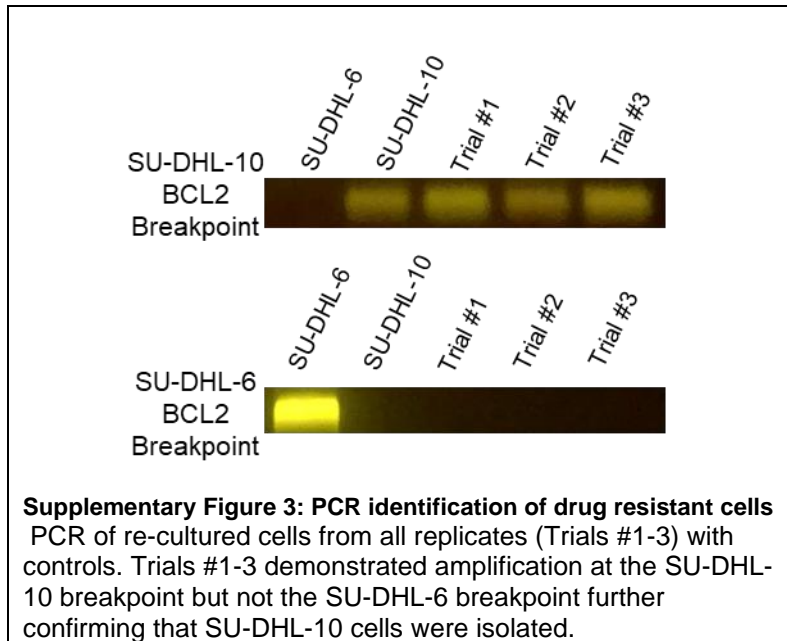
be processed. Once the unwrapping of loop  $n$  is complete, MATLAB waits for processing to be completed (from 0-5s) and then the unwrapping of loop  $n+1$  and processing of loop  $n$  begins.

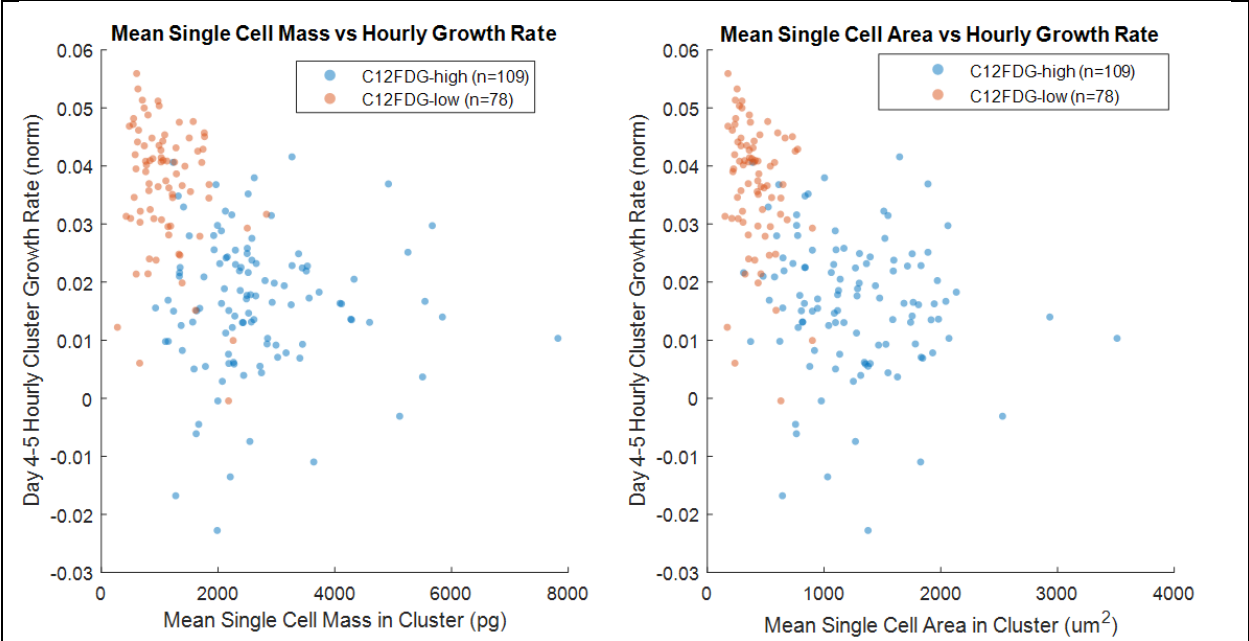
These processing changes enabled a doubling (4- $\rightarrow$ 8 sub columns) of the amount of the data that could be processed within 10 minutes. Continued improvements will come from parallelizing the unwrapping through multiple GPUs, and more workers to parallelize the processing.

## 9.2 Supplementary Figures

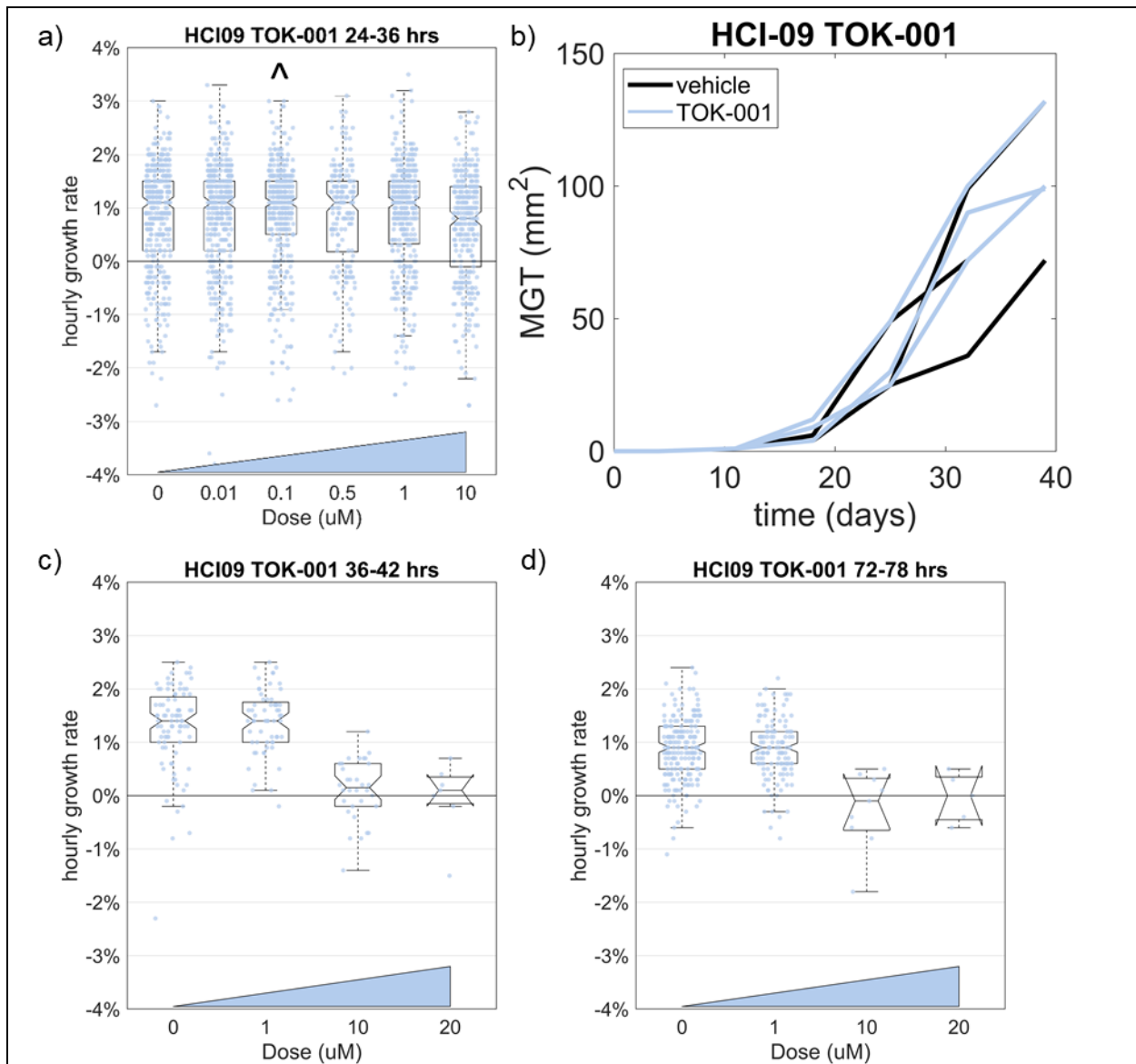








**Supplementary Figure 5: Cell clusters with smaller single cells grow faster after etoposide treatment**  
H460 cells were sorted for C<sub>12</sub>FDG and monitored by HSLCI from day 4 to day 5 after treatment. With significant noise, there appears to be an inverse relationship between cell size and growth rate.



**Supplementary Figure 6: TOK-001 HCI09 *in vitro-in vivo* correlation**

TOK-001, also known as Galeterone, is a steroidal antiandrogen with unique three pronged mechanism of action: it is an androgen receptor antagonist, androgen receptor down regulated and a CYP17A1 inhibitor, preventing androgen biosynthesis [110-112]. With limited treatment options in triple negative breast cancer, TOK-001 was screened on the androgen receptor positive HCI-09 PDX. a). HSLCI screen of TOK-001 24-36 hrs after treatment. Maximum concentration seen in mice is highlighted by the carrot “^”, indicating TOK-001 is unlikely to be effective *in vivo* [113]. b) *in vivo* treatment data from HCI-09 mice treated with TOK-001 5 days a week from day 25 onward showed no significant difference in tumor growth. c & d) A second HSLCI screen performed 36-42 hrs after treatment, and 72-78 hrs after treatment. Monitoring was only six hours in attempt to see if looking more frequently would boost cell counts as PDX cells remain relatively unattached and can float away. HCI-09 cells still demonstrated resistance at 1µM well above the CMax of 100 nM. While the 10 µM dose did appear to be more effective as time went on, a lack of cells due to the only 6 hours of monitoring hardly makes this a firm conclusion. Together these data show the correct prediction of *in vivo* resistance by HSLCI.

## Vita

Graeme Fritchen Murray was born on February 18<sup>th</sup>, 1992 in Seattle, Washington and is an American citizen. He graduated from Lakeside School in Seattle, Washington in 2010. He received a Bachelor of Arts in Physics with Honors and a Bachelor of Arts in Chemistry from the University of Chicago in 2014. In 2015, he joined the MD/PhD program at Virginia Commonwealth University.